DISSERTATION

FROM SURFACE TO TROPOPAUSE: ON THE VERTICAL STRUCTURE OF THE TROPICAL CYCLONE VORTEX

Submitted by

Alexander J. DesRosiers

Department of Atmospheric Science

In partial fulfillment of the requirements

For the Degree of Doctor of Philosophy

Colorado State University

Fort Collins, Colorado

Summer 2024

Doctoral Committee:

Advisor: Michael M. Bell

Elizabeth A. Barnes
Kristen L. Rasmussen
Frances V. Davenport

ABSTRACT

FROM SURFACE TO TROPOPAUSE: ON THE VERTICAL STRUCTURE OF THE TROPICAL CYCLONE VORTEX

The internal vortex structure of a tropical cyclone (TC) influences intensity change. Beneficial structural characteristics that allow TCs to capitalize on favorable environmental conditions are an important determinant as to whether a TC will undergo rapid intensification (RI) or not. Accurately forecasting RI is a significant challenge and past work identified characteristics of radial and azimuthal structure of the tangential winds which favor RI, but vertical structure has received less attention. This dissertation aims to define vertical structure in a consistent manner to improve our understanding of how it influences intensity change in observed and modeled TCs, as well as discern when strong winds are more likely to reach the surface with potential for greater impacts.

Part 1 investigates the height of the vortex (HOV) in observed TCs and its potential relationships with intensity and intensification rate. As a TC intensifies, the tangential wind field expands vertically and increases in magnitude. Past work supports the notion that vortex height is important throughout the TC lifecycle. The Tropical Cyclone Radar Archive of Doppler Analyses with Recentering (TC-RADAR) dataset provides kinematic analyses for calculation of HOV in observed TCs. Analyses are azimuthally-averaged with tangential wind values taken along the radius of maximum winds (RMW). A threshold-based technique is used to determine the HOV. A fixed-threshold HOV strongly correlates with current TC intensity. A dynamic HOV (DHOV) metric quantifies vertical decay of the tangential wind normalized to its maximum at lower levels with reduced intensity dependence. DHOV exhibits a statistically significant relationship with TC intensity change with taller vortices favoring intensification. A tall vortex is always present in observed cases meeting a pressure-based RI definition in the following 24-hr period, suggesting DHOV may be useful to intensity prediction.

In Part 2, numerical modeling simulations are utilized to discern mechanisms responsible for the observed relationships in Part 1. Vertical wind shear (VWS) can tilt the TC vortex by misaligning the low- and mid-level circulation centers which prevents intensification until realignment occurs. Both observed and simulated TCs with small vortex tilt magnitudes possess DHOV values consistent with those observed prior to RI. In aligned TC intensification, DHOV and intensity have a mutually increasing relationship, indicating the metric provides useful information about vertical structure in both tilted and aligned TCs. Vertical vortex growth during RI is sensitive to internal processes which strengthen the TC warm core in the upper-levels of the troposphere. Comparison of a TC simulated in the presence of a concentrated upper-level jet of VWS to a control simulation in quiescent flow indicates that disruption of intensification in the upper levels limits vortex height and intensity without appreciable low- to mid-level tilt.

Part 3 focuses on decay of the TC wind field as it encounters friction near the surface in the planetary boundary layer (PBL). Surface winds are important to operational TC intensity estimation, but direct observations within the PBL are rare. Forecasters use reduction factors formulated with wind ratios (WRs) from winds observed by aircraft in the free troposphere and surface winds. WRs help reduce stronger winds aloft to their expected weaker values at the surface. Asymmetries in the TC wind field such as those induced by storm motion can limit the accuracy of static existing WR values employed in operations. A large training dataset of horizontally co-located wind measurements at flight level and the surface is constructed to train a neural network (NN) to predict WRs. A custom loss function ensures the model prioritizes accurate prediction of the strongest wind observations which are uncommon. The NN can leverage relevant physical relationships from the observational data and predict a surface wind field in real-time for forecasters with greater accuracy than the current operational method, especially in high winds.

ACKNOWLEDGEMENTS

Many incredible people have supported me during this journey as I learned, like many others, how to be a scientist from scratch. I am thankful for the care and dedication of my parents who always made it their priority to support my siblings and I in all of our endeavors. My mother, Denise DesRosiers, taught me the importance of hard work and how a combination of effort and faith in yourself can carry you forward toward your goals. My father, James DesRosiers, was an indominable one man cheering squad, who always encouraged me to pursue my passion and took genuine interest in all that I do. Although he is missed dearly, the courage and grace with which he faced his greatest challenge taught me a great deal about the importance of always striving to do good, no matter the circumstances. I would never have had the courage to pursue such an abnormal and challenging path without the lessons he taught me and his unrelenting support. My siblings, Michael and Mary DesRosiers are a crucial part of my family support system that makes this all possible. I would like to thank my fiancée, Devon Leasure, for standing by my side through all of the ups and downs of graduate school and life surrounding it. She was always willing to go above and beyond to help me and I am lucky to have such a committed partner in life. Her parents, Kevin and Elise Leasure have also been a wonderful source of support throughout and encouragement in this process. I appreciate my dog, Elbert, for being a source of unconditional happiness and love.

I am grateful to the entire Colorado State University Department of Atmospheric Science, especially the administrative staff, for an excellent place to learn as I worked my way towards making contributions to this field. My advisor, Michael Bell, gave me incredible opportunities to work on a wide variety of projects that greatly expanded my skillset. His expertise and mentorship is pivotal to my growth as a scientist, the work presented here, and other publications produced during this time. Phil Klotzbach has also served as an unofficial mentor and I owe my ability to effectively communicate science to the time, effort, and opportunities he gave me in our work with the seasonal hurricane forecast. The opportunities I received to communicate with local and national media are a unique learning experience that I cherish. I would like to thank my committee members,

Elizabeth Barnes, Kristen Rasmussen, and Frances Davenport who have provided their time and expertise to prepare me for a career in this field and improve the quality of my work. Suren Chen, a past committee member, provided helpful feedback on this work in its earlier stages. The contributions of Michael Fischer and Paul Reasor from the NOAA/AOML Hurricane research division, who served as co-authors of published work contained within this text, are greatly appreciated.

I thank the entire Bell research group, past and present, who always entertained my questions and served as a knowledgeable sounding board for working through problems related to and outside of the domain of research. I appreciate several scientists at CIRA who were always eager to help as well. Fellow ATS/CIRA DEI committee members and my instructors in the course“Social Responsibility in Atmospheric Science" opened my eyes to the many issues that plague our field, and I pledge to carry on with this knowledge as an ally to worthy causes pertaining to diversity, equity, and inclusion. I am grateful to many friends, here in Fort Collins and elsewhere, who always bring so much joy into my life amidst the strain of a PhD program. To any I have not named here, know you are appreciated and your role in my development as a scientist and a person do not go unnoticed. However, this document is long enough as is, and I had to stop at some point to spare my committee, who must read it.

This research is supported by the Office of Naval Research (ONR) Award N000142012069 and the NOAA Hurricane and Ocean Testbed (HOT) program award NA22OAR4590527.

DEDICATION

To my father, James DesRosiers, who would always tell my siblings and me before school to "learn something new, come home, and tell me about it." Your love, guidance, and memory carry me forward as I continue to learn new things.

TABLE OF CONTENTS

LIST OF TABLES

LIST OF FIGURES

Chapter 1

Introduction

1.1 Motivation

Tropical cyclones (TCs) are large and impactful warm-cored low pressure systems which often originate in the tropical and subtropical oceans. TCs can generate a large footprint of hazards including, but not limited to, high winds, dangerous surf, and heavy precipitation. Many TCs spend the duration of their existence generating hazardous marine conditions over the open ocean, but some make their way onshore bringing considerable impacts to coastal and inland communities via wind, water, and storm surge inundation. Predictions of TC track and intensity from operational forecast centers are vital to identifying and warning communities to prepare for an approaching storm and its associated hazards.

Advances in TC track forecasting have outpaced those made in intensity forecasting (DeMaria et al. 2014). Despite recent improvements to intensity forecasting efforts (Cangialosi et al. 2020), accurate TC intensity prediction remains challenging, due in part to a phenomenon known as rapid intensification (RI). RI is defined by the National Hurricane Center (NHC) as a 30 kt or greater increase in the maximum sustained winds of a TC at 10-meter altitude in a 24-hour period (Kaplan and DeMaria 2003; Kaplan et al. 2010). Successful forecasts of RI by the NHC are still uncommon (Trabing and Bell 2020). Environmental conditions which are conducive to TC intensification are well understood, but internal dynamical processes are an important determinant of RI in favorable conditions (Hendricks et al. 2010). Research efforts focused on internal structure and processes in TCs, such as those presented here, are important to improving our understanding of RI.

TCs draw energy from the heat and moisture of the warm oceans. The storms intensify and maintain themselves via convection within the cyclone-scale circulation (Ooyama 1969). Some concerning trends have emerged in the global records of TC activity in recent decades as our planet and oceans warm (Klotzbach et al. 2022b). A larger proportion of TCs are reaching extreme

intensities of category 4 and 5 on the Saffir-Simpson Hurricane Wind Scale and extreme RI events ($\geq$ 50 kt day^{-1}) are increasingly common. These more intense storms pose greater threats to the communities they may impact. Global damages from TCs are increasing in recent decates as a result of landfalling storms impacting a growing concentration of population and wealth on the coasts. As the intensity and impacts of TCs increase, so too should the focus on improving our understanding of internal factors relating to RI, which can enhance our ability to forecast TC intensity.

1.2 Height of the Tropical Cyclone Vortex (HOV)

TCs are deep convective vortices which can span the depth of the troposphere at their most intense (Rogers et al. 2017). The height of the tropical cyclone vortex (HOV) is an important structural characteristic throughout the TC lifecycle. From the earliest stages, the height of the pre-depression disturbance is important to TC genesis (Wang et al. 2012). HOV is also important during intensification. Fitzpatrick (1995) found increased inner-core upper-level tangential (rotational) wind was associated with faster TC intensification rates in storms observed by aircraft. Vertical development of the TC vortex was observed during the latter stages of RI in Hurricane Michael (2018) by airborne radar (DesRosiers et al. 2022). Upper-level intensification of the tangential winds decreased the vertical decay of the wind field and took place in concert with the development of an upper-tropospheric component of the warm core via thermal wind balance.

A taller TC vortex should benefit the intensification process. Numerical modeling simulations indicate a deeper initial vortex promotes faster intensification in idealized TCs (Peng and Fang 2021). The more coherent vertical structure enables the TC to sustain deep convection and establish a strong secondary circulation composed of inflow near the surface, updrafts in the inner core, and outflow in the upper levels. Vertical structure remains important beyond the initial stages of intensification. The vertical growth of the vortex and upper-level warming were found to be a key factor in the RI of Hurricane Michael as it approached extreme intensity. Warm core development

at any level of the troposphere, especially in the upper levels, contributes to pressure falls at the surface (Hirschberg and Fritsch 1993) of an intensifying TC.

HOV is an important component of TC structure, but its lack of a consistent defining metric is an impediment to its study. Past work on the topic focused on the decay of the tangential wind field with height along the radius of maximum winds (RMW) through the lower- and mid-levels of the troposphere (Stern and Nolan 2011). Theoretical considerations suggest there should be uniformity in the decay of tangential winds through these layers, but the observed wind profiles exhibited some variability (Stern et al. 2014). These previous studies lay out a useful starting framework for evaluating tangential wind decay by normalizing it to the maximum values in lower levels of the troposphere. Their data was limited by past observing platforms which provided insufficient coverage of the upper levels where vertical growth is expected during RI, making it difficult to discern a relationship with intenisty change. Great strides have been made in understanding internal radial and structural characteristics associated with RI, but vertical structure has received less attention (Chen et al. 2023). Although a theoretical basis for a relationship between vortex height and intensity change is present, more research is needed to characterize the nature of the connection.

A larger sample of observed tropical cyclones (Fischer et al. 2022) and upgrades to the observing capabilities of airborne radar (Aircraft Operations Center 2016) grant an opportunity to revisit the tangential wind decay with height in TCs examined in past work. Finding a meaningful and consistent metric to characterize vortex height in observations provides a useful basis for analysis in numerical model experiments. The combination of a new and expansive observational dataset, idealized numerical modeling tools, and a novel vortex height metric are leveraged in this dissertation to improve our understanding of TC vertical structure a it relates to intensification.

1.3 Surface Winds

Although the full structure of the TC wind field is of importance, the surface wind field is a key determinant the magnitude of TC impacts. Operational centers define TC intensity using the

maximum sustained wind speed (V_{max}) near the surface at 10-meter altitude. Direct observations of surface winds are uncommon due to safety restrictions which prevent TC reconnaissance aircraft from operating near the surface. Aircraft typically operate in TCs in the free troposphere, above the dangerous turbulence of the frictional planetary boundary layer (PBL) in TCs (Lorsolo et al. 2010).

To estimate surface winds, changes in the magnitude of the TC wind field with height are, once again, a principal consideration. Forecasters utilize wind ratios (WRs) which are empirically derived from expendable dropwindsondes, which measure the winds at aircraft flight level, the surface, and the profile between as they descend (Franklin et al. 2003). The WRs currently utilized in operations are a useful tool for V_{max} estimation, but are static recommended values which cannot adequately account for asymmetries present in the wind field at the surface and flight-level (Uhlhorn et al. 2014). The differential impacts of frictional drag in the PBL around the TC make obtaining accurate surface winds with WRs a difficult task, but accounting for larger-scale asymmetries such as those due to TC motion (Shapiro 1983) could improve upon the current methodology.

Several observational technologies can provide estimates of the surface winds in TCs (Knaff et al. 2021), providing useful data for machine learning (ML) techniques, which are gaining traction in the field of atmospheric science (Boukabara et al. 2019). Among these observational platforms, the consistent use of the stepped frequency microwave radiometer (SFMR) provides a large sample of surface wind retrievals co-located with flight-level winds (Uhlhorn et al. 2007). Although the retrieval algorithm designed for the SFMR is imperfect (Sapp et al. 2019), the quantity of data collected by the instrument makes for excellent training data for a ML technique to learn relevant physical relationships for reducing wind observations from the flight level to the surface. Pairing the SFMR training data with ML creates an opportunity to improve upon operational techniques and produce WRs which better account for the complex and variable nature of the changing wind profile in TCs within the PBL. A more accurate methodology obtained through ML can also

assist forecasters in the important task of V_{max} estimation for determining TC intensity in real-time.

1.4 Research Objectives

The overall scientific objective of this dissertation is to improve our understanding of changes in the vertical structure of the TC wind field and how it relates to intensity change and estimation. Three projects are constructed to address key research questions to meet this goal:

1. Are observed TCs with deeper tangential wind fields more likely to intensify than more shallow ones?

2. How does the vertical structure of the TC wind field change throughout TC intensification and impact the process?

3. Can observational datasets of TC surface winds allow an ML method to learn and utilize relevant physical relationships to more accurately reduce wind observations to the surface?

Chapter 2 utilizes a large dataset of kinematic analyses of TC wind fields observed by airborne radar to define HOV and quantify its relationship with TC intensity and intensity change. Chapter 3 uses numerical model simulations to explain the physical meaning behind the observed signal for a relationship between HOV and intensity change found in chapter 2. Chapter 4 continues the exploration of TC vertical structure with a focus on the lower levels of the atmosphere and the TC PBL. A ML technique trained with observational data is used to discern the appropriate WRs needed to estimate surface winds from observations at aircraft flight level in the free troposphere. Chapter 5 synthesizes the key findings of each of these projects and their implications.

Chapter 2

Observed Relationships between Tropical Cyclone Vortex Height, Intensity, and Intensification Rate [1]

2.1 Introduction

Tropical cyclones (TCs) have long been understood as a phenomena capable of spanning a large depth of the troposphere (Haurwitz 1935). While TCs are known to exhibit deep convection throughout their life cycle, the evolution of the vertical structure of the wind field is still not fully understood. Tangential wind profiles in TCs obtained during reconnaissance in the 1950s and 1960s showed early evidence of a link between increased upper-level inner-core tangential wind and TC intensification rate (Fitzpatrick 1995). Evidence suggests that even during the pre-genesis stage of the TC life cycle, the height of the circulation is important. A deep wave pouch in which a TC forms is likely a necessary condition for genesis from an easterly wave (Wang et al. 2012). Once a TC has formed, idealized numerical simulations indicate a deeper initial vortex may undergo faster intensification (Peng and Fang 2021). In a mature TC, vortical flow can continue to reach higher altitudes. Tail Doppler radar (TDR) data collected in Hurricane Patricia (2015) near peak intensity documented an intense axisymmetric vortex with strong tangential winds extending vertically through the depth of the troposphere (Rogers et al. 2017; Martinez et al. 2019).

As a TC becomes more intense, upper-level dynamics and thermodynamics take on greater importance while the vortex grows vertically. Inertial stability decays quickly with height in shallower vortices, likely impacting heating efficiency in the inner-core (Schubert and Hack 1982). Composite observations indicate updraft mass flux peaks at higher altitudes and decreases less rapidly with height in intensifying storms (Rogers et al. 2013). Rapid intensification (RI) is canonically defined

[1]The results presented in Chapter 2 have been published in the *Geophysical Research Letters*: DesRosiers, A. J., M. M. Bell, P. J. Klotzbach, M. S. Fischer, and P. D. Reasor, 2023: Observed relationships between tropical cyclone vortex height, intensity, and intensification rate. *Geophysical Research Letters*, **50**, e2022GL101 877, doi: 10.1029/2022GL101877.

as an increase in the maximum sustained winds of a TC of at least 30 kts in a 24-hour period (Kaplan and DeMaria 2003; Kaplan et al. 2010). Successful prediction of RI is difficult (Trabing and Bell 2020), due in part to the importance of internal dynamical processes in otherwise favorable environments for intensification (Hendricks et al. 2010). DesRosiers et al. (2022) analyzed TDR data from Hurricane Michael (2018) to show how the axisymmetric eyewall vorticity tower grew vertically during RI which occurred during the majority of its lifetime. They argued thermal wind balance linked the upper-level warm core development with changes in vertical structure of the tangential wind field during RI.

Other aspects of TC vertical structure have received attention in observational analysis. Hazelton and Hart (2013) examined the vertical slope of eyewalls in Atlantic hurricanes and documented a greater slope at upper levels than at lower levels. Stern and Nolan (2009) evaluated vertical structure of the radius of maximum winds (RMW). Their observations showed the RMW is approximately a surface of constant absolute angular momentum, and outward slope of the RMW increases with RMW size. Follow-on work investigated the profile of tangential wind field decay with height scaled by the lower-level wind maximum. Although theoretical arguments suggest uniformity in the decay profile, observational data indicate a tendency for the decay to decrease with increasing TC intensity and decreasing TC size (Stern and Nolan 2011; Stern et al. 2014). Collections of aircraft reconnaissance data offer an excellent opportunity to make discoveries about TC structure relative to intensity change (Rogers et al. 2013; Martinez et al. 2017). While prior research suggests that important relationships between height of the TC vortex, TC intensity, and TC intensification rate exist, these relationships have not been fully explored.

In this study, aircraft radar observations from multiple TCs are used to characterize the relationships between vortex height and current intensity, as well as intensification. Section 2.2 describes data and methodology employed to calculate vortex height. Section 2.3 presents and evaluates how calculated vortex height relates to intensity and intensity change rate. Conclusions and recommendations for future work are discussed in section 2.4.

2.2 Data and Methods

NOAA P-3 Hurricane Hunter aircraft reconnaissance research flights equipped with a TDR collect data to document TC inner-core structure. The Tropical Cyclone Radar Archive of Doppler Analyses with Recentering (TC-RADAR) is a large observational dataset of inner-core kinematic analyses derived from TDR data (Fischer et al. 2022). TC-RADAR is used herein to investigate how TC vertical structure relates to intensity and intensification. The version of TC-RADAR (v3j) used contains 306 merged analyses assembled using all TDR data collected during a flight. Data are typically collected in a series of radial aircraft legs crossing the TC center. TC-RADAR analyses are in Cartesian coordinates with a horizontal and vertical resolution of 2 km and 0.5 km, respectively, with a vertical domain extending from the surface to 18 km. Cases in TC-RADAR where the storm was within 50 km of land were excluded to limit impacts of surface heterogeneity on inner-core structure. The 50 km threshold does not entirely eliminate surface heterogeneity impacts, but is consistent with the exclusion criterion used by Fischer et al. (2022). Cases where the TC minimum sea level pressure was greater than 1000 hPa were excluded as they often do not have a coherent azimuthally-averaged vertical structure to analyze. If two flights were close enough together to share a 6-hourly synoptic time and duplicate intensity and intensity change information, only the flight closest to the 6-hourly synoptic time was retained. 223 cases remained after exclusion criteria were applied. The majority of cases are in the North Atlantic with $\sim 3\%$ from the eastern North Pacific.

The process to obtain the height of the TC vortex (HOV) is illustrated using an analysis of Hurricane Florence (2018) (Figure 2.1). The tangential wind field for a merged analysis of interest (Figure 2.1a) is converted from Cartesian to cylindrical coordinates with a resolution of 0.5 km, 2.0 km, and 1° in the vertical, radial, and azimuthal dimensions, respectively. The cylindrical field is azimuthally averaged (Figure 2.1b). A 25% data coverage filter is applied when averaging the cylindrical field in the azimuthal dimension to prevent isolated data points from being unrepresentative of the averaged field in radius-height space. The RMW (cyan; Figure 2.1b) is calculated from the full wind field composed of radial and tangential components by identifying the radius at

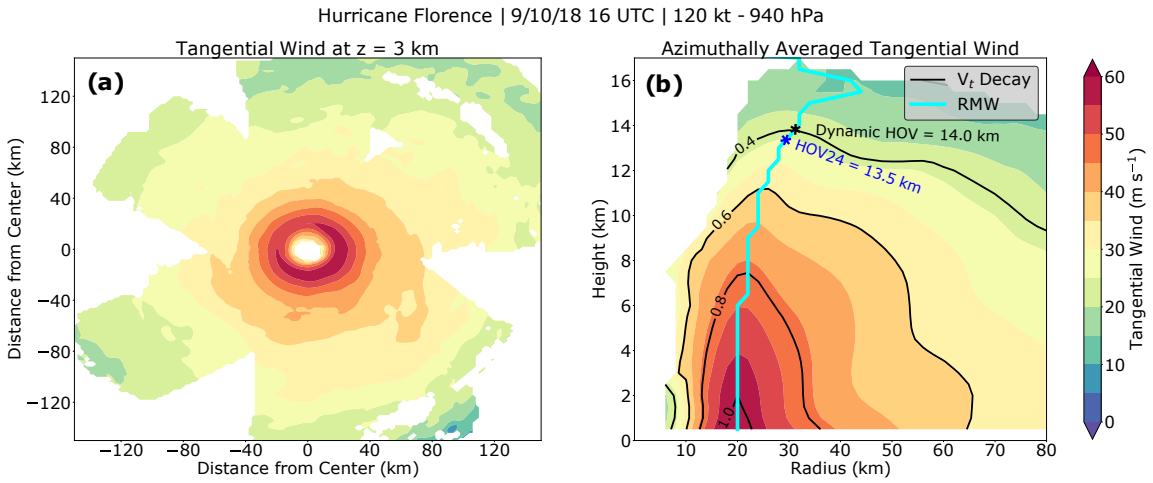

Figure 2.1: (a) Merged tangential wind analysis at a height (z) of 3 km from TC-RADAR in Hurricane Florence at Category 4 intensity and (b) the azimuthally-averaged tangential wind field. The radius of maximum winds is denoted by a cyan contour. Black countours are tangential wind (V_t) divided by the maximum value of V_t found at the RMW at z of 2 km.

which the greatest wind is observed at each vertical level. Tangential wind speed at the RMW is recorded at all vertical levels. Several potential threshold values, which are evaluated in the next section, are used to determine useful HOV definitions. The greatest height at which the maximum value exceeds or is equal to the threshold value is the HOV. If the value is never exceeded or equaled, the HOV is considered to be 0 km. The threshold technique is also applicable for other dynamical fields available in TC-RADAR, but this study focuses on tangential wind. Two HOV values (HOV24 and dynamic HOV) obtained using the described method are noted in the example case (Figure 2.1b). Their definitions and importance to TC intensity and intensity change are provided in the following section.

2.3 Results

The previously-described methodology is used to compute and analyze HOV metrics. An example case is highlighted where HOV could have provided helpful diagnostic information for predicting intensity change.

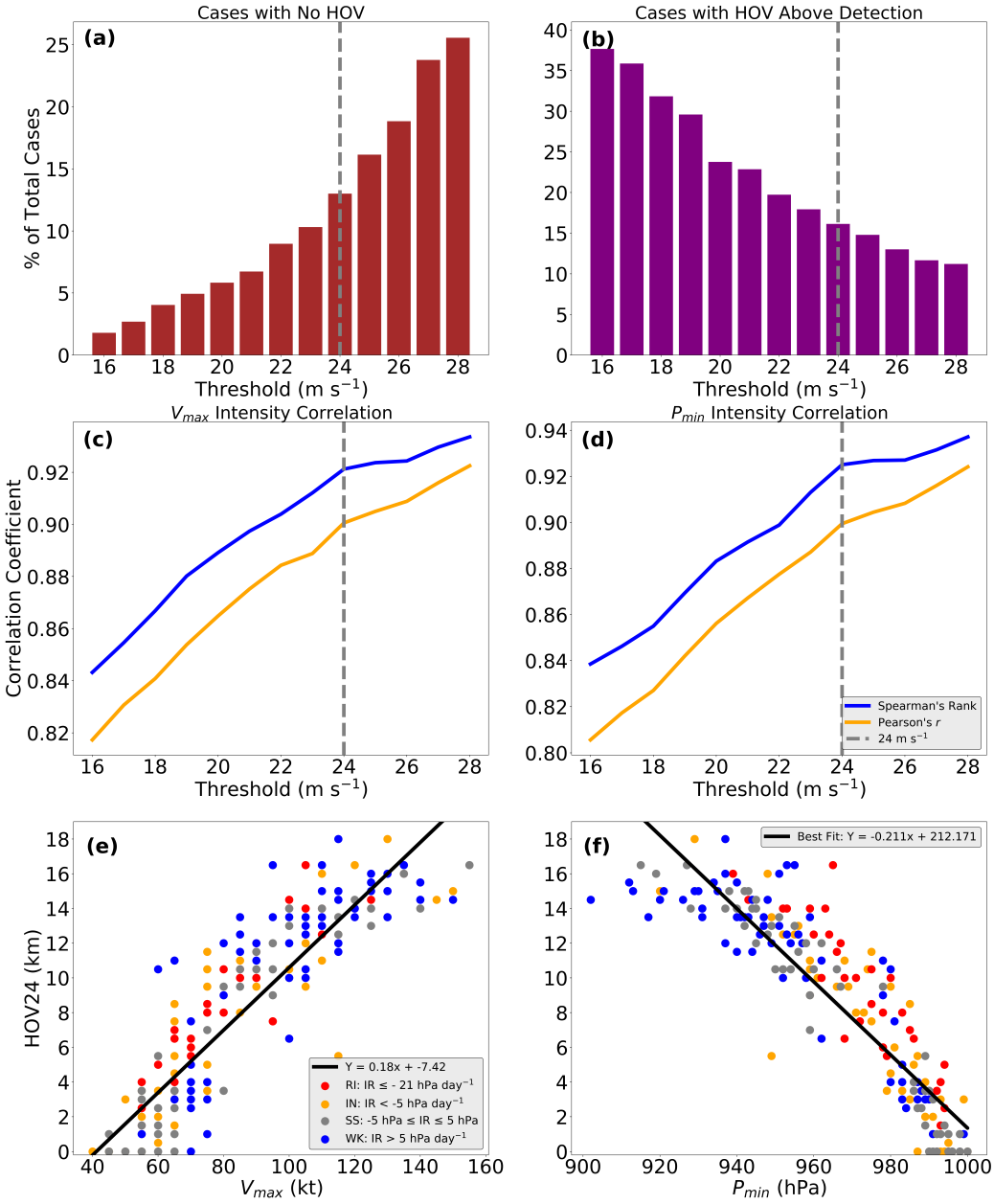

Figure 2.2: Percentage of all cases (n = 223) at each tangential wind threshold where HOV is (a) not recorded or (b) occurs above detection range. Spearman's rank (blue) and Pearson's r (orange) correlation coefficients of HOV with current intensity defined by (c) V_{max} and (d) P_{min}. HOV defined by the 24 m s^{-1} contour (HOV24) for all cases plotted against intensity as defined by (e) V_{max} and (f) P_{min}. Observations are grouped and labeled by intensification rate (IR) following analysis time (colors - legend).

2.3.1 Vortex Height and Intensity

The tangential wind field was used with the threshold method to define a vortex height metric that correlates well with the current intensity of observed TCs in TC-RADAR. Tangential wind thresholds ranging from 16 to 28 m s^{-1} were used to determine the HOV in Figure 2.2. With a lower threshold, many cases failed to capture the threshold value along the RMW within the vertical domain of resolved azimuthally-averaged winds of the TDR analysis (Figure 2.2b). Conversely, higher threshold values failed in cases with tangential winds that did not exceed this value (Figure 2.2a), resulting in an HOV of 0 km. Correlations of HOV values at each threshold with intensity as defined by V_{max}, or the maximum sustained 10 m winds, (Figure 2.2c) and P_{min}, or minimum sea level pressure, (Figure 2.2d) were calculated and tracked. The percentage of cases without an explicitly observed HOV and correlations with intensity at each threshold were used to subjectively determine an optimal threshold value. HOV as determined by the 24 m s^{-1} tangential wind threshold (gray - dashed; Figure 2.2a,b,c,d), or HOV24, exists at a point where the slope of mutual increases in correlation with threshold lessens, and cases with no observed HOV remain low, representing a reasonable compromise between constraints.

HOV24 was directly observed in $\sim 71\%$ of the 223 cases analyzed. HOV24 showed a strong linear relationship with present storm intensity as defined by V_{max} (Figure 2.2e) and P_{min} (Figure 2.2f) with linear correlation values of ~ 0.9 for both. Spearman's rank correlations are slightly stronger with values of ~ 0.92 and 0.93 for V_{max} and P_{min}, respectively. Some non-linearity in the scatter can be explained at the low end where observed azimuthally-averaged tangential winds are weaker than 24 m s^{-1} in some cases. At higher altitudes, asymptotic behavior is likely due in part to TDR sensitivity limitations. Color coding of the dots in the scatter (Figure 2.2e,f) indicate categorical classifications of intensity change determined by temporal changes in P_{min} (legend; Figure 2.2e) described in the following subsection. Quantification of the known mutually-increasing relationship between vertical depth and intensity in TCs (Stern et al. 2014; Fischer et al. 2022) in a novel observational dataset exhibits the potential utility of this methodology to explore connections between vortex height and intensity change.

2.3.2 Relationship with Intensity Change

A key argument to the importance of the vertical development observed during the RI of Hurricane Michael (DesRosiers et al. 2022) was the integral nature of P_{min} as an intensity metric. As the vortex grew in height, geopotential height decreases aloft helped contribute to reduction of P_{min} at the surface. Given the hydrostatic link between vortex height and surface P_{min}, the relationship between HOV and intensity change is examined through changes in pressure, where the relationship is stronger than the one obtained using wind. Structural factors which can lower P_{min} are important to understand as P_{min} correlates better with normalized damage in continental US landfalling hurricanes than V_{max} (Klotzbach et al. 2020, 2022a). We hypothesize that geopotential height falls aloft in a deeper vortex are associated with a more efficient reduction of P_{min}, which is an integrated metric of the three-dimensional wind field through thermal wind balance.

Cases from TC-RADAR are divided into four intensity change categories based on the 24-hour change in P_{min} following storm analysis time given in TC-RADAR. Aircraft reconnaissance missions are most common in TCs threatening land. Restricting to only cases where a full 24-hour period occurred over water further limits the sample size due to the many landfalling TCs observed. If landfall occurred in the final 6 hours (11 of 116 cases in the final dataset), the analysis was retained in addition to purely over water cases, and the 18-hour over water intensification rate is extrapolated to 24 hours assuming a constant rate. The RI category boundary is determined with a method consistent with its original calculation with respect to V_{max} (Kaplan and DeMaria 2003). The equivalent 95^{th} percentile of over water intensity change for pressure-based RI is a 21 hPa drop in P_{min} in 24 hours, when considering the period of 1979 to 2021 for the North Atlantic (Landsea and Franklin 2013a). Cases with pressure drops greater than 5 hPa, but not crossing the RI threshold make up the intensifying (IN) group. Changes in P_{min} from -5 hPa to +5 hPa are considered steady-state (SS). Increases in pressure greater than 5 hPa are classified as weakening (WK).

Metrics using specific thresholds like HOV24 have strong correlations with present intensity, so a value reflective of vortex height with decreased sensitivity to present intensity is introduced as

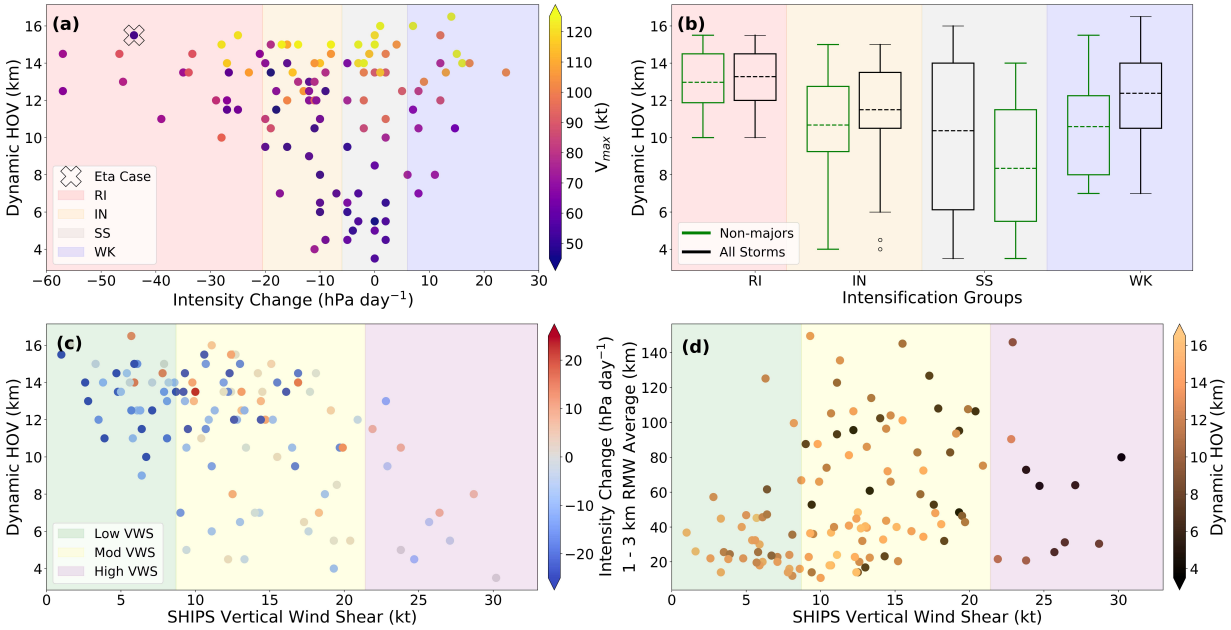

Figure 2.3: (a) Dynamic HOV determined by decay of tangential wind to 40% its value at height (z) of 2 km as a function of intensity change. Intensity of storm at analysis time (colorbar) as well as intensity change groups (shaded) are shown. Two WK cases occupy the x,y coordinate pairs of (8,7), (9,13), and (12,15.5) with the intensities of each case pair within 5 kt of each other. A hollow X surrounds a Hurricane Eta (2020) case discussed in Section 3. (b) Box and whisker plots with means (dashed) for each intensity change grouping for all storms (black) and non-major hurricane strength storms (green). (c) Differences in dynamic HOV for different regimes of vertical wind shear with low, moderate, and high values shaded. 24-hour change in pressure following the analysis time (colorbar) is shown for each point. (d) Dynamic HOV values (colorbar) in cases with varying shear and low-level (z = 1-3 km) averaged RMW.

dynamic HOV. Dynamic HOV is obtained with the same thresholding approach along the RMW, however, the threshold is now specific to the intensity of each case. The threshold is 40% of the value of the maximum tangential wind at 2 km altitude (Figure 2.1b) due to its greater relationship with intensity change compared to other thresholds investigated (not shown). Scaling decay with the 2-km maximum tangential wind is consistent with previous work investigating wind field decay (Stern and Nolan 2011; Stern et al. 2014). The HOV is set as the last vertical level where this threshold is equaled or exceeded along the RMW as defined by the full wind field. For inclusion of a case in dynamic HOV analysis, the threshold value must be explicitly observed. 116 cases were qualified for analysis with counts of 20, 41, 34, and 21 in the RI, IN, SS, and WK groups, respectively. Of the 223 original cases, dynamic HOV was not observed in 77, and 30 did not have at least 18 hours over water after analysis.

Plotting dynamic HOV values against intensity change (Figure 2.3a) reveals a narrowing of the range of values towards higher HOV as the intensification rate becomes greater. The present intensity of TC cases (colors; Figure 2.3a) shows some relationship with dynamic HOV, consistent with previously-calculated profiles of observed vertical wind field decay (Fischer et al. 2022; Stern et al. 2014). Storms of major (Category 3+; $\geq$ 96 kt) intensity on the Saffir-Simpson Hurricane Wind Scale typically have a deep vertical structure indicated by high dynamic HOV values which vary little. Non-major cases possess considerable variability. Box and whisker plots with dashed mean values (Figure 2.3b) show a tendency of increasing dynamic HOV as the intensification rate moves towards RI. The increasing trend is most prevalent in non-major cases (green) which is consistent with the increased upper-level tangential winds found in intensifying storms of tropical storm to lower-end hurricane intensity (Fitzpatrick 1995). In general, the results suggest a tall vortex may be a necessary condition for pressure-based RI in the observed dataset. The result relates well with findings of a comparison study (Hazelton et al. 2018) in which modeled Atlantic TCs exhibited higher than observed intensities and a greater vortex depth parameter based on V_t decay when compared to TDR observations.

All Storms

(a)	RI	IN	SS	WK
RI		0.03	0.03	0.47*
IN	0.03		0.43	0.22*
SS	0.03	0.43		0.1
WK	0.47*	0.22*	0.1	

Non-Majors

(b)	RI	IN	SS	WK
RI		<0.01	<0.01	0.03
IN	<0.01		0.02	0.77
SS	<0.01	0.02		0.06
WK	0.03	0.77	0.06	

Figure 2.4: Two-sided p-values for Mann-Whitney U tests between intensification groups for (a) all storms and (b) excluding major hurricanes. White squares indicate a failure to reject the null hypothesis, while green squares are statistically significant differences at the 95% confidence level. Results with an asterisk indicate statistically significant differences in present intensity between groups.

The relationship between dynamic HOV and intensity change must also be considered in the context of vertical wind shear (VWS). Vortex height is determined through azimuthal averaging about a lower-tropospheric center, so a tilting of the vortex by VWS (Jones 1995) can stunt the height of the vortex when it is unable to be aligned upright about its center, weakening the azimuthally-averaged projection of tangential winds. SHIPS VWS (SHDC: deep-layer shear with vortex removed) magnitude at analysis time (DeMaria et al. 2005) is examined in three different categories of low, moderate, and high as defined in Rios-Berrios and Torn (2017), a climatological study focused on the challenges of TC intensity change prediction in moderate VWS. Moderate VWS falls between and including the magnitudes of 8.7 and 21.4 kt with low and high ranges on the opposite ends of these bounds, respectively. Dynamic HOV tends to be higher in low VWS environments and lower in high VWS environments. There is substantial variability in the moderate VWS regime (Figure 2.3c). Cases with a greater reduction in P_{min} occurring in moderate shear tend to have higher dynamic HOV. The radial extent of the circulation also appears to be related to the dynamic HOV. TCs with more compact inner cores, as evidenced by the z = 1-3 km RMW average value, are more likely to have higher dynamic HOV values (Figure 2.3d). Low VWS environments also tend to favor a more compact inner-core, which is known to be conducive to RI (Carrasco et al. 2014).

Significance testing is used to determine if there are statistically significant differences between dynamic HOV values in intensity change groups for all storms and non-major cases. The Mann-Whitney U two-tailed non-parametric test (Nachar 2008) is chosen to determine if the null hypothesis can be rejected, and the distributions of dynamic HOV values between two groups can be considered different from each other. Results of the statistical tests are given as matrices in Figure 2.4 where two-sided p-values in highlighted green boxes denote rejection of the null hypothesis at the 95% confidence level. Distributions of dynamic HOV values for RI were found to be different from IN and SS groups in both categories. Differences between the IN and SS groups were also statistically significant for non-majors, but confidence in this particular result drops to 94% when a tangential-wind-defined RMW is used. Lower p-values for non-majors indicates the relationship between greater dynamic HOV and RI is driven by weaker cases. The majority of observed wind-based RI cases in the Atlantic initiate below hurricane strength (Kaplan and DeMaria 2003). The same two-tailed Mann-Whitney U test was used to probe for differences in the current intensity via P_{min} in the groups (Figure 2.3a). An asterisk (Figure 2.4) indicates a comparison between groups where the null hypothesis that the present intensity distribution was the same could be rejected, and differences in intensity may impact differences in dynamic HOV. Of the statistically significant differences found in dynamic HOV, none were flagged for intensity differences. Although not marked as significant, the mean P_{min} of the RI group is $\sim$ 2 hPa less than the IN group for all storms and $\sim$ 6 hPa for non-majors. Some differences in intensity between RI and IN are expected given previous research showing that as a TC grows more intense, the heating efficiency increases as well (Schubert and Hack 1982; Nolan et al. 2007), likely enabling greater pressure falls. Mean dynamic HOV values of the WK cases were not less than SS, but this may be due to mean intensity differences. Some WK storms of lesser intensity were also previously major hurricanes with established tall vortices. The average peak lifetime intensity of the WK cases is $\sim$ 115 kt. The timescale of decay of the vertical structure in weakening TCs and what controls the decay rate is a topic for future investigation.

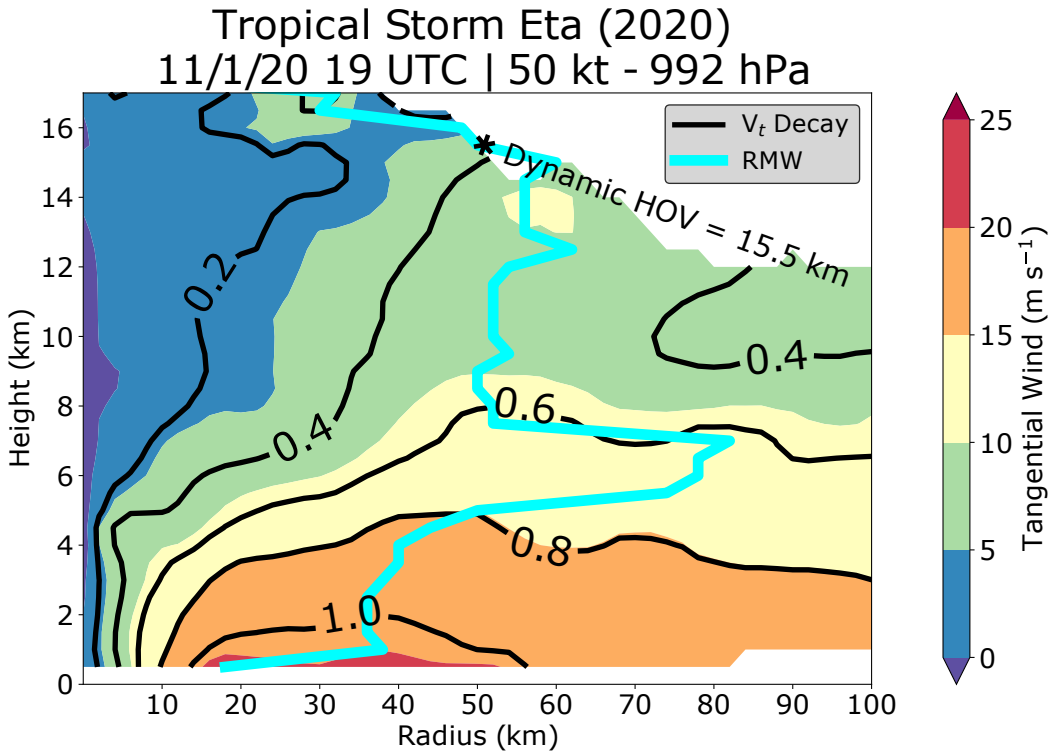

Figure 2.5: Azimuthally-averaged tangential wind field from Tropical Storm Eta (2020). The RMW is denoted by a cyan contour and the dynamic HOV by an asterisk. Black countours are tangential wind (V_t) divided by the maximum value of V_t found at the RMW at a height (z) of 2 km.

2.3.3 Example Case: Hurricane Eta

Dynamic HOV may have been an early indicator in the extreme RI event preceding major Hurricane Eta's (2020) landfall in Nicaragua. A flight centered around 19 UTC on 1 November 2020 sampled Eta as a 50 kt tropical storm with P_{min} of 992 hPa in a favorable environment. The National Hurricane Center forecast Eta to intensify in their 21 UTC advisory issued later that day. The forecast called for a strengthening 80 kt Category 1 hurricane at 18 UTC on 2 November 2020. Eta far exceeded expectations and became a 115 kt Category 4 hurricane with P_{min} of 948 hPa by the verification time (Pasch et al. 2021). Dynamic HOV calculated from the 1 November flight into then Tropical Storm Eta was an impressive 15.5 km (Figure 2.3a), indicating a vertical structure that we hypothesize was conducive for its subsequent RI event (Figure 2.5).

2.4 Conclusions

Previous studies have shown that the height of the tropical cyclone (TC) vortex (HOV) is an important structural factor in the TC life cycle. A comprehensive dataset of TDR-derived kinematic observations of TCs makes possible the characterization of relationships between vortex height and TC intensity and intensification. A threshold-focused technique is used to determine the HOV based on tangential wind values along the radius of maximum winds (RMW). HOV as determined by the 24 m s^{-1} (HOV24) tangential wind threshold offered the best compromise between number of cases where the value is directly observed and correlations with present intensity. Correlation values are ~ 0.9 for HOV24 and intensity as defined by wind and pressure. These results provide strong and novel observational evidence of the known relationship between vortex height and TC intensity (Stern et al. 2014; Fischer et al. 2022).

Rapid intensification (RI) in TCs is challenging to predict and controlled by internal dynamical processes in addition to environmental factors. A more general understanding of the role vertical structure plays should improve understanding of internal mechanisms during RI. RI is defined in this study in a similar manner to the original, wind-based definition using rates of decrease in P_{min} which yielded a stronger signal than rates of increase in V_{max}. Each case in the dataset is grouped into rapidly intensifying (RI), intensifying (IN), steady-state (SS), and weakening (WK) groups based on a 24-hour change in P_{min} following analysis time. Dynamic HOV, which is determined by the height at which the tangential wind along the RMW decays to 40% of its value at a height of 2 km, is used due to its lower sensitivity to present intensity as compared to a fixed threshold. As decreases in pressure following the analysis time become greater, the distribution of dynamic HOV values narrows and becomes composed of exclusively higher values. The mean dynamic HOV increases from SS towards RI groups for all storms. The increase in mean dynamic HOV is greater when only considering cases below major hurricane intensity, at which point a deep vortex is expected in a major storm. Lower vertical wind shear (VWS) values and smaller inner-core size favor greater dynamic HOV values. Higher dynamic HOV favors intensification in moderate VWS. The VWS relationship may indicate that larger HOV values are associated with more aligned

vortices, but a more thorough analysis is needed. We hypothesize that a deeper vortex can more efficiently lower P_{min} and intensify in high dynamic HOV cases. How and if this puzzle piece fits uniquely into the TC intensification process, or is a symptom of other mechanisms, needs further investigation.

Significant differences exist between the distribution of dynamic HOV values in RI groups when compared to IN and SS prior to the change in intensity. Differences between the IN and SS groups were also found to be statistically significant in cases when excluding major hurricanes. The statistical significance of the dynamic HOV and intensification relationship is mainly defined by cases of lower intensity which possess more variability in dynamic HOV. Dynamic HOV may be useful for predicting TC intensity change in relatively weak TCs. WK cases had mean dynamical HOV values in excess of SS cases, which may be due in part to the small sample size, stronger mean current intensity, and that some of the weaker cases were major hurricanes previously. The timescale of both the growth and decay of vertical structure in a TC should be investigated in future studies. The age of the TC and its potential relationship with dynamic HOV should also be investigated. The recent example case of Eta (2020) and its extreme RI event illustrates that dynamic HOV might be useful in forecasting TC intensity change. Future work should focus on both achieving a greater understanding of the mechanisms involved with vortex height and intensity change as well as identifying ways to utilize height-based metrics for real-time TC intensity forecasting.

Chapter 3

Dynamic Vortex Height Evolution during Tropical Cyclone Rapid Intensification [2]

3.1 Introduction

Tropical cyclones (TCs) are organized convective storms capable of producing vortical circulations throughout the troposphere in their most intense states. Airborne radar analyses of category-5 Hurricane Patricia (2015) offer evidence of this extreme by showing a tangential wind field spanning the full depth of the troposphere (Rogers et al. 2017; Martinez et al. 2019). TCs at powerful intensities like Patricia are massive atmospheric phenomena which generate a large area of associated hazards; however, our understanding of the processes by which these storms attain great intensity, especially when occurring quickly, is a work in progress. Successful prediction of rapid intensification (RI), or the increase in the maximum sustained winds of a TC of at least 30 kt over a 24-hr period (Kaplan and DeMaria 2003; Kaplan et al. 2010), are historically uncommon (Trabing and Bell 2020). This is due in part to internal processes within the TC being an important determinant of RI in otherwise favorable environments capable of supporting TC intensification (Hendricks et al. 2010). TC intensity forecasts are continually improving relative to past performance metrics (Cangialosi et al. 2020) indicating encouraging progress in our ability to predict rapid intensity changes. Research efforts focused on internal processes that drive TC intensity change are important to improving forecasts. Much of this past work explores aspects of vortex structure, with radial and azimuthal structure receiving the bulk of the attention in comparison to the vertical structure of the TC vortex, about which there is still much to learn (Chen et al. 2023).

The work presented in Chapter 2 is published in DesRosiers et al. (2023), henceforth referred to as D23. D23 evaluated TC vertical structure in a large dataset of kinematic analyses gener-

[2]The results contained in Chapter 3 are in review at the *Journal of Geophysical Research: Atmospheres.*

ated from tail Doppler radar (TDR) data collected during TC reconnaissance flights (Fischer et al. 2022). The study evaluated different quantities to determine the height of the vortex (HOV) and the relationships these quantities have with current TC intensity as well as intensity change. A quantity termed dynamic HOV (DHOV), defined as the height at which the maximum winds in the azimuthally-averaged tangential wind field decay to 40% of the maximum at 2-km altitude in each analysis, demonstrated a relationship with intensity change. Grouping DHOV values into intensity change groups defined by changes in P_{min} over the 24-hr period following observation revealed that a tall vertical vortex structure was always present in storms preceding periods meeting a pressure-based RI definition. The observed relationship between DHOV and intensity change is intriguing, but the physical nature of this relationship has yet to be explored. Previous observational (Fitzpatrick 1995) and modeling (Peng and Fang 2021) studies suggest that TCs with tall tangential wind fields are more likely to intensify at greater rates. TC vertical structure should exert control on intensity change as the minimum surface pressure (P_{min}) is hydrostatically linked to geopotential height falls aloft in a strengthening TC. However, a more detailed observational analysis which evaluated vertical vortex structure using the decay of tangential winds normalized to the 2-km maximum did not report a relationship similar to that of D23 (Stern and Nolan 2011; Stern et al. 2014). These studies were limited to 8-km altitude and below by an older dataset preceding upgrades to the sensitivity of the TDR (Aircraft Operations Center 2016), which allowed for improved TC observation in the upper levels of the atmosphere.

Further study of interactions between vertical wind shear (VWS), which is a change in magnitude and direction of environmental winds with height, and TC intensity is necessary to better understand the TC intensification process (**?**). A relationship between environmental VWS and DHOV is noted in the findings of D23. Large, or “tall", DHOV values are favored in lower VWS environments while small, or “short", values are more common when VWS is higher. VWS acts to tilt the vortex downshear, causing the low- and mid-level circulation to become vertically misaligned (DeMaria 1996). Vortex tilt resulting from VWS can inhibit intensification until vertical realignment of the circulation occurs (Rios-Berrios et al. 2018). A tilted, asymmetric vortex strug-

gles to project strong tangential winds in the azimuthal average taken about storm center during the determination of DHOV. Therefore, smaller DHOV values may not be “short" TCs, but rather vortices tilted by environmental VWS. The “tall" DHOV values necessary for RI in D23 may be indicative of TCs that are vertically aligned. DHOV should not be exclusively determined by the status of vortex alignment. The tangential wind field of the vortex continues to grow vertically during aligned TC intensification. The vertical growth process was characterized in TDR observations of the RI of Hurricane Michael (2018) as both a dynamic and thermodynamic process (DesRosiers et al. 2022). Strengthening upper-level rotation increased the DHOV and was coupled via thermal wind balance with a developing upper-level warm core that aided in decreasing the P_{min} of the intensifying TC.

Upper-level warm core development in TCs is not solely a tropospheric process. During the record-setting RI of Hurricane Patricia (2015), a warm core developed at the interface between the upper-troposphere and lower-stratosphere (UTLS), evidenced by novel in-situ upper-level observations (Duran and Molinari 2018). Numerical model simulations indicate a key contributing factor of UTLS warm-core development is descent of warm stratospheric air into the eye (Ohno 2015). The descent is a response to diabatic heating from deep convection accompanied by growing inertial stability from the strengthening cyclonic circulation capable of trapping the heating locally (Chen and Zhang 2013a). The DHOV metric introduced in D23, and employed again in this study, can bridge the gap as a continuous vertical structure diagnostic which is informative during the earlier, tilt-susceptible TC development phase and the aligned vortex intensification phase in a continuous fashion. Investigation of changes in DHOV throughout the TC lifecycle in observations and numerical model simulations can help bolster our understanding of vertical vortex structure and its relationship with TC intensity change.

The analysis presented herein aims to further discern the physical meaning of the DHOV metric. In section 3.2, observational data helps characterize the relationship between DHOV and VWS-induced vortex tilt with greater detail. Section 3.3 calculates and tracks the evolution of DHOV within an ensemble of simulated TCs evolving in the presence of VWS. Section 3.4 describes dif-

ferences in DHOV and intensity which arise in simulated TCs in a control and test simulation, in which a concentrated jet of upper-level VWS limits upper-level vortex development. Section 3.5 discusses the findings of this study and how they relate to existing literature. Conclusions are summarized in section 3.6.

3.2 Observed Relationship between DHOV and Vortex Tilt

The DHOV analysis generated in D23, using the Tropical Cyclone Radar Archive of Doppler Analyses with Recentering (TC-RADAR) dataset (Fischer et al. 2022), are revisited with an updated version of TC-RADAR (v3k) to gain greater insight into the relationship between DHOV and vortex tilt induced by environmental VWS. The merged TC-RADAR kinematic analyses are created using TDR data from aircraft reconnaissance missions into storms in the northern Atlantic and eastern and central north Pacific basins. The calculation of DHOV in TC-RADAR is illustrated with an analysis of Hurricane Dorian (2019). Merged tangential wind analyses in TC-RADAR are converted from Cartesian (Fig. 3.1a) to cylindrical coordinates and the resulting cylindrical field is azimuthally averaged and normalized to its maximum value at 2-km altitude (Fig. 3.1b). DHOV is defined as the height at which the tangential wind at the radius of maximum wind (RMW) decays to 40% of its maximum value at 2-km altitude. Calculation of DHOV is mostly consistent with the methodology described in D23, however, the RMW is now defined using the tangential wind field (purple contour; Fig. 3.1b) rather than the full wind speed field composed of meridional and zonal components of flow (cyan contour; Fig. 3.1b). The resulting DHOV values using the tangential-wind-defined RMW are largely similar to the wind-speed-defined RMW DHOV values, with those in the Dorian sample case (asterisks; Fig. 3.1b) being identical. The relationship between intensity change and DHOV was present in D23 using either RMW definition, but the wind speed field definition was favored in that study given a slight increase in the statistical significance of the relationship. In the current study, the use of model simulations were found to have larger sensitivity in DHOV due the presence of stronger radial outflow in the clear air of the eye compared to radar observations where winds are only available where radar scatterers are present. The clear air radial

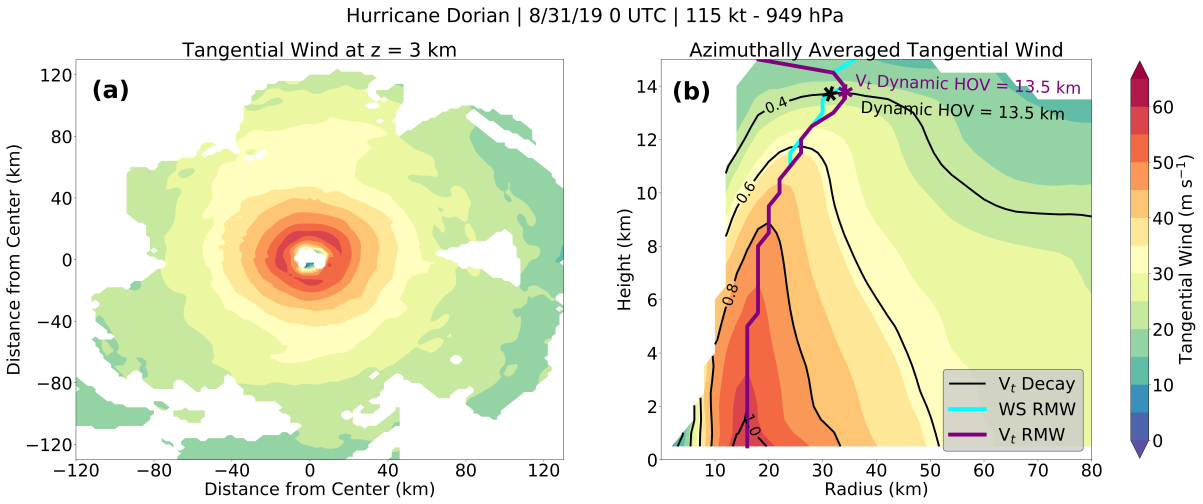

Figure 3.1: (a) Merged tangential wind analysis at a height of (z) of 3 km from TC-RADAR in Hurricane Dorian at Category-4 intensity and (b) the azimuthally-averaged tangential wind field. The radius of maximum winds (RMW) is denoted by a cyan contour and purple contour when defined by total wind speed (WS) and tangential wind (V_t), respectively. Black contours are V_t divided by the maximum value of V_t found at the RMW at z of 2 km. The dynamic HOV values are given for each RMW determination (asterisks; b)

wind produces RMWs which were on the inner edge of the eyewall and led to some undesirable sensitivity in the calculation of the height of the cyclonic vortex.

In addition to the calculation of the RMW and DHOV, observed vortex tilt values corresponding to each case are calculated between 1- and 6-km altitude using the vertical profiles of tilt magnitude available in TC-RADAR generated by Fischer et al. (2022). An accurate measurement of DHOV in TC-RADAR is only retained for analysis in cases with P_{min} less than 1000 hPa, distance to land greater than 50 km, and sufficient time over-water to establish a subsequent intensification rate. We first investigate the direct relationship between DHOV and vortex tilt shown in Fig. 3.2. There is a little relationship for tilt values less than 10 km, and a negative relationship for larger tilt values corresponding to lower DHOV values. A relationship between tilt, DHOV, and intensity is also evident, with the storms having higher DHOV and smaller tilts generally being more intense.

Figure 3.3a shows the distribution of DHOV as a function of intensity change and current intensity (colorbar). As in D23, intensity change groups are determined by 24-hr rate of change in P_{min} following analysis time. RI is defined as a drop in P_{min} greater than 21 hPa, while strengthening storms that do not meet the RI threshold are in the intensifying (IN) group, and changes in

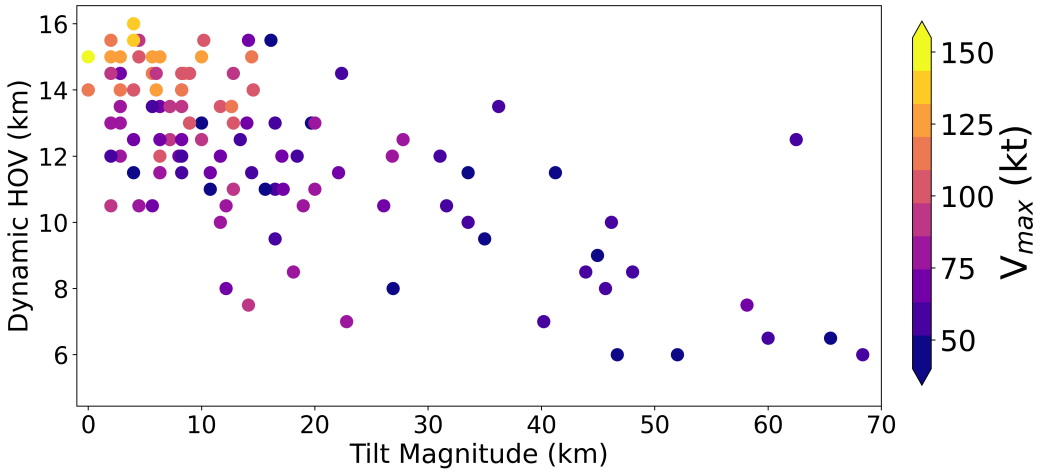

Figure 3.2: Observed dynamic HOV values in TC-RADAR versus their corresponding vortex tilt magnitudes between 1- and 6-km heights. The intensity (colorbar) is given as the maximum sustained wind (V_{max}) at analysis time.

P_{min} from -5 hPa to + 5 hPa classify as steady-state (SS). Increases in pressure greater than 5 hPa qualify for the weakening (WK) group. The distribution of DHOV values narrows towards exclusively high values ($\geq$ 10 km) in the RI group, similar to the results shown in D23. Defining aligned vortices as those with tilt magnitudes $<$ 10 km and retaining only that subset of the cases shows that all observed aligned TCs exhibit DHOV values of 10 km altitude or greater (Fig. 3.3b). The relationship between DHOV and RI discovered in D23 is no longer present, since all values are consistent with those in the RI group. The result of restricting the sample to only aligned vortices is consistent with alignment being a necessary but insufficient condition for rapid intensification (Rios-Berrios et al. 2018). Another important aspect of Figure 3.3b is that there are no observed instances of “short" TCs in aligned storms. The TCs deemed “short" by the DHOV metric were all vertically misaligned between their low- and mid-level circulation centers rather than being shallow, aligned vortices.

The color shading of the dots in Fig. 3.3b indicates there is a positive relationship between intensity and the DHOV axis in the aligned cases. The general relationship is more evident when the DHOV of aligned cases is plotted against intensity (Fig. 3.4). There is more spread of DHOV values in weaker storms, but as TCs approach and attain major hurricane intensity (Category 3+; P_{min} $\leq$ 960 hPa) as defined by the pressure-based intensity scale proposed by Klotzbach et al. (2022a),

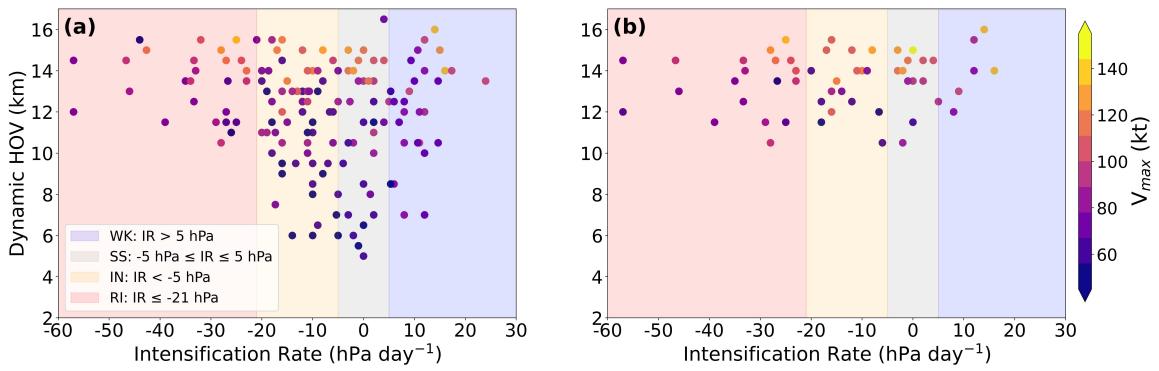

Figure 3.3: Dynamic HOV as a function of 24-hr intensity change rate. Intensity of storm at analysis time (colorbar) and intensity change groups (shaded) are shown with intensification rate (IR) bounds for groups given (legend). The quantity defined by tangential wind RMW is shown for (a) all cases and (b) cases with vortex tilt less than 10 km.

the upward trend indicates continued vertical growth of the vortex. The most intense TCs have the highest DHOV values, suggesting that the metric still contains additional useful information about vertical structure in aligned TCs as well as tilted ones. The signal for vertical growth of the vortex during intensification seen here is consistent with observations in DesRosiers et al. (2022), but the further analysis with respect to tilt suggests that DHOV may mean different things depending on whether the storm is tilted or aligned. Since the observations from TC-RADAR are snapshots at different stages of the TC lifecycle in different storms, it is difficult to assess whether the changing DHOV values are indicative of a vertical alignment or vertical growth process. Further analysis with numerical models is required to improve the interpretation of the DHOV metric throughout the full TC lifecycle.

3.3 Dynamic Vortex Height Evolution in Moderate Vertical Wind Shear

A 20-member ensemble of idealized TC simulations with the Advanced Research version of Weather Research and Forecasting (ARW-WRF; version 3.1.1) model (Skamarock et al. 2008) is employed here to gain a greater understanding of the DHOV metric in TCs impacted by moderate deep-layer VWS. The ensemble was used by Tao and Zhang (2014) and Nam et al. (2023) as part

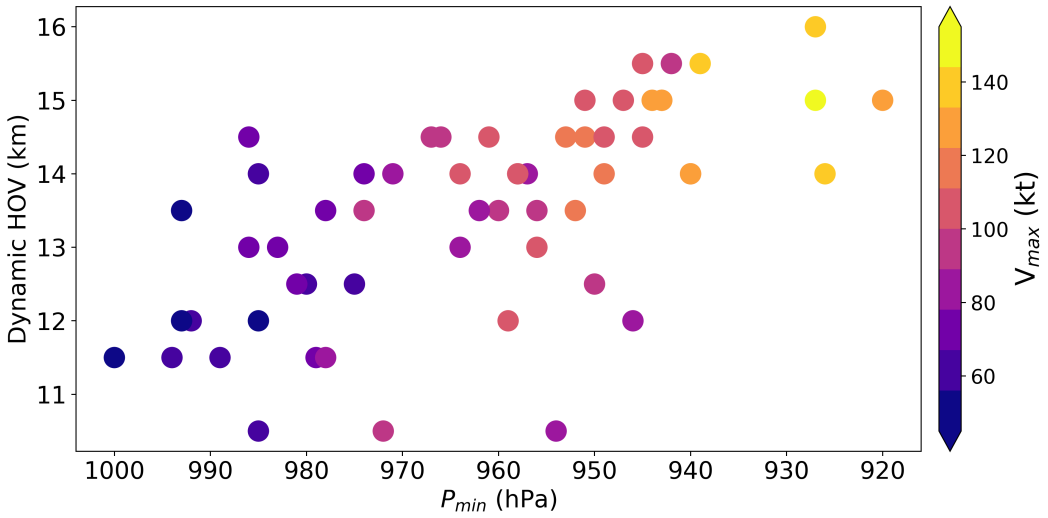

Figure 3.4: Dynamic HOV as a function of storm intensity, evaluated with P_{min}. Wind-based intensity of storms at analysis time is shaded for each case plotted (colorbar).

of a larger set of simulations with varying VWS magnitudes, sea surface temperature (SST) values, and atmospheric moisture profiles. The 20-members used herein are the SH7.5/Moist100 ensemble in Nam et al. (2023). Simulations are initialized with a modified Rankine vortex profile with a 15 m s^{-1} tangential wind maximum at 135-km radius. Figure 3.5 shows the VWS profile that would be classified as moderate (7.5 m s^{-1}) by the climatology described in Rios-Berrios and Torn (2017), introduced via the point downscaling method described in Nolan (2011). The thermodynamic profile is initialized using the non-Saharan air layer (SAL) mean hurricane season sounding (Dunion and Marron 2008) and 29° C SSTs. Random perturbations are added to the boundary layer moisture to generate the 20-members. The simulations use the WRF single-moment 6-class microphysics (WSM6) scheme (Hong et al. 2004), Yonsei University (YSU) boundary layer scheme (Hong et al. 2006), and no radiation schemes or cumulus parameterization. There are 41 vertical levels with a model top at 20-km altitude. Three two-way nested domains have horizontal resolutions of 18, 6, and 2 km, with the innermost domain analyzed in this study having a dimension of 720 km x 720 km with 360 x 360 grid points. The simulated TCs are integrated forward on an f-plane at 20° N for 9 days. See Tao and Zhang (2014) and Nam et al. (2023) for additional details on the simulations.

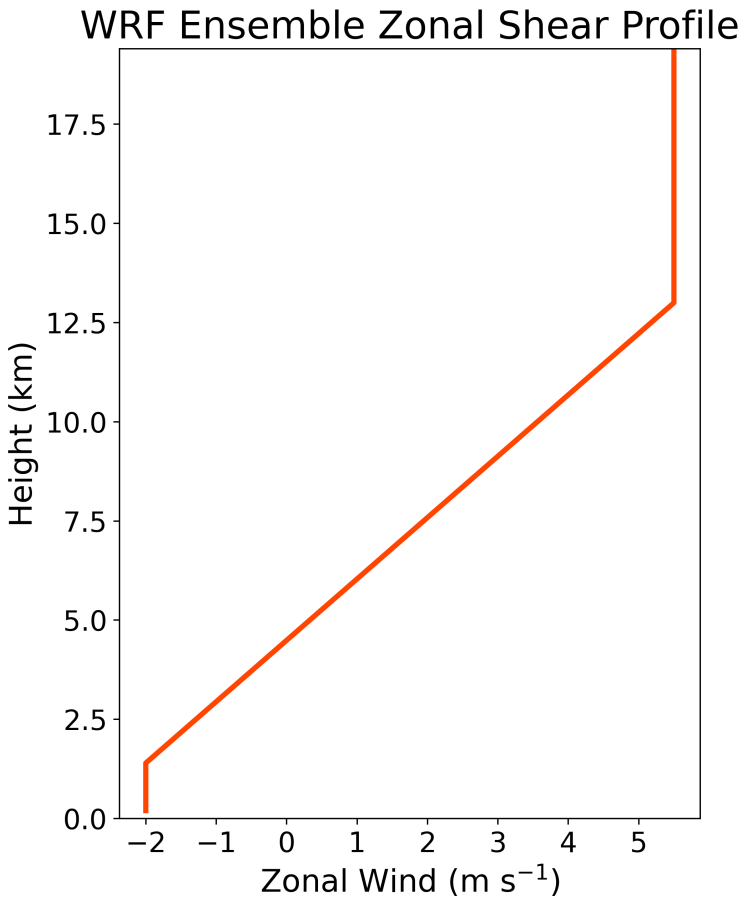

Figure 3.5: Prescribed moderate environmental zonal wind shear in the WRF ensemble simulations.

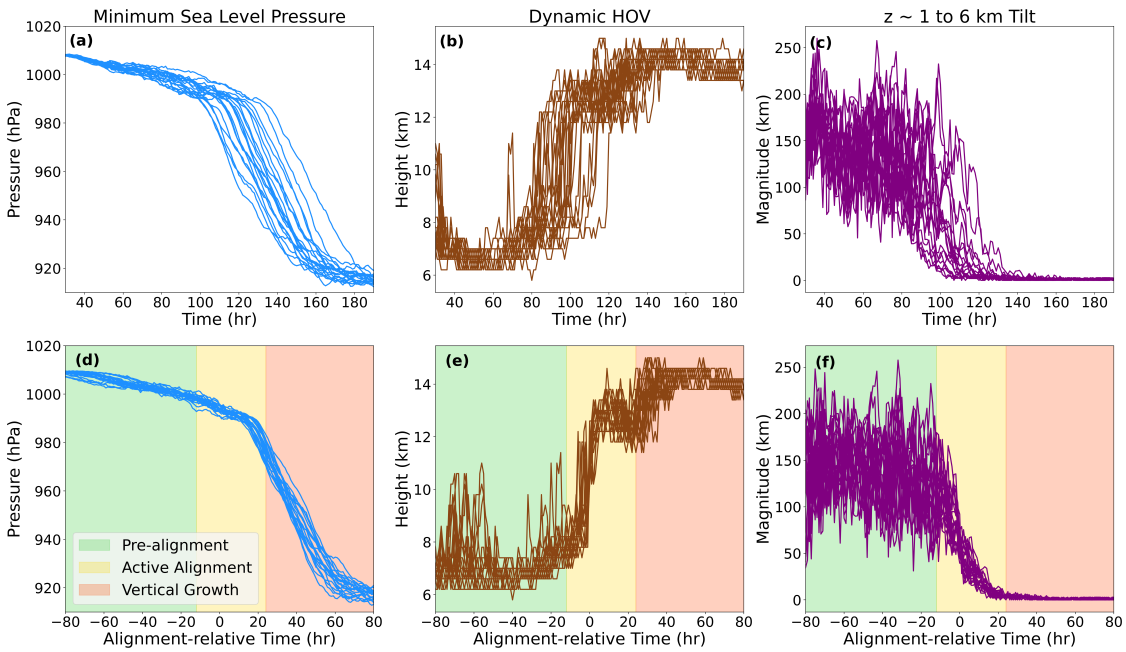

Figure 3.6: Evolution of all 20 WRF ensemble members. The (a) P_{min}, (b) Dynamic HOV values, (c) height (z) of 1 to 6 km vortex tilt values are given as time series in the original model time. The same variabls are given with the time now centered on time of alignment (d,e,f). The shading denotes the time periods of the pre-alignnment (green; -80 to -12 hrs), active alignment (yellow; -12 to +24 hrs), and vertical growth (+24 to +80 hrs) stages of intensification.

All variables interpolated to height coordinates from WRF sigma levels with 400-m spacing between interpolated levels. Vortex tilt calculations between roughly 1- to 6-km altitude performed by Nam et al. (2023) are used for time series analysis of the ensemble set. Note that the terms “roughly" and “approximately" when used with respect to altitudes and radial locations in model simulation discussions indicate that the closest interpolated location to this point has been used in its place. Results presented in this study are invariant to the choice of an interpolated coordinate above or below the approximate point so the behavior neighboring these layers is consistent. The vertically interpolated zonal and meridional winds are transformed into a tangential wind field in the innermost storm-following domain. The tangential winds are calculated and then azimuthally averaged with a tangential-wind-defined RMW used to calculate DHOV at each model time step consistent with the process used for the TCC-RADAR analyses.

The 20-member WRF ensemble allows for analysis of the evolution of DHOV and other storm metrics with greater temporal resolution than the observations. All members experience initial

vortex tilt induced by the VWS, followed by alignment and RI (Fig. 3.6a,c) although the timing is slightly different in each simulation. A time series of DHOV values is shown in Fig. 3.6b to characterize the vertical structure of the vortex. Initially, DHOV values are predominantly below 8 km and vortex tilt values are greater than 100 km with substantial variability. As the vortex comes into alignment in each member, there is a large jump in DHOV. The moment at which DHOV exceeds 10 km and remains above that height for all subsequent model time steps is considered here to be the time of alignment, which corresponds to an average tilt of about 50 km. For efficient comparison of all ensemble members, the time series for all members are shifted with respect to this time, which is set to hour 0. The shifted time series is shown in Figs. 3.6d-f and reveal a similar temporal evolution of P_{min}, DHOV, and tilt.

Three distinct phases in the DHOV are apparent that are shaded in green, yellow, and red backgrounds and correspond to pre-alignment, a period of active alignment, and post-alignment vertical growth. The pre-alignment phase prior to the DHOV jump is characterized by slowly falling P_{min} (Fig. 3.6d), low and sometimes erratic DHOV values (Fig. 3.6e), and large vortex tilt (Fig. 3.6f). During active alignment, the DHOV values rise sharply as the pressure continues to slowly fall and the tilt steadily decreases. As the tilt declines, the DHOV values show a jump followed by a drop to a minimum height near 12 km (Fig. 3.6e). Following the relative minimum in DHOV, the vortex height then grows towards a maximum at or above 14-km altitude. We denote that relative minimum as the start of the post-alignment vertical growth phase which is near the onset of RI with rapidly falling P_{min} (Fig. 3.6d) and tilt magnitudes near-zero (Fig. 3.6f).

The relationship between DHOV and tilt across the WRF ensemble is shown in Fig. 3.7. A wind intensity (colorbar) is estimated by taking the maximum azimuthally-averaged tangential wind value at 2-km height. A similar relationship is seen as in the observations, with lower DHOV associated with higher tilts. The distribution in the ensemble is approximately bimodal, with two distinct clusters of DHOV above and below 10 km associated with small and large tilt. All DHOV values below 10 km are associated with tilts greater than 50 km and weaker intensities. The first 12 hours of model time in each member is excluded to remove outliers with no tilt and low DHOV

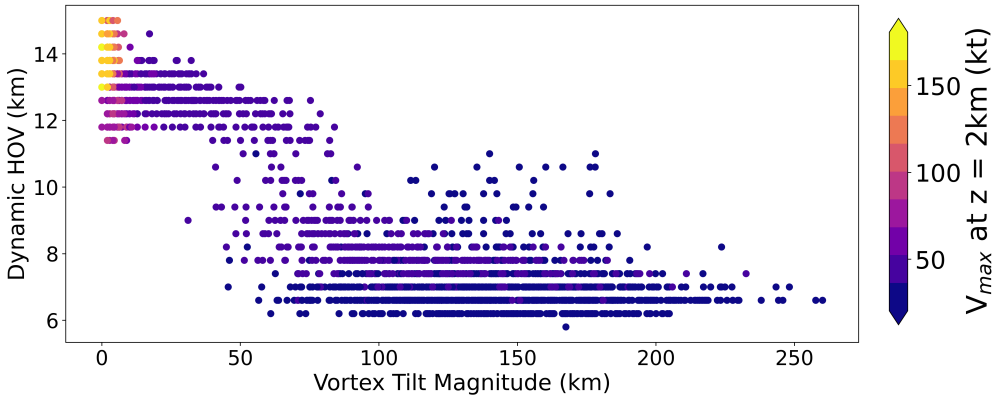

Figure 3.7: DHOV at all times across all members of the WRF ensemble simulations versus their corresponding vortex tilt maginutes between roughly 1- and 6-km heights. The intensity (colorbar) is estimated via the maximum value of azimuthally averaged tangential wind at a height (z) of 2 km.

associated with the model initialization time where the simulated vortices have yet to be impacted by the VWS. DHOV values above 10 km show a relationship with tilt and intensity similar to the observations, with the strongest storms having the smallest tilt. The presence of larger tilt values here as compared to the observed samples (Fig. 3.2) is due to coverage limitations of airborne radar which may struggle to capture the entire wind field of a TC with high magnitude vortex tilt. The distribution of DHOV values provides further evidence that 10 km is a reasonable demarcation between misaligned and vertically aligned storms.

Since all members undergo a similar evolution in this idealized simulation, a representative member with near average values of the ensemble is selected to illustrate the changes in vertical structure in the simulated TCs (Fig. 3.8). In addition to the prior metrics, the maximum tangential wind velocity near 2-km height (Fig. 3.8b) and upper-level temperature perturbation (Fig. 3.8e) are tracked in time. The latter quantity is an average of the perturbation temperatures between 12- and 16-km altitude within the 2-km RMW. The perturbation is in reference to the azimuthally-averaged profile at roughly 300-km radius well away from the TC center. The low-level tangential wind increases slowly during the pre-alignment and active alignment phases, while the upper-level temperature perturbation changes very little. Just past alignment-relative hour +10, the 2-km tangential winds begin to increase quickly and the pressure falls rapidly signaling the onset of RI.

Shortly after RI onset near the +20 alignment-relative hour, the upper-level warm core perturbation temperature begins to increase rapidly in all members.

The azimuthally-averaged vertical structure of perturbation temperatures and tangential winds at specific times of interest (gray dashed lines) are shown for the representative member in Figs. 3.8f-j. At alignment-relative model hour -30, the tangential wind field is weak and concentrated in the lower levels (Fig. 3.8f) resulting in low DHOV. The TC warm core temperature perturbation is concentrated below 6-km altitude at this time. At alignment hour 0, the tangential wind field appears somewhat disorganized, but is beginning to have greater coverage with respect to height (Fig. 3.8g), which nearly doubles the DHOV from the previous time of interest. The warm core temperature perturbation is stronger, but is still concentrated in the lower-troposphere. 10 hours after alignment time, the tangential wind field appears slightly more organized (Fig. 3.8h), although the maximum value is just slightly higher than at hour 0. Dynamic HOV increased slightly but the strongest temperature perturbation remains in the lower troposphere and has become more diffuse with a weaker maximum. Between model hours 10 and 20, the DHOV decreases slightly following its jump and there is a noticeable change in the thermal structure of the TC warm core. The near-surface tangential winds become more intense and the maximum of the temperature perturbation is centered near 10 km (Fig. 3.8i). The slightly decreased DHOV value is just above the warm-core maximum at this time which is likely related to an increase in the DHOV-determining threshold value and adjustments with respect to thermal wind balance between the developing warm-core maximum and the tangential wind field. By hour 50, RI is nearly complete and DHOV remains steady at its maximum. The tangential wind field is considerably larger in both magnitude and vertical extent (Fig. 3.8j). The warm core temperature perturbation is maximized near 8-km height but remains strong up to and near the level of the DHOV value, and decays rapidly above it along with the tangential winds.

Inspection of the horizontal wind structure in the representative member at the 1- and 6-km levels at the times of interest is helpful in understanding the importance of vortex tilt to the evolution of vertical structure. At hour -30, the low level circulation is weak and asymmetric (Fig. 3.9a).

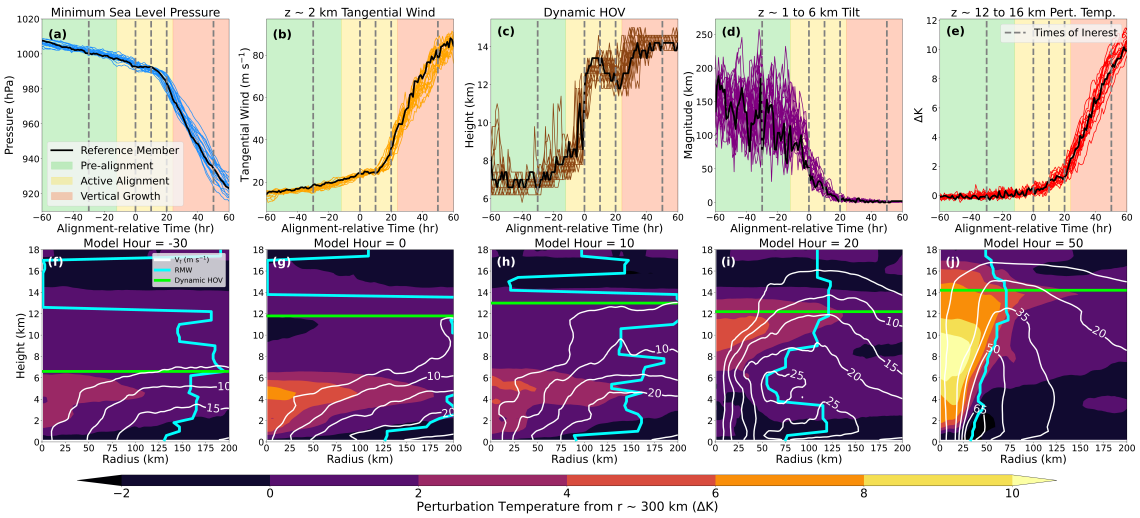

Figure 3.8: Time series plots for all members showing (a) P_{min}, (b) maximum azimuthally-averaged tangential wind at altitude (z) of 2 km, (c) dynamic HOV, (d) magnitude of $\sim$ 1 to 6 km vortex tilt, and (e) averaged perturbation temperature from approximately 12- to 16-km height within the RMW at approximately 2-km height. The phases of intensification are indicated by background shading (legend). A representative member (black line; a,b,c,d,e) is highlighted with the temperature perturbation (colorbar) shown with respect to an azimuthally-averaged reference profile at radius (r) of roughly 300 km and tangential winds (white contours) given at several times of interest (gray dashed lines; a,b,c,d,e). The RMW and DHOV are denoted at each reference time by cyan and green lines, respectively. The times of interest are alignment relative model hours (f) -30, (g) 0, (h) 10, (i) 20, and (j) 50.

The mid-level circulation is displaced to the east by the westerly VWS (Fig. 3.9b). Tilt magnitude is large at this time (Fig. 3.8d) as evidenced by the mismatch in location of TC centers at each level obtained with the pressure centroid method of Nguyen et al. (2014). Winds are weak at both levels at hour 0 (Fig. 3.9c,d), but the tilt is reduced and the centers are much closer. The 6-km rotational flow about the center is much better defined, explaining the jump in DHOV occurring at this time (Fig. 3.8c). At hour 10, when DHOV reaches its initial post-alignment peak, the centers continue to move closer to one another (Fig. 3.9e,f), although not yet fully aligned, and the wind field becomes more symmetric and well-defined at the 6-km level. DHOV is near its minimum in the active alignment phase during hour 20. Although the organization of the wind field has improved at both levels (Fig. 3.9g,h), the most drastic improvement and intensification of the winds occurs in the lower levels, which reduces DHOV by increasing maximum winds at 2-km faster than the upper-level winds (Fig. 3.8b). By the end of RI at hour 50, the wind fields at both levels are strong,

well defined, and clearly vertically stacked (Fig. 3.9i,j), which is indicative of a vertical structure that maximizes the DHOV metric.

3.4 Dynamic Vortex Height Evolution During Rapid Intensification in the Post-alignment Vertical Growth Phase

In the WRF ensemble, deep-layer moderate VWS was imposed during the entire TC lifecycle. The VWS causes misalignment that the TC must overcome before undergoing RI, as evidenced by the evolution of DHOV from shallow values to higher values during the active alignment phase. In this section, we devise an additional set of numerical experiments to examine the evolution of DHOV during the post-alignment vertical growth phase. We hypothesize that the low to mid-level alignment is primarily disrupted by the VWS in the low to mid-troposphere, and that aligned storms with VWS confined to the UTLS would not need to undergo the active alignment phase and could move directly to the third phase of development. We further hypothesize that the vertical growth of DHOV above 10 km is important and indicative of structural evolution and intensification during RI. To test these hypotheses, additional idealized modeling simulations are performed using a pair of Cloud Model 1 (CM1; version 21.0) (Bryan and Fritsch 2002) simulations. The change from WRF to CM1 also allows us to test the sensitivity of the conclusions regarding DHOV using a different dynamical core and physics parameterizations to ensure that the metric still provides a similar interpretation in a different modeling framework.

Both simulations are initialized with a modified rankine vortex with maximum winds of 15 m s^{-1} located at 75-km radius from storm center consistent with defaults for TC initialization set in the model and similar to the WRF initial vortex. The moist tropical profile in Dunion (2011) is used to initialize the thermodynamic environment, which is slightly less moist than the Dunion and Marron (2008) used in WRF, but is qualitatively similar. The model configuration is largely similar to that described in Martinez et al. (2022). The main differences present in these CM1 experiments from the referenced study are 2-km horizontal resolution, SSTs of 29° C, and use of the Thompson microphysics scheme (Thompson et al. 2004), which has demonstrated skill in TC

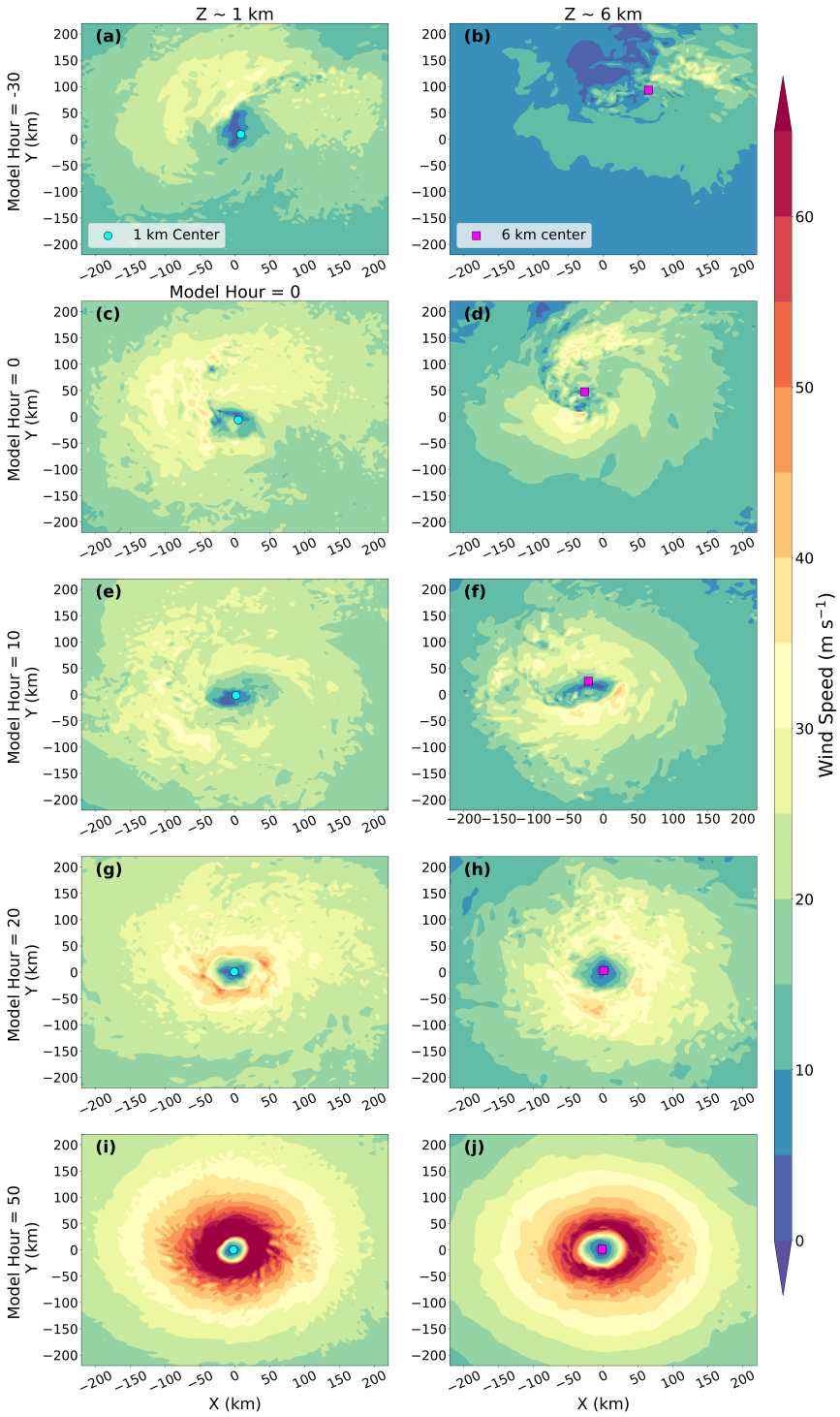

Figure 3.9: Total u and v component wind speed (colorbar) given for the reference member at height (z) of approximately 1 km at alignment-relative model hours (a) -30, (b) 0, (c) 10, (d) 20, and (e) 50. The winds near 6-km altitude are also shown for hours (f) -30, (g) 0, (h) 10, (i) 20, and (j) 50. Vortex centers determined by the pressure centroid are given at the $\sim$ 1 km (cyan circles) and 6 km (magenta squares) levels for each model hour.

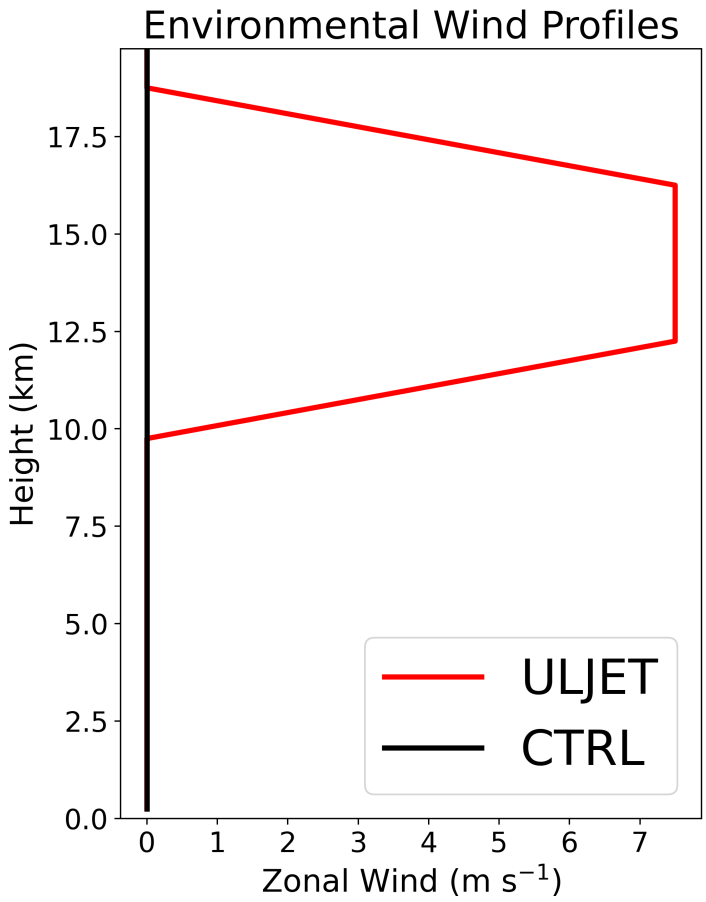

Figure 3.10: Prescribed calm environmental zonal wind profile in the control simulation (CTRL; black) and the profile of the upper-level jet (ULJET; red) simulation.

model forecasts (Choudhury and Das 2017). A simple Louis-type scheme is used in the planetary boundary layer (Bryan and Rotunno 2009) and the Rapid Radiative Transfer Model for General circulation models (RRTMG) scheme is used for shortwave and longwave radiation. The storm-following horizontal grid is composed of 540 x 540 grid points and is 2000 km x 2000 km on an f-plane at 20° N. Uniform 2-km horizontal resolution is maintained over the innermost 620 km x 620 km and stretches outward to 10-km resolution at the domain boundaries. The vertical grid stretches from 50- to 500-m resolution from 0- to 5.5-km altitude where a uniform 500-m resolution is maintained until model top at 25 km, resulting in 59 vertical levels.

The two simulations are differentiated by environmental VWS profiles shown in Fig. 3.10. The control simulation, referred to as CTRL, has no background flow or VWS. The test simulation,

referred to as ULJET, introduces a 7.5 m s^{-1} upper-level zonal jet via the time-varying point downscaling technique (Onderlinde and Nolan 2017). The jet is constructed such that a bulk shear calculation returns the same VWS value of 7.5 m s^{-1} as the WRF ensemble when evaluated between the 850 to 200 hPa layer, despite the strongest zonal winds being focused in the upper levels above quiescent flow over much of the troposphere. The focused upper-level VWS in the jet is intended to affect the development of the UTLS warm core which forms in the CTRL simulation, while having little to no impact on the developing vortex in the lower to mid-troposphere. After allowing for initial convective development in calm flow, the VWS profile is nudged in at the boundaries in ULJET from model hours 12 to 24 consistent with the strategy of Alland et al. (2021).

The results from the WRF ensemble indicate the importance of a strengthening upper-level warm core temperature perturbation to the deep vertical structure obtained by TCs during the RI process. The additional experiments run in CM1 serve as a mechanism denial experiment in which a concentrated upper-level jet of moderate VWS strength is used to disrupt the formation of the UTLS warm core in the ULJET simulation. The TC is allowed to develop in a similar environment over the first 12 hours, and then during hours 12-24, the upper-level jet ramps up in ULJET and is maintained from hour 24 onward. Through the first 3 days of the model simulations, RI proceeds in a qualitatively similar fashion with respect to maximum surface wind speeds (Fig. 3.11a) and P_{min} (Fig. 3.11b) with the intensity of the simulated TC in ULJET lagging slightly behind CTRL. Near hour 75 and onward, the intensities begin to diverge and RI continues in CTRL while the intensity in ULJET weakens briefly. The DHOV values diverge earlier with ULJET beginning to decline around hour 60 while CTRL continues to increase the vertical extent of its tangential wind field (Fig. 3.11c). There is an initial jump in DHOV followed by a lull in growth in CTRL, but the slight decline in DHOV seen in the WRF ensemble at the end of active alignment is not present. ULJET does eventually recover from its brief weakening period and declining DHOV, but the TC intensity and height that the DHOV stays at are noticeably lower than CTRL. The differences between simulations suggest the upper-level jet halted the RI episode and served as an effective

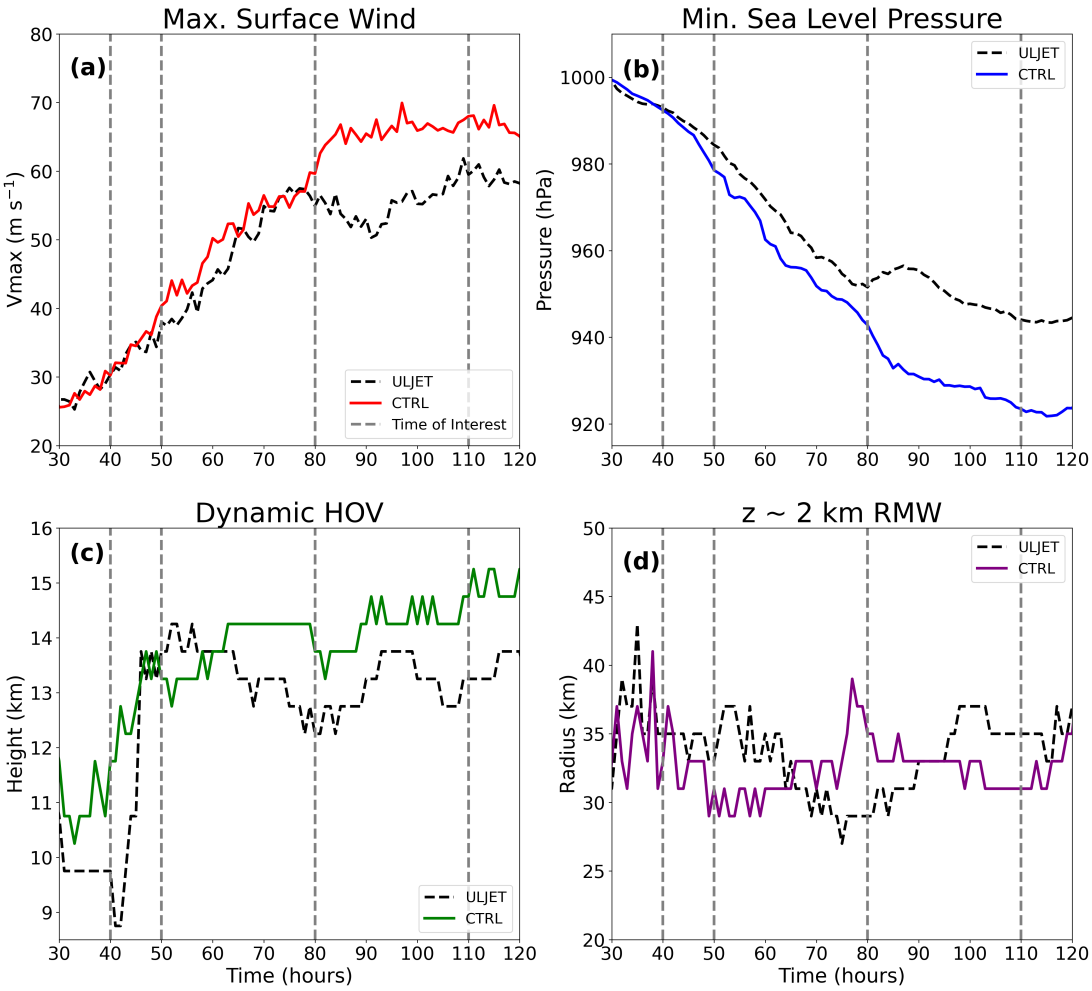

Figure 3.11: Time series of (a) the maximum surface wind (V_{max}), (b) P_{min}, (c) dynamic HOV, and (d) azimuthally-averaged RMW at a height (z) of 2 km for the control run (CTRL; solid colored lines) and the upper-level jet run (ULJET; dashed black lines) with times of interest shown (gray dashed lines).

cap on both the vertical development of the TC vortex and its surface wind intensity. Since these simulations include radiation, eyewall replacement cycles (ERCs) become more likely to occur (Trabing and Bell 2021). Secondary eyewall formation in an ERC would temporarily weaken the TC and likely decrease the DHOV. The RMW at 2-km altitude holds steady near 35-km radius in both simulations (Fig. 3.11d) over the time analyzed, confirming that ERCs did not impact the behavior of the simulated TCs, such that the differences cannot be attributed to such a mechanism.

Times of interest in Fig. 3.11 are identified to highlight differences in the tangential wind field and warm core structure (Fig. 3.12). The warm core structure is again evaluated through azimuthally-averaged perturbation temperatures from a 300-km radius reference profile similar to

the WRF ensemble. At hour 40, the wind intensities of ULJET and CTRL are similar, but the warm core temperature perturbation is more diffuse and the tangential wind field is less vertically expansive in ULJET compared to its counterpart in CTRL (Fig. 3.12a,b). At hour 50, following the initial jump in DHOV, the winds are stronger and more organized in CTRL (Fig. 3.12c,d) with a steady outward slope of the RMW (cyan contour) apparent. A warm core perturbation forms around 12-km altitude in both simulations, but is better defined and more expansive in CTRL. Intensity and DHOV values have diverged by hour 80 and the vertical structure is different as well (Fig. 3.12e,f). The warm core temperature perturbation is much weaker above 14 km in ULJET with a strong maximum forming near 6-km altitude. The maximum perturbation temperature in the eye is weaker in CTRL, but dual maxima are present near 6- and 12-km altitude. Strong cyclonic winds in the eyewall extend higher into the troposphere in CTRL. Near the peak steady-state intensity for each simulation at hour 110, the inner-core structures are quite different (Fig. 3.12g,h). The RMW is more upright in CTRL and the tangential wind field is stronger with most of its decay in magnitude occurring much higher in the troposphere, resulting in a higher DHOV than ULJET. An additional warm core perturbation temperature maxima forms above 14-km altitude. With a single perturbation temperature maximum still dominant in ULJET and a warm core that decays rapidly above 14-km altitude, the wind field in ULJET decays much faster in the upper-troposphere.

To further examine the detailed evolution of vertical structure, the strength of the tangential wind field and warm core are averaged in several vertical layers throughout the analyzed period of CTRL and ULJET (Fig. 3.13). Azimuthally-averaged fields from hour 100 of CTRL are used as a visual aid for the method of averaging. At each model time step, the tangential winds are normalized to their maximum at 2-km altitude along the RMW through the 0- to 4-km, 4- to 8-km, 8- to 12-km, and 12- to 16-km levels (Fig. 3.13a; legend). The resulting time series are given in each layer in CTRL (Fig. 3.13c) and ULJET (Fig. 3.13e). The perturbation temperature is averaged over the same layers within a box radially bounded by the center of the TC and the location of the 2-km RMW at each time step (Fig. 3.13b; legend). While the warm core grows radially with height as the RMW and eyewall slope outward, the averages are bounded by the lower-level RMW

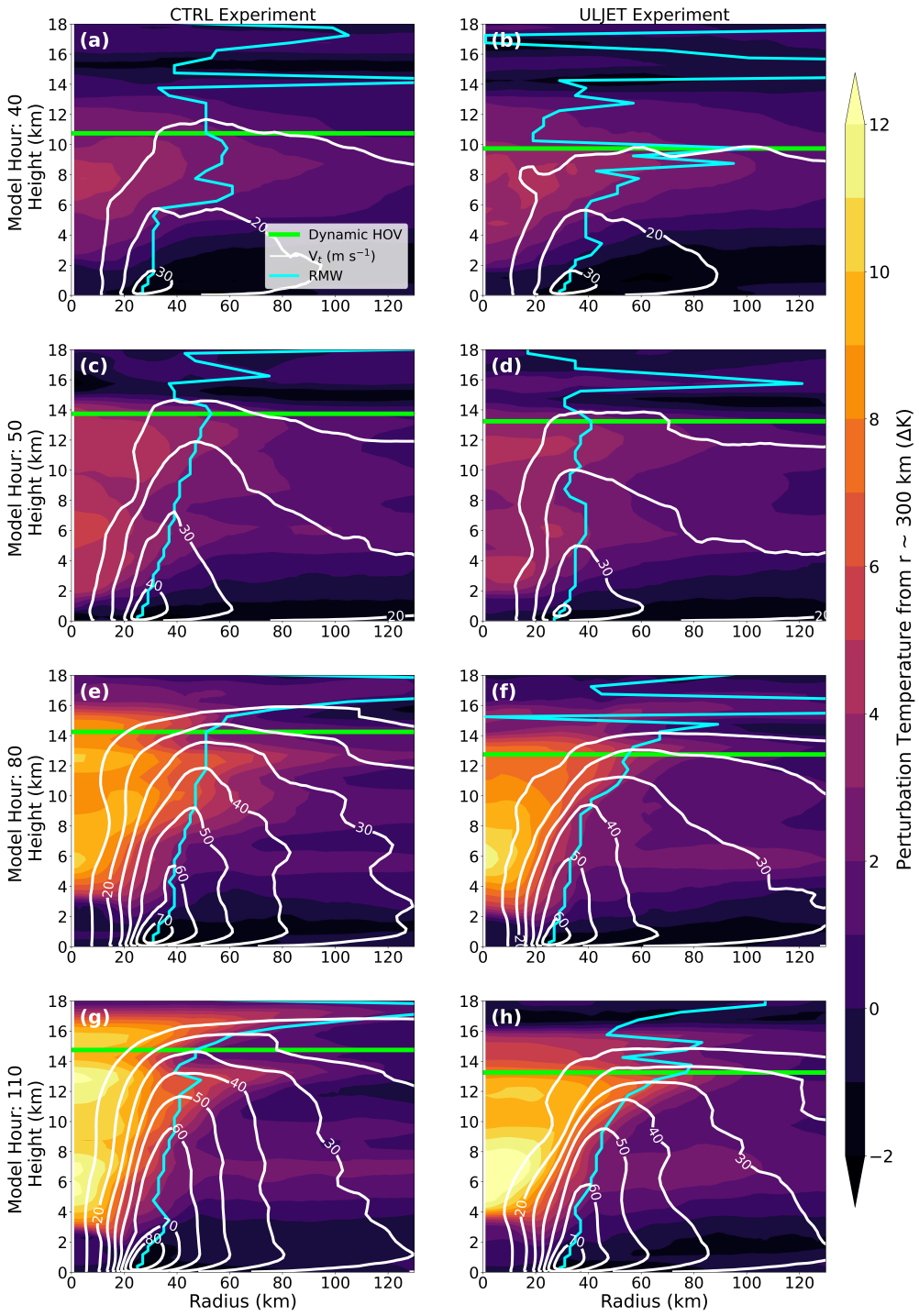

Figure 3.12: Azimuthally-averaged perturbation temperature (colorbar) from an azimuthally-averaged reference profile at radius (r) of approximately 300 km. Analyses are shown at model hours 40, 50, 80, and 110 for the control (CTRL; a,c,e,g) and upper-level jet (ULJET; b,d,f,h) simulations. The radius of maximum winds (RMW; cyan contour), dynamic HOV (green line), and tangential winds (white contours) are shown for all analyzed times.

to focus on its potential impact on the minimum central surface pressure. The time series of these averaged quantities in CTRL (Fig. 3.13d) and ULJET (Fig. 3.13f) allow for comparison of the developing warm core to the strengthening tangential winds at the corresponding levels. Winds in the lowest layer are unsurprisingly static near 1.0 in both simulations since the scaling value is calculated in this layer. The warm core is largely nonexistent through the lowest layer. Later in the simulations once the intensities have diverged, the winds and temperature perturbations in the middle two levels plateau and remain mostly static with the values being slightly larger in ULJET as compared to CTRL. The similar behavior in these levels is likely due to the environmental winds being zero through the bulk of these layers in both simulations, thus allowing for intensification of the TCs in predominantly quiescent background flow.

The most noticeable differences in the structural evolution are found in the upper-level from 12- to 16-km altitude. Following the onset of RI in both simulations, the upper-level winds and warm core intensify with the TC. The averaged winds and perturbation temperatures experience consistent growth throughout the analysis period in CTRL, with the strongest rates of increase occurring in tandem during the period of RI. Once a steady-state intensity in terms of maximum winds is reached, the average values of all quantities in the lower three levels remain static. The upper-level winds and temperature perturbation continues to grow along with DHOV as the minimum pressure drops into extreme values below 930 hPa. In ULJET, the winds and warm core increase in the upper-levels during RI. At the earlier end to the RI period in ULJET when the intensities of the simulated TCs diverge, the averaged values in this level begin to decline and never reach the values at peak intensity in CTRL. Accordingly, the DHOV and intensity is capped by the upper-level jet. Although some metrics in the upper-levels of ULJET do increase, the difference is more stark when comparing changes from 14- to 16-km in the uppermost part of the TC circulation. The UTLS warm core which has been observed and simulated (Duran and Molinari 2018; Ohno 2015) should form here in the highest levels of the troposphere. The difference in structure becomes apparent at hour 80 when the warm core temperature perturbation continues to expand vertically and DHOV is higher in CTRL (Fig. 3.13g,h). The tangential wind field is weak, but

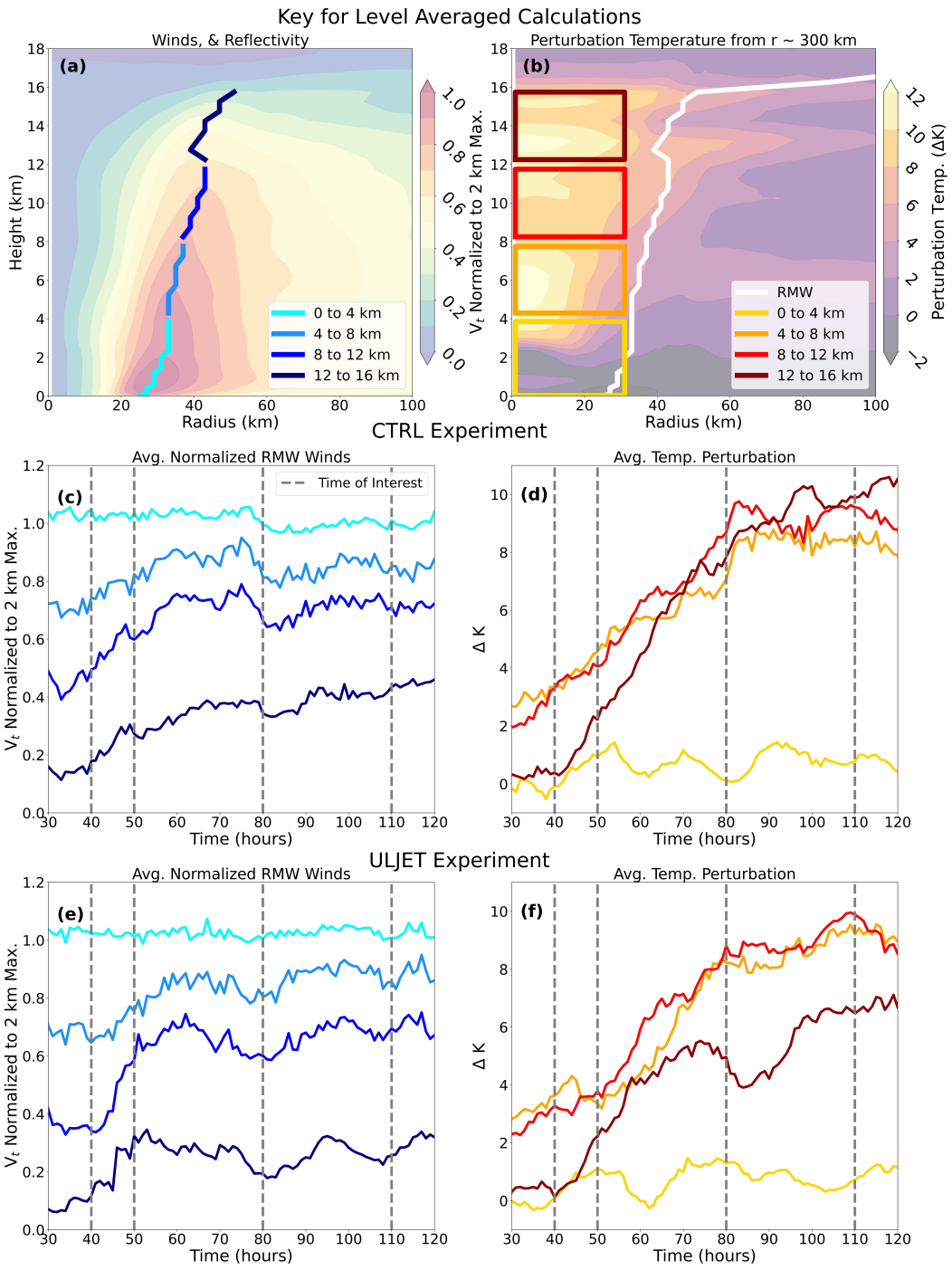

Figure 3.13: (a) Azimuthally-averaged profile of tangential winds normalized to the maximum at height (z) of 2 km (colorbar; a) at model hour 100 in the control (CTRL) run normalized to the 2-km maximum. Colored lines denote the tangential wind values averaged over specific levels (legend; a). Averaged wind values are given as time series for the (c) CTRL and (e) upper-level jet (ULJET) simulations. (b) Azimuthally-averaged profile of perturbation temperature (colorbar; b) with respect to an azimuthally-averaged reference profile at radius (r) of roughly 300 km. The radius of maximum winds (RMW) is shown as a white line. Averaged temperature values over specific levels (legend; b) are given as time series for the CTRL (d) and ULJET (f) simulations. Times of interest are given as dashed gray lines (c,d,e,f).

well defined in this level while the RMW remains upright and further radially inward in the middle and upper levels in CTRL. By hour 110 (Fig. 3.13g,h), the additional perturbation temperature maxima is present in CTRL and absent in ULJET.

3.5 Discussion

Changes to the axisymmetric azimuthally-averaged vertical structure of the vortex tangential wind field are important to TC intensity and intensification. The DHOV metric utilized in this study serves as a useful proxy for diagnosing vertical wind field structure in TCs throughout their lifecycle. Analysis of the observational dataset utilized in D23 indicates this metric is sensitive to environmental VWS with all observed “short" DHOV values being indicative of tilted vortices. The relationship between DHOV and tilt in observed TCs suggests the aircraft data analyzed in Fitzpatrick (1995) may have contained some of the earliest observational clues of the link between vortex tilt and intensification. Results of numerical model simulations add greater context to this DHOV-VWS relationship. VWS is known to cause differential advection of the low- and mid-level centers of circulation which tilts the vortex downshear (DeMaria 1996). The impact of this tilt on DHOV is apparent early in the modeled TCs of the WRF ensemble, which exhibit large magnitudes of tilt and corresponding low values of DHOV during the pre-alignment phase. As the tilt magnitude begins to decrease, there is a large jump in DHOV to exclusively higher values which are maintained as the vortex continues to become more aligned and rapidly intensify (Fig. 3.6).

Alignment in this study is defined as the model hour in which this jump in DHOV occurs. The jump in DHOV is a key characteristic of the active alignment phase. Although vortex tilt lowers considerably in the time surrounding this period, it remains present but decreasing over the $\sim$ 20 hours following the DHOV-defined alignment time. The onset of RI occurs during the latter times of this period between the jump in DHOV and the elimination of tilt as it reduces to near zero. The jump in DHOV preceding RI onset suggests the DHOV jump is a necessary, but insufficient, condition for RI. The final stages of tilt reduction being concurrent with RI onset is consistent with Chen and Gopalakrishnan (2015), who show reduction of vortex tilt continues in the early stages

of RI in the presence of VWS as a consequence of it rather than a precursor. In their simulation of Hurricane Earl (2010) which underwent RI in VWS, tilt reduces from moderate values to much lower ones similar to those found in the ensemble near the DHOV-defined alignment time. The results here indicate TC vortex alignment in VWS is likely not a discrete moment as defined here for simplicity, but more of a continuum. The alignment process observed in the WRF ensembles begins with a dramatic improvement of the coherence of the axisymmetric projection of the tangential wind field with respect to height followed by formation of an upper-level warm core temperature perturbation at the onset of RI, which grows rapidly as RI continues.

Analysis of key model times in a representative ensemble member show negative perturbation temperatures at the storm center near 12-km altitude at hour 0, suggesting the increase in upper-level tangential winds during alignment precedes the development of the upper-level warm core (Fig. 3.8). After the initial jump in DHOV, a small decline and subsequent growth of DHOV in concert with the strengthening upper-level warm core proceeds in accordance with thermal wind balance in this baroclinic upper-level region of the model TCs. This behavior at the end of the active alignment phase preconditions the TC structure for the vertical growth phase of RI that follows. The jump in DHOV may be an early indicator of a sheared TC obtaining the vertical structure necessary to develop an upper-level component of its warm core and rapidly align during the initial stages of RI. The jump in DHOV is more accurately referred to as “adequate alignment" for TC intensification versus a total reduction of vortex tilt. Deep atmospheric convection is an essential component of TC intensification which is a more efficient agent of the process when located in the inner-core and preferentially occurring within the RMW (Rogers et al. 2013) in the region of high inertial stability (Schubert and Hack 1982). An analysis of convective characteristics in observed TCs showed deep convection is preferentially located near the mid-level center (Fischer et al. 2024). The movement of the mid-level center into the vicinity of the low-level center produces the jump in DHOV and also signals the arrival of deep convection to the TC inner core which is important to facilitating intensification. Nam et al. (2023) analyzed convective behavior

in a larger set of ensembles including the WRF ensemble used here and noted deep convection near the mid-level center organizing near the low-level center as vortex tilt decreases.

Once the adequate alignment condition is met, a developing upper-level circulation and associated warm core are important features in the sheared ensemble simulations as tilt finishes decreasing and RI ensues. The CM1 simulations attempt to isolate the impact of development in this level on the RI process during the vertical growth phase of intensification in idealized TCs by using environmental VWS to hinder its formation via a concentrated upper-level jet. Finocchio et al. (2016) varied both the height of the maximum VWS magnitude and the depth over which the shear occurs in idealized modeling experiments and found low-level VWS is more effective at tilting the vortex and VWS concentrated in shallow layers are less favorable to TC intensification. Fu et al. (2019) found that concentrated VWS higher in the troposphere in numerical model simulations proved most effective at ventilating the upper-level warm core through dilution of the high-entropy air by an influx of low-entropy air. The simulated TC in ULJET behaved in a manner consistent with the results of these previous studies, although the upper-level jet used here is concentrated in higher atmospheric levels than those tested in the studies previously mentioned. The upper-level jet proved effective at disrupting TC intensification in the upper levels, but the absence of lower-level VWS allowed the modeled TC to maintain alignment of the low- and mid-level centers throughout intensification as evidenced by the absence of low DHOV values in both CM1 simulations. The duration of RI and peak steady-state intensities reached in CTRL and ULJET after their RI episodes are different with the RI process in ULJET being interrupted early, resulting in a TC that is still formidable but considerably weaker than its counterpart in CTRL. Averaging tangential winds and warm core temperature perturbations over vertical layers identified the main differences in axisymmetric vortex structure are located in the upper levels of the vortex from 12- to 16-km altitude (Fig. 3.13). The weakening tangential winds and warm core perturbation temperatures in the upper levels is concurrent with the cessation of RI in ULJET and divergence of intensity between CTRL and ULJET. The decline and effective cap on DHOV and intensity in ULJET show that in these simulated TCs, establishing a coherent vortex structure that extends into the highest levels of

the troposphere is an important feature in CTRL which allows the storm to continue RI and achieve extreme intensities of category 4 and greater. The difference in peak intensity is greater in P_{min} than maximum sustained wind, but pressure is known to be a greater predictor of damage than maximum winds in landfalling TCs (Klotzbach et al. 2020, 2022a). The strong P_{min} difference implies the TC in CTRL would present greater hazards than the one in ULJET.

The lack of upper-level winds and warming being most prominent from 14- to 16-km altitude lends credence to the importance of the UTLS warm core and cyclonic wind field present in modeled (Ohno 2015; Chen and Zhang 2013a) and observed (Duran and Molinari 2018) TCs of extreme intensity. Finocchio and Rios-Berrios (2021) exposed modeled TCs to increasing environmental VWS at different stages of intensification. The strongest TCs exposed to VWS near peak intensity resisted vortex tilt, but rapidly weakened to steady-state intensities similar to the steady-state P_{min} value attained by the TC in ULJET. The weakening of these strong simulated TCs may be due in part to VWS ventilation of the UTLS warm core. The upper-level weakening mechanism is similar to that proposed by Frank and Ritchie (2001) in which VWS results in loss of the warm core at upper-levels and rising P_{min} at the surface. The results, although idealized, suggest that TC intensity and intensification have a strong connection to processes which increase the vertical extent of the TC vortex. Intensification of the tangential wind field in the upper-levels is closely tied via thermal wind balance to the development of the upper-level warm core, evidenced by aircraft observations of RI (DesRosiers et al. 2022). The relationship between peak DHOV values and maximum steady-state intensity in the CM1 simulations can be considered with respect to potential intensity (PI) theory. Some derivations of PI theory rely on an estimation of the temperature of the TC outflow in the upper levels of the TC secondary circulation with a colder outflow temperature resulting in a higher calculated PI (Rousseau-Rizzi and Emanuel 2019). The azimuthally-averaged ULJET vortex structure decays at lower heights than CTRL (Fig. 3.12g,h) at steady-state intensity with a concentrated upper-level outflow jet which is maximized at lower altitude (not shown). In the troposphere, temperatures decrease with height so a lower outflow jet results in an increased outflow temperature, and therefore decreased PI. This agrees in principle

with Stern and Nolan (2011) who used a formulation of PI theory with varied SSTs and outflow temperatures to show the decay rate of the tangential wind field should be sensitive to the maximum PI of the TC. Increasing the vertical extent of the warm core should help to lower P_{min} through hydrostatic arguments, but the additional consideration of PI theory relates the height-intensity connection in TCs to the kinematics of the wind field via the height of the outflow in the secondary circulation. Although deciphering relationships between vortex height and intensity change requires more attention be paid to the upper levels of the atmosphere, the complex and interconnected nature of the TC implies processes in other region of the storm are likely to remain important.

Both modeling experiments indicate environmental VWS is an important modulator of TC vertical structure evaluated through the azimthally-averaged lens of DHOV. Different profiles of VWS correspond with different trajectories of DHOV during intensification. VWS, which is also present in the lower levels of the atmosphere in the WRF ensemble, resulted in long periods of vortex tilt and low DHOV values. During the active alignment phase, DHOV values quickly jump upward followed by a brief decrease and then continued growth during RI. In the CM1 simulations, the vortex remains aligned and DHOV continually increases from its starting value during RI at varied rates of increase. The lack of a noticeable jump and decline in DHOV in the CM1 simulations raises the question if this behavior is unique to alignment processes in sheared TCs. However, the experiments must be compared with some caution as there key differences between the simulation sets. Different choices in parameterization schemes mentioned in the methods are important, but a crucial difference from the WRF ensemble to the CM1 simulations is the inclusion of radiation. Radiation introduces cloud-radiation interactions which are shown to speed up TC development and are likely important to RI as well (Ruppert Jr et al. 2020). Upper-level TC structure is also sensitive to radiative tendencies (Trabing et al. 2019) which may partially explain the discrepancy between peak DHOV values in the WRF ensemble and CM1 control despite similar peak intensities. Vertical resolution differences could also play a role with 18 additional vertical levels and a model top altitude that is 5 km higher than the WRF ensembles in the CM1 simulations. The

model VWS profiles are also sustained with uniformity for long periods of time, which is unlikely to occur in the real atmosphere where VWS is found to vary at shorter timescales (Rios-Berrios and Torn 2017). The vertical structure of the tangential wind field examined in detail here is not independent from radial structure. Study of the radial structure of tangential winds in reconnaissance aircraft observations show a preference towards more compact inner cores and peaked wind profiles in the eyewall in intensifying storms (Martinez et al. 2017). Observational results in D23 indicated storms with more compact inner cores were more likely to possess large DHOV values. A principal component analysis indicates that although intensity, which is shown to relate to vertical structure here, and size can be somewhat decoupled, the empirical orthogonal functions explaining the bulk of the variance in TCs all depend on measures of the radial structure of the tangential wind, hinting the two are not independent (Casas et al. 2023).

3.6 Conclusions

As tropical cyclones (TCs) intensify, changes in the kinematic and thermodynamic structure of the middle, and especially upper, levels of the troposphere are associated with development of a deep axisymmetric vortex. The work here seeks to build on findings of DesRosiers et al. (2023), referred to as D23, in which all observed TCs possessed deep vertical vortex structure prior to RI. Vertical structure of the vortex wind field is evaluated with the dynamic height of the vortex (DHOV) metric, which is defined as the height at which the aimuthally-averaged tangential wind at the radius of maximum wind (RMW) decays to 40% of its maximum azimuthally-averaged value at 2-km altitude. Environmental vertical wind shear (VWS) can tilt vortices downshear and misalign the mid- and low-level centers, stunting the azimuthally-averaged projection of the tangential wind field. Revisiting the dataset of TCs observed with airborne radar utilized in D23 shows that all aligned TCs with minimal vortex tilt, regardless of their intensity at analysis time, exhibit DHOV values $\geq$ 10 km, indicative of the deep vertical vortex structure required for RI. All observed TCs with “short" DHOV values were tilted vortices with their vertical misalignment resulting in weak tangential winds in the middle and upper levels of the troposphere in the azimuthal-average

taken about the low-level circulation center. The absence of low DHOV values in all aligned TCs suggests that “short" TCs of tropical storm intensity or greater may not exist, and vertical alignment is all that is required for a TC to qualify as “tall", or adequately aligned, using DHOV. In aligned TCs, observed DHOV values trend upward with intensity indicating that continued vertical growth of the vortex is an important structural process in TC intensification.

Using DHOV, the evolution of vertical vortex structure in numerical modeling simulations is tracked to explore mechanisms correlated with changes to DHOV in the presence of moderate VWS. In the WRF ensemble simulations, a dramatic increase in DHOV is assigned as the alignment time as it is associated with existing rotation about the mid-level center approaching the low-level center, allowing for stronger tangential winds at greater heights when azimuthally-averaged about the low-level center. In the $\sim$ 20 hours following the alignment time, a jump in DHOV happens during continued reduction of vortex tilt, but the subsequent decrease in DHOV is associated with initial growth of a warm core perturbation temperature higher in the troposphere. RI onset occurs after the initial jump in DHOV at alignment time. RI onset is concurrent with the increase in upper-level warm core perturbation temperatures and happens prior to the complete reduction of vortex tilt to near-zero values. The timing suggests vortex alignment and RI onset are not discrete and simultaneous events, but rather part of a longer continuum which may be tracked relative to changes in the azimuthally-averaged tangential winds. Furthermore, “adequate" alignment of the low- and mid-level centers, signaled by sustained DHOV greater than 10 km, is found to be a necessary condition to RI and a key step in the TC alignment and intensification process in VWS. Continued DHOV growth during RI proceeds in concert with rapid strengthening of the upper-level warm core in the simulated TCs during the vertical growth stage, indicating the importance of upper-level processes to RI. Therefore, DHOV continuously provides useful information about TC structure and intensity change during the pre-alignment, active alignment, and vertical growth phases of intensification in VWS described here.

The sensitivity of the RI process to development of the upper level warm core is investigated in CM1 simulations in which a control (CTRL) TC is allowed to develop in quiescent flow while

another TC evolves in a parallel environment differentiated only by an upper-level jet (ULJET) of moderate VWS. Both simulations begin RI, but the process comes to a halt more quickly in ULJET resulting in a weaker steady-state intensity TC than that of CTRL with a lower peak DHOV value. Despite both TCs maintaining vertical alignment of the low- and mid-level centers, the upper-level jet prevents formation of a strong upper-level warm core and effectively serves as a cap for both DHOV and TC intensity. In the aligned RI of CTRL, the jump and decrease behavior of DHOV in the WRF ensemble TCs in moderate VWS is noticeably absent. Differences in the evolution may be indicative of different RI pathways with respect to vertical structure in dissimilar VWS environments, but several key differences in model configuration likely contribute as well. Calculation of azimuthally-averaged winds and perturbation temperatures in both experiments confirm that evolution in most lower and middle vertical levels of the TCs are similar and the biggest structural differences are present in the upper levels. The greatest differences in TC structure were between 12- 14-km altitude where CTRL developed a localized perturbation temperature maxima while the thermal structure of ULJET decayed rapidly with height. Differences at these altitudes as well as differences in peak steady-state intensity suggest the presence, or lack, of a component of the warm core at the interface between the upper-troposphere and lower-stratosphere (UTLS) may be important to extending the duration of RI and setting a ceiling for the peak steady-state intensity a TC can achieve. Vertical structure seems to be primarily related to the profile of environmental VWS. Although vortex tilt explains most of the reduction of DHOV in observed cases and the WRF ensemble, the CM1 results suggest that ventilation of the warm core by upper-level VWS may be capable of limiting the vertical extent of TCs regardless of alignment in the lower- and middle-levels of the troposphere.

Through the lens of potential intensity (PI) theory, the influence DHOV exerts on TC intensity is related to vortex height via its relationship with the vertical location of TC outflow and its temperature. Lower outflow temperatures in a taller TC create a greater temperature differential between the outflow layer and the surface, and therefore a stronger PI. Although changes in TC vertical structure are found to be a robust feature of intensification and RI in the modeled TCs,

it is important to note that vertical structure co-varies with radial structure and both exhibit relationships with TC intensity change. Upper-level structural changes in TCs are likely sensitive to choices made in horizontal and vertical resolution as well as radiation and other parameterization schemes (Duran and Molinari 2019). Sensitivity tests with these choices and their impacts on development of the upper level vortex would be a useful effort in future work. Successful ventilation of the UTLS warm core in ULJET motivates numerical modeling experiments to discern just how vulnerable this feature, which exists in a region of weak inertial stability, is to radial ventilation by varied magnitudes of upper-level VWS. The mechanisms by which the warm core in the upper levels of a TC intensify may differ from lower levels of the troposphere. Understanding these potential differences may help discern how the TC intensification process may differ throughout an RI event. Agreement of the DHOV analysis conducted here with the findings of several past studies of TC vertical structure and intensity change described in the discussion section confirm DHOV is a useful vertical structural metric for subsequent work on the topic. The results of this study also help to assign physical meaning to the observed relationship between DHOV and intensity change found in D23. Continued investigation of internal processes and environmental conditions which modulate vertical vortex structure and DHOV should improve our understanding of RI, providing the field with additional knowledge with which to improve TC intensity forecasts.

Chapter 4

Tropical Cyclone Surface Wind Reduction with a Neural Network

4.1 Introduction

The tropical cyclone (TC) surface wind field is of great interest as it relates to the magnitude of TC impacts and hazards. Operational forecasting centers such as the National Hurricane Center (NHC) in the United States of America as well as others globally are tasked with estimating and forecasting characteristics of the surface wind field. Accurate estimation of the maximum sustained 1-minute-average wind speed of the TC at 10-m altitude over open-ocean conditions (V_{max}) is a key metric for operational hurricane intensity classification by the NHC on the Saffir-Simpson Hurricane Wind Scale. Although wind alone is not a comprehensive metric for destructive potential of a TC (Klotzbach et al. 2022a), the importance of V_{max} to present operational procedures make its estimation an important task. At the NHC, surface winds are operationally reported in knots (kt; 1 kt = 0.51444 m s^{-1}). The radius of hurricane force winds (R64; 64 kt), damaging winds (R50; 50 kt), and tropical storm force winds (R34; 34 kt) are characterized in quadrants to define the spatial distribution of the TC surface wind field (Sampson and Knaff 2015). The most damaging winds are located at the radius of maximum winds (RMW), which is typically within the TC eyewall.

The surface wind maxima occurs within the turbulent planetary boundary layer (PBL). TC reconnaissance aircraft cannot safely operate in the PBL which makes in-situ measurements of surface V_{max} difficult to obtain. TC wind data is routinely available above the PBL via in-situ aircraft observations along the flight path and with much greater coverage when data from the tail Doppler radar (TDR) aboard NOAA P-3 Hurricane Hunter aircraft is used for dual-Doppler wind synthesis (Lorsolo et al. 2013). Although TDR-based wind analyses can provide excellent coverage of the wind field in TCs, they cannot produce reliable winds near the surface due to partial

filling of the radar beam by the surface at the lowest levels (DesRosiers and Bell 2024). Estimates of surface V_{max} can be obtained from flight-level aircraft observations of the PBL via reduction factors (RFs) which reduce observed flight-level winds in the free troposphere to the surface.

Franklin et al. (2003) empirically-derived RFs using wind profiles along the falling trajectories of global positioning system (GPS) dropwindsondes which are deployed from TC reconnaissance aircraft to take measurements between the aircraft and the surface. Dropwindsonde measurements are instantaneous and may record higher gusts, so an average of the lowest 150 m of observed winds (WL150) is reduced to the surface using the profiles to obtain an estimate of the 1-minute sustained V_{max}. The drift of dropwindsondes as they fall from aircraft to the surface makes the exact co-location of in-situ surface wind observations with flight-level wind observations impossible. The study found that in the convective eyewall of TCs, surface winds are $\sim$ 90% of their value at the 700 hPa pressure altitude ($\sim$ 3 km) where aircraft typically fly when observing TCs of hurricane strength or greater.

Despite observational limitations of dropwindsondes for generating accurate RFs, the RFs obtained from their profiles in Franklin et al. (2003) are still important to operational V_{max} estimation at the NHC. However, these RFs were intended for point measurements of wind, making them incapable of accounting for asymmetries in the full surface wind field of a TC. Asymmetries in the surface wind field of translating TCs are due largely to changes in the frictional surface drag around the storm which can be modulated by storm motion (Shapiro 1983). These motion-induced TC wind field asymmetries result in asymmetric RFs around the TC with lesser reduction of flight-level winds to the surface expected to the left of motion. This asymmetry in RFs is captured in a linear model constructed by Kepert (2001) which can reproduce observed characteristics of a localized maxima in the low-level winds termed the boundary layer jet. The linear model attributes the asymmetric jet to strong inward advection of angular momentum in the PBL resulting in supergradient flow, however the jet is found to be too weak in the linear model. A more advanced model which accounts for nonlinear effects as well as vertical advection produces a stronger boundary layer jet and asymmetry which is more consistent with observed behavior (Kepert and Wang

2001). Most of the motion-induced asymmetry in the flight-level and surface wind fields can be captured by the smoothed wavenumber (WN) 0+1 structure of the TC wind field (Uhlhorn et al. 2014).

There is variability beyond the larger-scale left-to-right asymmetry in RFs, especially in the highly variable TC inner core where the strongest winds are located. Import of angular momentum into the core of the storm by the inflow within the PBL is a critical component of TC intensification which helps to maintain and increase strong surface winds despite momentum lost to surface drag (Smith and Montgomery 2016). An inflow maximum, which is preferentially located in the front-right quadrant of a moving TC (Shapiro 1983), is likely an important player in the surface wind maxima typically being located here despite the weaker RFs right of motion. Radar observations confirm the convergence favored in the front right motion-relative quadrant is associated with convective initiation (Didlake Jr. and Kumjian 2018). The presence of convection indicates higher RFs in the original work of Franklin et al. (2003) so convective initiation in this quadrant should increase inner-core RFs. The outward slope of the tropical cyclone eyewall is also critical to inner-core RFs as the maximum surface winds are almost always located within the flight-level RMW where wind speeds aloft are decreasing along the flight track (Powell et al. 2009). The position of the surface wind maximum is also sensitive to the magnitude of storm motion and its resulting surface drag asymmetries which can move the surface RMW radially inward with increasing translation speed of a TC (Williams Jr. 2015). With these factors in mind, the motion of a TC and location within a motion-relative framework offer important contextual information to the task of wind reduction.

Past work has attempted to reduce wind observations to the surface while accounting for TC wind field asymmetries. The H*wind system developed at the National Oceanic and Atmospheric Administration Atantic Oceanographic and Meteorological Laboratory's Hurricane Research Division (HRD) can be used to incorporate surface wind estimates from the observations at various altitudes collected with a multitude of observational platforms to reconstruct a best guess of the TC surface wind field (Powell et al. 2010). Knaff and Slocum (2024) designed an automated technique

to reduce an observed flight-level wind field to the surface using an asymmetry-aware formulation of the Franklin et al. (2003) RFs employed operationally. Although this method is successful at producing bulk vortex surface wind field characteristics, estimates of V_{max} are often too low in this product, and its quality suffers when observational coverage is sparse. Kepert (2023) designed a parametric model which is capable of capturing impacts of increased surface roughness over land that increases frictional drag on the winds in the PBL. This method is an improvement in our understanding of frictional effects in the PBL but is targeted for model assimilation into surge and wave models versus intensity and wind radii estimation.

There are many existing and emerging observational technologies which can be leveraged to estimate the surface winds in TCs (Knaff et al. 2021). Among the most promising new technologies is Synthetic Aperture Radar (SAR), which can derive TC surface wind fields via satellite by taking advantage of different sensitivities between co- and cross-polarized signals (Mouche et al. 2017). A geophysical model function (GMF) is used to fit the signal to observed surface winds, but like many other fitting techniques, struggles to accurately depict the highest winds which are rarely observed compared to winds of lower magnitude. The Imaging Wind and Rain Airborne Profiler (IWRAP) is a downward-pointing, conically-scanning, dual-frequency, dual-polarization Doppler radar deployed on recent aircraft reconnaissance flights which is capable of retrieving winds in the PBL at high ($\sim$ 30 m) resolution (Holbach et al. 2023). Continued deployment of IWRAP in intense TCs will be instrumental to increasing the count of high-quality observations of high winds in the PBL of TCs. The Stepped Frequency Microwave Radiometer (SFMR) is a nadir-looking microwave radiometer mounted on reconnaissance aircraft to measure brightness temperatures (T_B) from the ocean surface, and atmosphere between the sensor and surface at six different C-band frequencies (Uhlhorn et al. 2007). Surface wind speeds and rain rates are retrieved from SFMR T_B with a GMF fit to observations of these quantities. No instrument used in operations matches the quantity of surface wind data available via the SFMR. However, dropwindsonde drift away from the flight path makes direct co-location of the surface and flight-level wind an issue that is only partially remedied by limiting the distance allowed between flight-level winds paired to surface

observations to train the GMF. Brightness temperatures recorded by the SFMR are sensitive to characteristics of the sea surface which changes in response to wind stress. The generation of sea foam from breaking waves is a major contributor to ocean surface emissivity sensed by the SFMR. Sea foam generation is sensitive to the wind stress and orientation of the swell with respect to the wind which changes around the TC (Holthuijsen et al. 2012) and causes spatial inconsistencies in the emissivity sensed by the SFMR.

The SFMR GMF is continually improving to address issues discovered by researchers and forecasters. Algorithm updates as well as characterization of its errors have helped improve surface wind retrievals with the SFMR. Attribution of emissivity sensed by the SFMR to rain in the atmospheric column along the sensor path and characteristics of the sea surface allows the GMF to predict both a rain rate and surface wind speed. Incorrect partitioning of the measured emissivity in the retrieval algorithm can result in a high predicted wind speed bias in heavy rainfall and in the peak winds which are typically present in heavy precipitation. Identification of these issues and re-formulation of the GMF by Klotz and Uhlhorn (2014) greatly improved this bias in the operational retrieval algorithm. Sapp et al. (2019) investigated the current SFMR retrieval algorithm and found several issues including a 10% low bias in predicted wind speeds below 45 m s^{-1}. Low precision remains below surface wind speeds of 15 m s^{-1} as well as the accurate prediction of low rain rates ($>$ 10 mm h^{-1}). The study proposed updates to the GMF which will help improve operational SFMR wind retrievals when implemented. The area in which V_{max} occurs is not always observed by the SFMR. An observing system simulation experiment for the SFMR quantified the undersampling of V_{max} in modeled TCs by comparing the maximum winds recorded by the SFMR to the maximum winds of the modeled TC around the time of a simulated reconnaissance flight (Klotz and Nolan 2019). The study found that in larger, weaker TCs of tropical storm intensity ($V_{max} < 65$ kt), the SFMR typically observed maximum winds that are less than V_{max} by 14% or more. As storms grow more organized and intense with compact inner cores, the underestimate is less pronounced with peak SFMR winds being lower than V_{max} in major hurricanes ($V_{max} \geq 96$

kt) by about 4% or less. Methods which estimate V_{max} from SFMR observations must take this undersampling into account.

NHC forecasters need real-time estimates of surface winds from more abundant flight-level observations that can help facilitate V_{max} estimation and define the footprint of hazardous winds at the surface. The current operational RFs do not adequately capture the asymmetries in the flight-level and surface winds which are critical to accurate surface wind reduction. Despite the imperfections of SFMR observations, this instrument provides copious retrieved surface wind values which are co-located with the flight-level wind measurements from reconnaissance aircraft. Co-located data can be leveraged to provide high-temporal-resolution estimates of observed ratios between surface and flight-level winds to inform accurate RFs in TCs. Previous work utilized SFMR observations to inform reduction factors which relate the maximum winds at flight-level to the surface V_{max} (Powell et al. 2009). Although prior work improves upon the more static reduction methodology of Franklin et al. (2003), the method is trained on past SFMR surface wind speed retrievals obtained with a less accurate GMF and is evaluated against the SFMR values and their inaccuracies. Future efforts, such as the one described herein, should validate an SFMR-trained model against the in-situ data obtained from dropwindsondes or other independent measurements.

Machine learning (ML) is gaining considerable traction for handling large data problems in atmospheric science (Boukabara et al. 2019). The abundance of SFMR data from reconnaissance flights makes a ML approach a promising avenue to reduce the inherent noise of the observations and harness potential relationships between flight-level and SFMR winds. Recent success in accurately reconstructing the 3-dimensional wind field structure of a TC using sparsely sampled data with a neural network (NN) demonstrates ML is a capable tool for this task (Eusbi et al. 2024). A data-informed ML wind reduction model can offer greater flexibility than the operational RFs. Analysis of the training data and validation of model predictions against in-situ measurements can shed light on weaknesses of the previous operational RFs. ML-model-derived surface wind fields can assist forecasters in determining characteristics of the TC wind field and storm intensity in real-time.

This study aims to train a neural network (NN) machine learning model to reduce winds recorded at higher altitudes in TCs to the surface. Section 4.2 discusses the data and methods. In section 4.3, the training dataset is analyzed, different predictive NN methodologies are compared, and performance of the chosen NN model is evaluated. Discussion of the results and overall conclusions are given in sections 4.4 and 4.5, respectively.

4.2 Data and Methods

4.2.1 Data Preparation

The FLIGHT+ dataset (Vigh et al. 2020) contains TC observations in a standardized format with flight level and SFMR data collected during TC reconnaissance flights. Earth-relative and storm-relative winds are available at high (1 s) temporal resolution. The data is quality controlled and parsed into radial legs flown in towards or out from the TC center. The most recent version of FLIGHT+ (v1.3) contains data from 1997 through 2019. Earth-relative flight-level wind data are used in favor of storm-relative wind so that the flight-level data can be appropriately compared to the earth-relative SFMR surface winds. The SFMR data in FLIGHT+ is reported as the wind speeds retrieved by the operational GMF at the time of a flight, so data collected prior to 2016 is omitted to ensure all surface wind data utilized in this study is retrieved from SFMR emissivity data using the most recent operational GMF (Klotz and Uhlhorn 2014). SFMR data quality control during compilation of the FLIGHT+ dataset excludes observations collected when aircraft motion or shallow water conditions below the aircraft would impact the ability of the instrument to accurately predict surface winds from the collected emissivity values. The 1-s temporal frequency of the wind data results in a large spread of wind ratios (WR; $\frac{SFMR}{Flight-level\ Wind}$) due to the gusty surface wind data within the PBL being far more noisy than the flight-level winds in the free troposphere. WRs are the physical basis for the RFs discussed in previous literature, so the two are considered synonymous going forward. Extreme WR values may be due to observational errors in addition to the noise and are not likely to be physically relevant to the relationships that a predictive methodology needs to learn to estimate surface winds. To remove extreme values, observations with WRs

greater than 0.6 or lesser than 1.4 are removed from the data before any subsequent preprocessing steps.

The SFMR and flight-level wind data are temporally smoothed to 10-s averages for all data points where a 10-s window surrounding the observations reports values for 6 of the 10 seconds in the window. Temporal autocorrelation is present in this time series data, but accepted as a necessary shortcoming of the training dataset to maintain a high volume of observations. SFMR surface wind speeds greater than 90 m s^{-1} are excluded and unlikely to be correct given the rarity of surface winds of this intensity and the struggles of the operational GMF in high winds (Klotz and Uhlhorn 2014; Sapp et al. 2019). To allow a ML method to predict winds in TCs across a spectra of size and motion characteristics, observations are mapped to a normalized polar coordinate system on a flight by flight basis with coordinates of θ* and r*. θ* is oriented by setting the TC motion direction to 0°. The TC motion direction is calculated using averages of the Cartesian zonal and meridional storm motion components gathered during a time period spanning the initial time of the first radial leg to the final time of the last radial leg of a flight. Flights with storm motion magnitudes greater than 20 m s^{-1} are considered anomalous and excluded from the dataset as outliers. Zonal and meridional distances of the aircraft from the storm center for each observation are used to solve for a 0°-north-relative θ value which can be rotated into the TC-motion-relative θ* coordinate. The RMW is calculated at aircraft flight level for each flight in the dataset by averaging the radial distances from the storm center at which flight-level winds reach a peak during each radial leg. RMW values greater than 100 km are indicative of storms with poorly-defined wind field structure, so any flights with RMWs in excess of this value are not included. To obtain the normalized radius coordinate, r*, the distance of an observation from the storm center is divided by the RMW determined for the flight.

To avoid data near the storm center where winds are likely to be weak as they decay rapidly inward of the RMW, data with r* values less than 0.5 are excluded. TC winds also decay with distance outward from the RMW, so an outer bound must be set to ensure the training data is likely to be within the TC environment. Given the need to forecast radius values at quadrant

resolution for R34 (Sampson and Knaff 2015), this radial bound must not be set so strictly that a wind reduction method trained on the data would not have the capability to determine radii, should that functionality be desired by forecasters. To choose an appropriate outer bound for r*, the density of SFMR surface wind observations is plotted in hexbins (Figure 4.1). The motion-relative quadrants are the front left (FL; $270^\circ \leq \theta^* < 360^\circ$), front right (FR; $0^\circ \leq \theta^* < 90^\circ$), rear right (RR; $90^\circ \leq \theta^* < 180^\circ$), and rear left (RL; $180^\circ \leq \theta^* < 270^\circ$). The majority of SFMR winds of 34 kt ($\sim$ 17.5 m s^{-1}) or greater lie within r* of 5 (gray dashed line; Figure 4.1) so observations outside of 5 r* are excluded from the dataset.

Weak winds where SFMR sensitivity to surface emission is poor (Sapp et al. 2019) must be limited so data with flight-level wind speeds below 15 m s^{-1} are omitted. This condition, paired with the lower data inclusion bound of 0.6 for observed WR effectively excludes any SFMR surface wind value below 9 m s^{-1}. The radial structure of the wind field varies with TC intensity. Wind peaks become more pronounced with more extreme gradients near the RMW in flight-level winds as a storm becomes more intense (Martinez et al. 2017). Therefore, TC intensity contains useful information with which to infer structure of the TC wind field. Historical TC intensity data is available at 6-hourly synoptic times in the HURDAT2 dataset (Landsea and Franklin 2013b) for storms in the North Atlantic and Northeast and North Central Pacific basins, where TC reconnaissance missions most often take place. During each flight in the dataset, the TC intensity (reported in kt) for the closest previous synoptic time is assigned to all observations collected during the flight. By using the previous intensity estimate, this predictor only provides data which would be available in a real-time application of surface wind prediction. Typical operational TC reconnaissance flight levels are the 850 hPa pressure altitude ($\sim$ 1500 m) in storms of tropical storm strength or less ($V_{max} < 64$ kt) and the 700 hPa pressure altitude ($\sim$ 3000 m) in storms of hurricane strength or greater ($V_{max} \geq 64$ kt) (Knaff et al. 2021). Observations with flight-level pressure values outside of $\pm$ 25 hPa of 850 or 700 hPa are removed from the dataset to ensure the data only consists of observations relevant to routine TC reconnaissance. A majority of the observations in the dataset

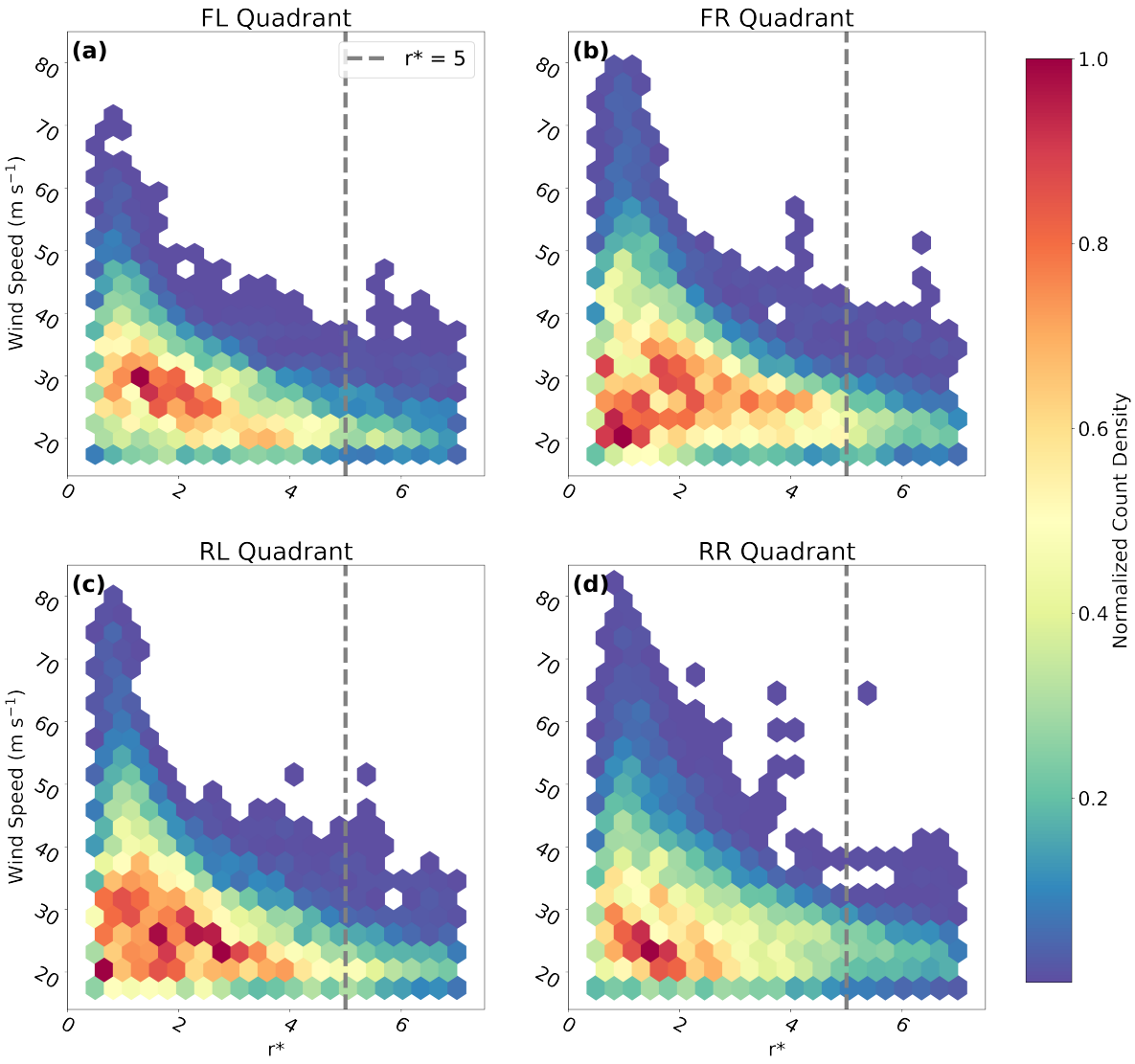

Figure 4.1: Hexbin plot showing the normalized count density (colorbar) for observations in the FLIGHT+ dataset divided into storm-motion relative quadrants. Quadrants are the front left (FL; a), (b) front right (FR; b), rear left (RL; c), and rear right (RR; d). A gray dashed line marks the location of the RMW-normalized radius (r*) of 5. 20 uniform bin width increments in r* and wind speed from 400 possible bins. Absence of hexbin tiles indicate no observations are present in a bin corresponding to its coordinate pair.

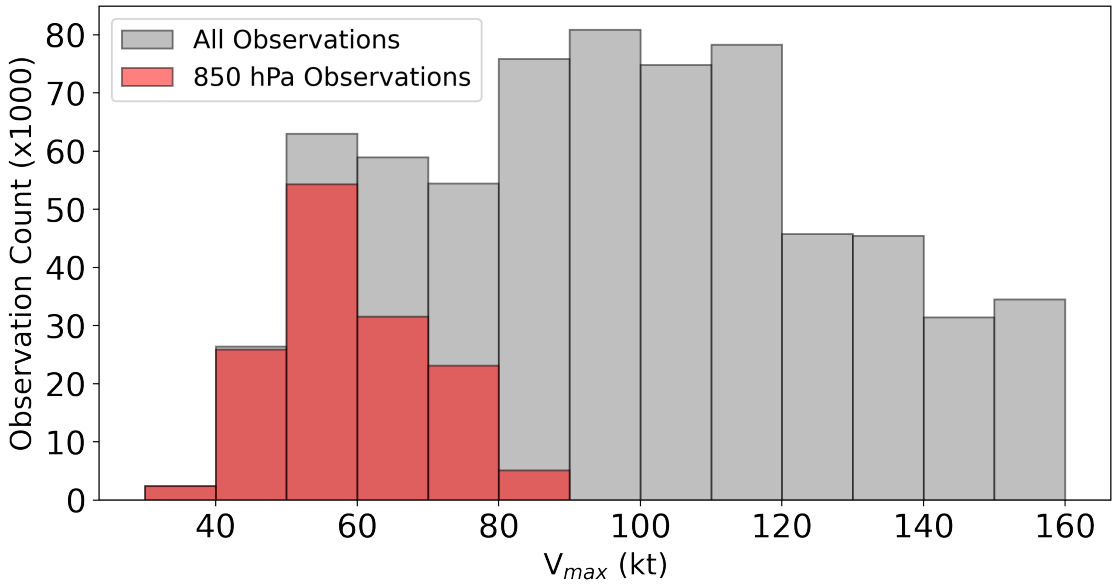

Figure 4.2: Histogram of counts of most recent prior best track TC intensity (V_{max}) in bin increments of 10 knots for all observations (gray) and observations taken near the 850 hPa flight level (red).

are recorded near the 700 hPa pressure altitude with only $\sim 21\%$ of observations collected near 850 hPa (Figure 4.2).

4.2.2 The Simplified Franklin Wind Reduction Method

The WRs derived from dropwindsonde profiles by Franklin et al. (2003) are still key to NHC operations. Forecasters can use these fixed recommended WRs to reduce flight-level wind observations to the surface. Some internal additions to the method at the NHC allow forecasters to account, in a limited capacity, for motion-induced asymmetries (Wallace Hogsett; Personal Communication, 2023). The published method provides WRs which are differentiated by inner core (r* $<$ 2) or outer core (r* $\geq$ 2), the presence of convection, and the pressure level at which an observation is taken. A Simplified Franklin (SF) wind reduction methodology is developed based on the guidance in the published work to serve as a baseline for comparison of new methods evaluated in this study. Given the challenge of systematically determining the presence of convection, the SF method always uses the WRs recommended for convection which only deviate for non-convective scenarios in the outer vortex. The method takes the fixed recommended WR values

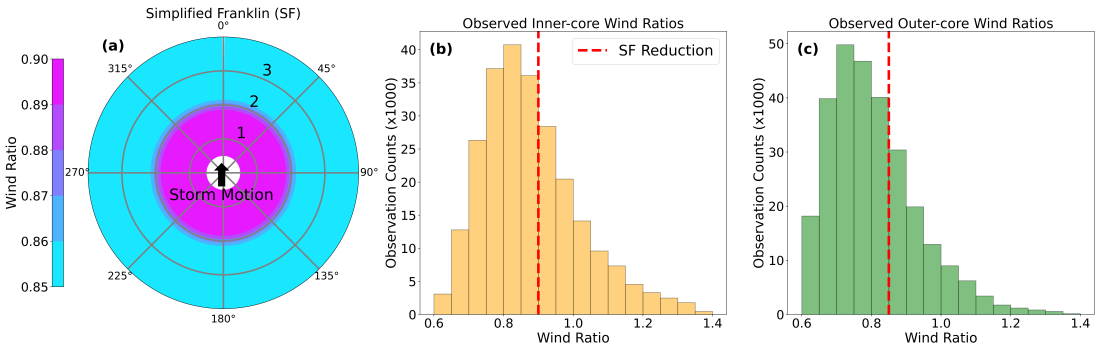

Figure 4.3: (a) Wind ratios recommended at the 700 hPa flight level by the SF wind reduction scheme. Histogram of all post-smoothing observed wind ratio (WR = $\frac{SFMR}{Flight-level\ Wind}$) values in the dataset with bin increments of 0.5 (b) within the TC inner core (r* $<$ 2) and (c) outer core (2 $\leq$ r* $\leq$ 5) with the recommended SF WR (red dashed line) shown in each.

and linearly interpolates between them from 1.75 to 2.25 r* for inner- versus outer-core considerations and between pressure levels. The recommended SF WR field at the 700 hPa pressure level is depicted spatially in the normalized polar coordinate space defined by r* and θ* in Figure 4.3a. The recommended reduction field is notably symmetric, offering new methods an opportunity for improvement relative to SF by accounting for TC wind field asymmetries. Histograms of observed WRs near the 700 hPa pressure level within the TC inner core and TC outer core (Figure 4.3b,c) show considerable spread about the static WR values of 0.9 and 0.85 recommended by the SF method in their respective regions at this level.

4.2.3 Machine Learning

Dataset Division

When training ML models, it is important to set aside data for subsequent model evaluation. Evaluating the model on unseen data excluded from the training set helps verify the model can generalize well and still achieve satisfactory performance scores on data that was not presented during training. To avoid spatial and temporal autocorrelation issues between the withheld sets and the training set as well as separate instances of structural features unique to a TC, data from all flights into a single TC throughout its lifetime are kept together in whichever set they are assigned. The division of data observations is shown as a scatter plot of the SFMR values with respect to the

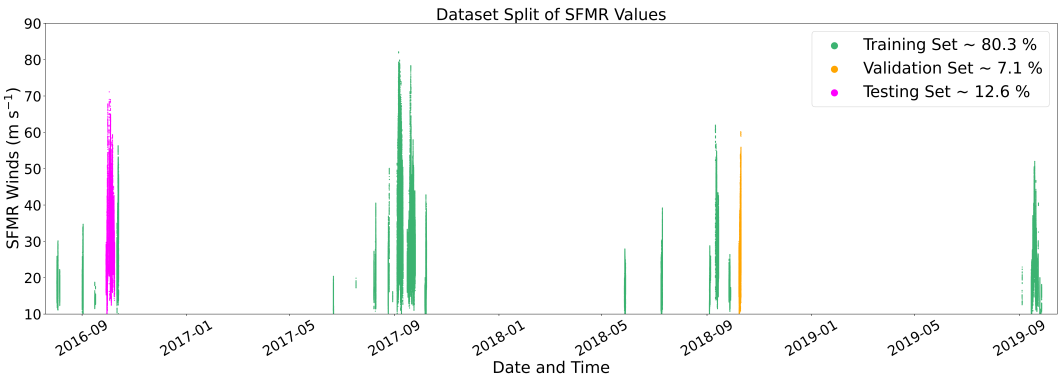

Figure 4.4: Observed SFMR values in the Flight+ dataset with colors (legend) indicating the data allocated to the training (green), validation (orange), and testing (magenta) sets. Percentages of the total dataset contained in each set are provided in the legend.

times at which there were collected (Figure 4.4). The validation set (orange) is composed of all observations collected in Hurricane Michael (2018) which was sampled by aircraft at a range of intensities from tropical storm to major hurricane (Beven et al. 2019). The testing set (magenta) consists of observations from Hurricane Matthew (2016), which was also sampled over a wide range of intensities (Stewart 2017). The training set (green) is made up of all other storms in the dataset. A notable absence from the dataset is Hurricane Dorian (2019) which would provide additional observations of extreme winds. Data from this storm was excluded due to evidence that the SFMR wind retrievals in this storm were problematic and inaccurate at high wind values (Holbach 2022). Each of these datasets contain numerous observations of major hurricane force surface winds well in excess of 50 m s^{-1}. Across the three datasets, there are 672,444 samples from model training and evaluation.

Neural Networks

An artificial neural network (NN) ML model (LeCun et al. 2015) is utilized to predict the surface wind field from flight-level features. The NN is a multi-layer perceptron consisting of an input layer which is the size of the given features, a single-node output layer for the desired predictand, and hidden layers which can vary in both number of layers and number of nodes per layer. The feed-forward network fully connects all nodes in the prior layer to the next layer moving

information from the inputs, to the hidden layer(s), and finally the output. The nodes in each layer are assigned activation functions which are applied to the incoming numerical information before being passed on to the next layer. Two safeguards are in place within the NN to prevent overfitting to the training dataset. A ridge regression (L2) coefficient is set in the hidden layers and the dropout technique is also applied to randomly drop nodes at a specified rate from the neural network during training (Srivastava et al. 2014). Unless otherwise noted, different techniques tested in this study use a NN architecture defined by two hidden layers with counts of 30 and 10 nodes respectively. Default hyperparameter choices for the tested methods are 50 epochs, a batch size of 256, L2 regularization coefficient of 0.01, a dropout rate of 0.2, rectified linear unit (ReLu) activation functions, and a conservative learning rate of $1\text{x}10^{-4}$.

The loss function is an important determinant in how a NN learns. A common choice is tasking the model with minimizing the mean squared error (MSE) between the predicted and true values of the training set. Standard loss functions, like MSE, do not always meet the needs of the unique data problems that can be encountered in atmospheric science. In special cases, creation of a custom loss function to ensure the model learns in a manner consistent with its desired performance is necessary (Ebert-Uphoff et al. 2021). The challenge presented by surface wind data in TCs is the rarity of extreme wind observations compared to those of lower magnitude, evidenced by a histogram of the SFMR surface wind speed magnitudes in the training dataset (Figure 4.5). Common loss functions like MSE are agnostic to the magnitude of the value the model is trying to predict and would allow the NN to divert focus away from this sparsely populated wind regime, which is important to the determination of V_{max} in extreme TCs. To address this, a multiplier for common loss functions, MSE in this use case, is developed to increase the penalty for inaccurate predictions of high surface winds in the dataset. The shifted cubic loss function (SCL) utilizes the exponential growth of a cubic function:

$$Shifted\ Cubic\ Loss = MSE\ x\ ((SFMR - Shift)^3 + Shift^3) \tag{4.1}$$

The SFMR wind speed value in m s^{-1} is subtracted from a shift value and cubed. The cubed shift value is added to this quantity and the full value is multiplied by the MSE for each observation. The SFMR value makes the multiplier grow exponentially at high winds. The shift value, in this case set to the minimum tropical storm force wind value of 17.5 m s^{-1}, delays exponential growth by shifting the inflection point between positive and negative decay away from zero and extends the relatively flat portion of the function through the commonly observed wind speed regime (Figure 4.5; black line). Adding the cubed shift value again in the multiplier shifts the inflection point upward from zero on the y-axis and ensures the multiplier stays positive even when SFMR values are less than the assigned shift value. The function essentially counters the exponential decrease of observations at high winds with an exponential increase of loss penalty value in this region. Both the standard MSE loss function and SCL function are utilized to ensure the custom function produces the desired effect.

The NN is given a set of predictors, or features, with which to produce either the observed SFMR surface wind speed or WR. The location of the aircraft is provided in r* and θ* coordinates with both the sine and cosine of θ* provided to prevent a jump discontinuity in predictions as θ* changes from high values to 0° at the azimuth of storm motion. The location information is necessary to capturing the motion-induced asymmetry. The flight-level wind and altitude of the aircraft are provided to inform the model of the value to be reduced and the height from which to reduce it. The magnitude of the storm motion is given which controls the magnitude of the motion-induced asymmetry (Shapiro 1983; Kepert 2001) and WRs (Powell et al. 2009). The intensity of the TC assessed at the prior synoptic time is also provided which relates to improved structure and symmetry of the TC wind field as intensity increases. All input features are standardized using the mean and standard deviation of the values in the training dataset which is required for satisfactory NN performance. The predictands, either SFMR wind speed or WR, are not standardized nor required to be.

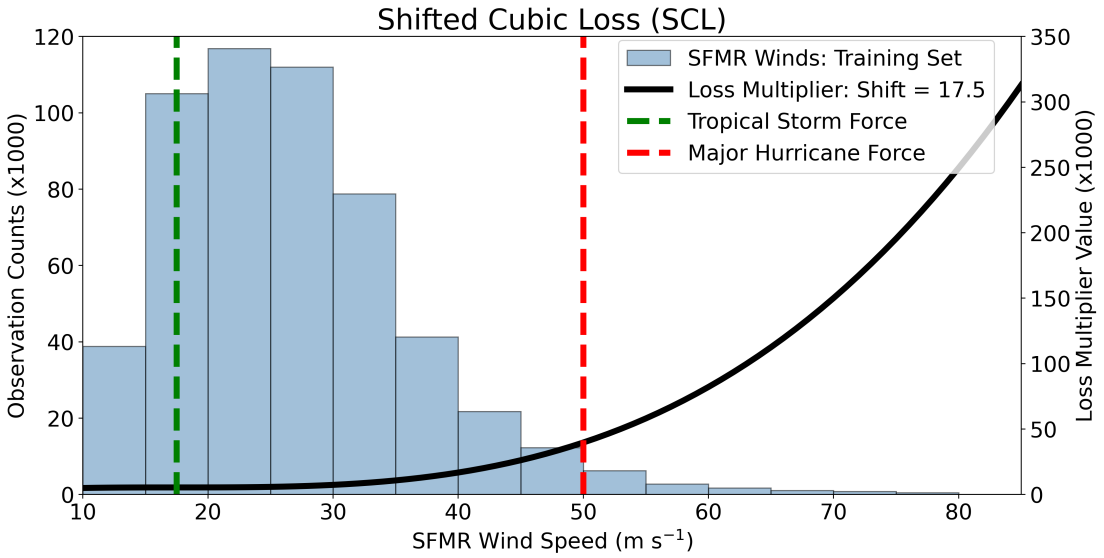

Figure 4.5: Histogram of observed SFMR wind speeds in the training set in m s^{-1} increment bins. Multiplier values for traditional loss functions from shifted cubic loss (SCL; black line) in relation to the SFMR wind speed of an observation with tropical storm force (green dashed line; $\sim$ 17.5 m s^{-1}) and major hurricane force (red dashed line; $\sim$ 50 m s^{-1}). The shift constant in the SCL function (Eq. 1) is set to 17.5 m s^{-1}.

Model Validation with Dropwindsondes

A prediction methodology trained with SFMR data which has known deficiencies in extreme conditions must be externally validated with more certain measures of surface wind. Data from past TC aircraft reconnaissance missions allows for this. The Tropical Cyclone Radar Archive of Doppler Analysis with Re-centering (TC-RADAR; v3j) is a historical dataset of kinematic analyses produced via dual-Doppler wind synthesis of TCs observed with TDR between 1997 and 2021 (Fischer et al. 2022). Flight-level wind fields for storms of tropical storm strength (altitude = 1.5 km) and hurricane or greater strength (altitude = 3 km) are transformed to the normalized polar grid space for prediction of a surface wind field by the ML method. The wind fields are smoothed to WN 0 + 1, which was deemed adequate for capturing storm-scale wind asymmetries by Uhlhorn et al. (2014). The smoothing is carried out at each radii where 25% of the azimuths report wind data based on recommendations for allowable gap size laid out by Lorsolo and Aksoy (2012). Surface wind predictions can be validated with in-situ measurements from dropwindsondes. A sustained surface wind is estimated from dropwindsonde vertical profiles by reducing an

average of wind speeds calculated over the lowest 150 m of the vertical profile (WL150) to the surface consistent with the methodology described in Franklin et al. (2003). The Tropical Cyclone Dropsonde Research and Operations Product Suite dataset (TC-Drops; v1.2) contains a large collection of dropwindsonde profiles collected from 1996 to 2021 (Zawislak et al. 2018). Surface wind observations derived from WL150 values calculated with TC-DROPS are also mapped to the normalized polar grid space using storm motion and RMW information from FLIGHT+. Comparison of surface wind predictions from TDR-derived wind fields at flight level with co-located dropwindsonde observations within the normalized polar grid enables $\sim$ 1000 points for validation of predictions against ground truth in-situ measurements.

4.3 Results

4.3.1 Observed Wind Ratios in FLIGHT+

The NN model learns from, among other variables, the flight-level and SFMR surface wind speeds in the FLIGHT+ dataset. Dividing the smoothed SFMR values by their corresponding flight-level winds creates a large sample of observed wind ratios which are the physical basis for reduction factors developed to reduce flight-level winds to the surface. Investigating the radial distribution of WRs in storm-motion-relative quadrants is helpful in characterizing the asymmetries the model is expected to learn from the observations and reproduce. Hexbin plots are utilized to show the density of observations in the dataset within bins defined by WR and r* for each quadrant. The hexbins are made up of a 15 by 15 array of equally-spaced bins in r* values (0.5 to 5) and WR values (0.6 to 1.4) which makes for a total of 225 possible hex tiles in the plots. The density count in the analysis is normalized from 0 to 1 where 1 corresponds to the maximum count density value in each quadrant. The normalization of the color scale by the maximum value in each quadrant allows a common color scale to show the variance of distributions in each. When no values populate a hexbin, it is not plotted. The RMW (orange dashed lines) and recommended WR values from the SF method (black lines) are displayed in the plots to provide context to the observation in terms of both the TC structure and current reduction methodology. Observations from flights into

TCs of tropical storm intensity near the 850 hPa pressure altitude are analyzed in Figure 4.6. The greatest density of observations is located within 2 r*. In weaker storms, the RMW is typically larger (Fischer et al. 2022) making for a greater physical distance spanned per unit of r*, which contributes to a greater density of observations at lower r* values. WR values are well distributed about the recommended WR line provided by the SF method with more systematic decreases of the WR values as r* increases to the right of motion, likely indicating more organized structure of the wind field in the right-of-motion quadrants.

In storms of hurricane strength (category 1 and 2) observed by aircraft flying near the 700 hPa pressure altitude (Figure 4.7), there is a more defined slope of WR and r* near the RMW. The relationship is stronger than the tropical storm cases in the FL quadrant indicating better organization of the TC wind field in this quadrant compared to storms of tropical storm intensity which are observed at lower altitudes. The increasingly symmetric wind field is consistent with behavior in observed TCs as they grow more intense (DesRosiers et al. 2022). Near the RMW at r* of 1, wind ratios are typically lesser than the WRs recommended by the SF method. The spread of WRs remains quite large in all quadrants. A greater density of observations at larger r* values is due to both larger storms and a RMW that is typically smaller, shrinking the physical distance spanned by r* values.

In storms of major hurricane intensity observed by aircraft near the 700 hPa flight level (Figure 4.8), the relationship between WR and r* is more defined in all quadrants. The normalized density of observations has increased markedly at larger r* values which is likely due to both smaller RMW values and more intense storms tending to be larger. The bulk of RMW contraction typically takes place prior to TCs reaching major hurricane intensity (Stern et al. 2015), so the shrinking of physical space spanned by r* coordinates between Figure 4.7 and Figure 4.8 should be minimal. The greater normalized density in outer-core observations is likely due to outward expansion of the wind field. The greatest density of observed wind ratios are typically below the recommended WRs by the SF method throughout most of the storm. This is not particularly surprising given the SF method is intended for point reductions, and our method assumes the presence

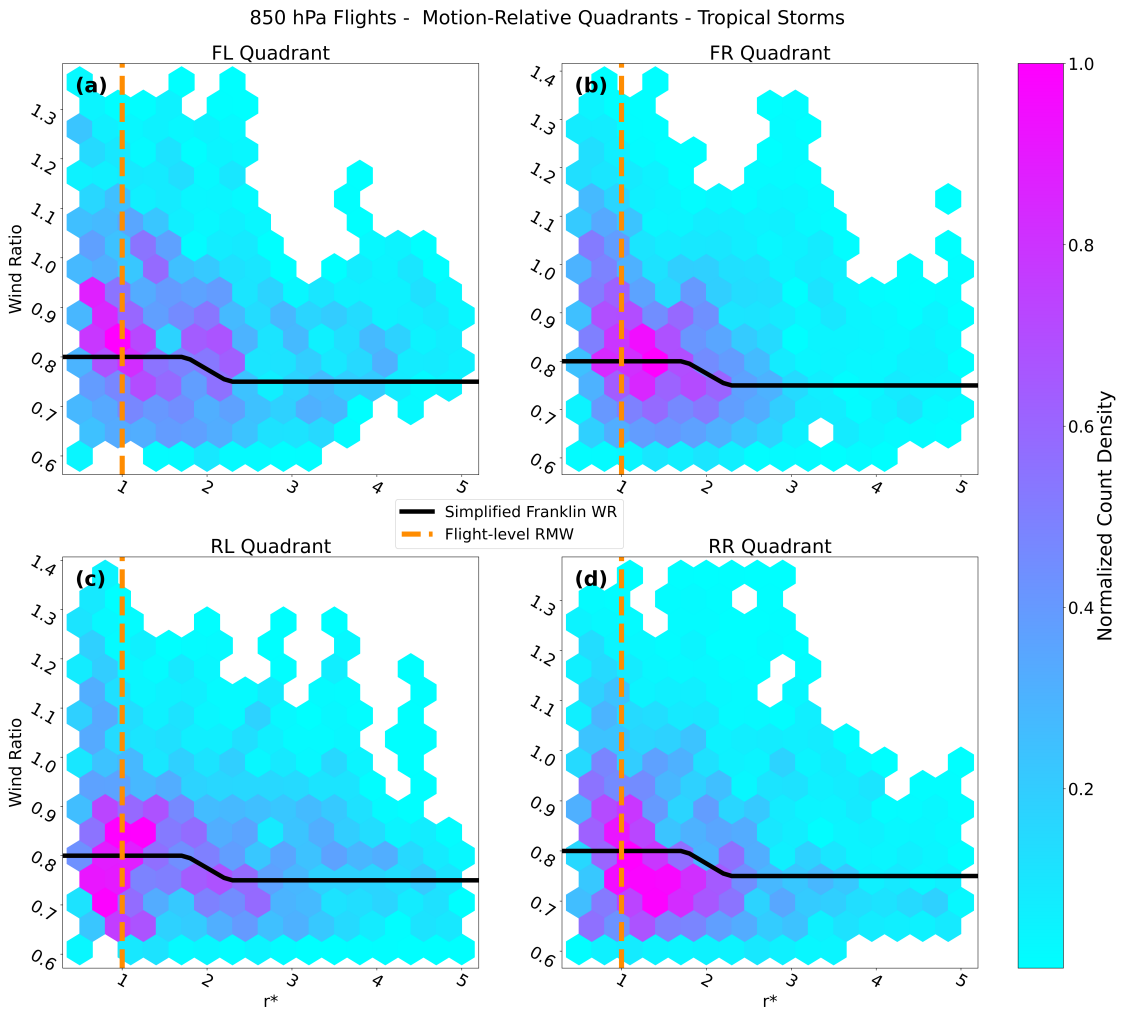

Figure 4.6: Hexbin plots with normalized density of observations in bins defined by coordinate pairs of wind ratio ($\frac{SFMR}{flight-level\ wind}$) and radial r* locations for flights in tropical storms ($V_{max} < 64$ kt) at the 850 hPa pressure altitude. Observation densities are given in storm-motion-relative quadrants of front left (a; FL), front right (b; FR), rear left (c; RL), and rear right (d; RR). The recommended SF reduction (black line) and flight-level RMW (orange dashed line) are shown. An absence of hexbin tiles indicate no observations are present in a bin corresponding to its coordinate pair.

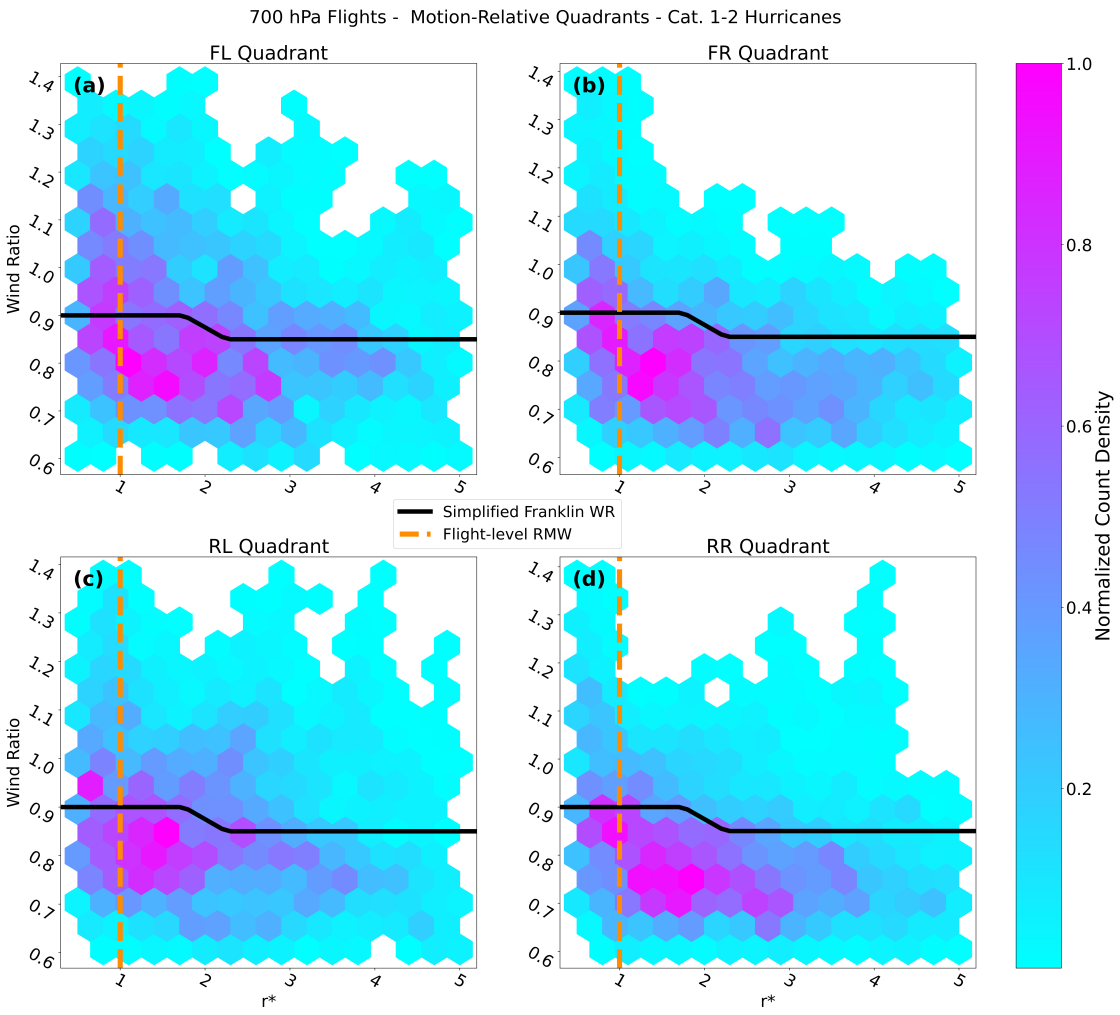

Figure 4.7: Same as Figure 6 but for 700 hPa pressure altitude flights into storms of Category 1-2 hurricane intensity (64 kt $\leq$ V$_{max}$ $<$ 96 kt).

of convection which is not a constant throughout the TC environment. The SF recommendation is a decent one for the bulk of observations near the flight-level RMW. However, within the RMW, the SF recommendation is too low as the WR values increase quickly while r* decreases. The rising WRs within the RMW are caused by the outward slope of the TC eyewall with height (Hazelton and Hart 2013). Due to this slope, the aircraft is likely to exit the eyewall and no longer observe strong winds at flight level while the SFMR continues to observe an ocean surface stressed by the strong winds within the eyewall. This behavior is also noted in Powell et al. (2009) where the SFMR surface wind maximum was almost always located inward of the flight-level RMW. An increase in occurrence of higher WRs in the outer core may be related to the presence of cross-swell in the far field of TCs which impacts the surface emissivity sensed by the SFMR (Holthuijsen et al. 2012).

Analysis of the FLIGHT+ dataset informs several factors which the NN model will attempt to capture when reducing flight-level winds to the surface. The SF model gives a first-order symmetric framework with which to estimate surface V_{max} from the flight-level winds, but other intensity and location parameters presented in the analysis here are important to capturing the asymmetric and changing nature of WRs in the TC environment. The motion-relative asymmetry in WRs suggests the WRs around the TC are sensitive to the present intensity of the system being observed as the wind field becomes stronger and more symmetric. An apparent increase in mean WR near and inward of the RMW should be accounted for with increasing WRs in this region to accurately place a surface wind maximum inward of the flight-level RMW. Overall, the observations paint a chaotic picture of WRs in observed TCs with significant spread that limits the potential accuracy of more static WRs, such as those recommended by the SF method. The noise in the data motivates the use of a complex and data-informed NN for wind reduction which can learn and account for relationships present in the observations.

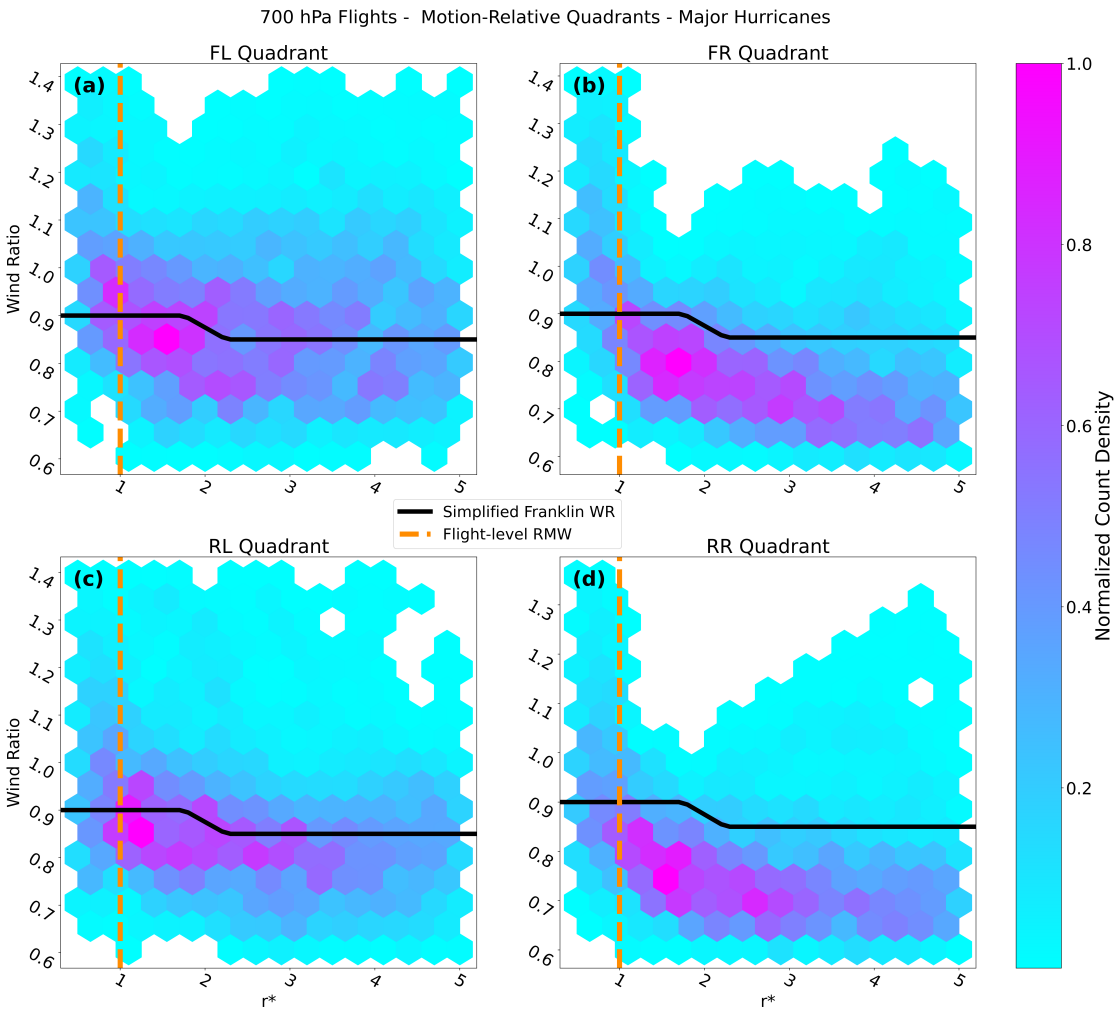

Figure 4.8: Same as Figure 6 but for 700 hPa pressure altitude flights into storms of major hurricane intensity ($V_{max} \geq 96$ kt).

4.3.2 Neural Network Method Comparison

Several different combinations of loss functions and predictands are evaluated to identify the NN method best suited for wind reduction. The nomenclature for each NN version is the loss function used in training followed by the predictand the model produces as its output. For example, a model referred to as MSE WR minimizes the mean squared error loss function in training and outputs a prediction for the WR to be used to relate the flight-level wind to the surface wind for the observation. In the case of a model prediction of WR, the NN is validating its prediction against the corresponding observed WR value. For a predictive technique, the predicted WR is used in the same manner as a WR would be, so the two are considered to be equivalent in this application. The different configurations use one of two loss functions; the MSE loss function and the SCL custom loss, which is multiplied by the MSE obtained from the model-predicted value and its target truth value in the dataset. The SCL multiplier increases the importance of accurate predictions in strong winds. The different possible predictands are the SFMR wind speed, the WR, and the residual error between an observed SFMR wind value and what the SF method would have guessed. A key for model nomenclature is given in Table 4.1. Note that for the error model, the predictand can be positive or negative. For the error NN (MSE ERR), the ReLu activation function, which limits output to positive values, is swapped for a hyperbolic tangent function which allows the NN to produce negative output. The true error values in the dataset are also scaled between -1 and 1 based on the minimum and maximum values found in the training set. The same scaler is applied to output from the NN to revert the unitless scaled errors back to values in m s^{-1}.

Table 4.1: Key for the neural networks nomenclature.

Model Name	Loss Function	Predictand
MSE ERR	Mean Squared Error	Error (SFMR - SF Prediction)
MSE WR	Mean Square Error	Wind Ratio
MSE SFMR	Mean Squared Error	SFMR Surface Wind
SCL SFMR	Shifted Cubic Loss with MSE	SFMR Surface Wind
SCL WR	Shifted Cubic Loss with MSE	Wind Ratio

Performance of each method is evaluated with the testing set by comparing the true SFMR values to the SFMR wind speeds predicted by the NNs (Figure 4.9). For models predicting the WR, the predicted value is multiplied by the flight-level wind speed to obtain a predicted SFMR surface wind speed. Error predictions are added to the surface wind speed predicted by the SF method to obtain a predicted SFMR wind. Converting all predictions to a common target value allows for a more direct comparison of model accuracy. Originally, the MSE ERR, MSE WR, MSE SFMR, and SCL SFMR methods were all tested using the default NN settings described in the Data and Methods section. The models generated by all methods with the exception of MSE ERR achieved both linear correlations, via r^2, and root mean squared error (RMSE) values, which outperform the SF method (Figure 4.9). The MSE ERR method likely needs additional dedicated tuning effort due to its differences from the others, but this was not pursued further in favor of continuing with more promising techniques. Among the top models, certain tradeoffs are apparent in their performance. The MSE SFMR method was consistently biased low in the rarely observed major hurricane force (SFMR wind $\geq$ 50 m s^{-1}) wind regime. The MSE WR method exhibited decreased low bias at high winds compared to MSE SFMR with similar performance metrics, but still struggled to predict high winds. The SCL SFMR model which applies stronger weighting to high wind observations in the loss function is able to more accurately predict high SFMR surface winds, but in a manner which is too exact. The GMF for the SFMR struggles at high winds, and the accuracy of those retrievals is uncertain.

The ideal wind reduction model trained on observations should make skillful predictions of SFMR surface winds while limiting the variance in WR. For models which output non-WR quantities, a predicted WR can be obtained by dividing the predicted surface wind by the corresponding wind at flight level. A model that varies greatly in WR would not be desired by forecasters as large variance is likely evidence of a model which recreates the noise and biases of SFMR observations and departs from the smooth WR field predicted by theory (Kepert 2001). Among MSE WR, MSE SFMR, and SCL SFMR, which are the three most skillful models of the original five tested, the RMSE values for predicted SFMR winds are comparable in winds of tropical storm and hurricane

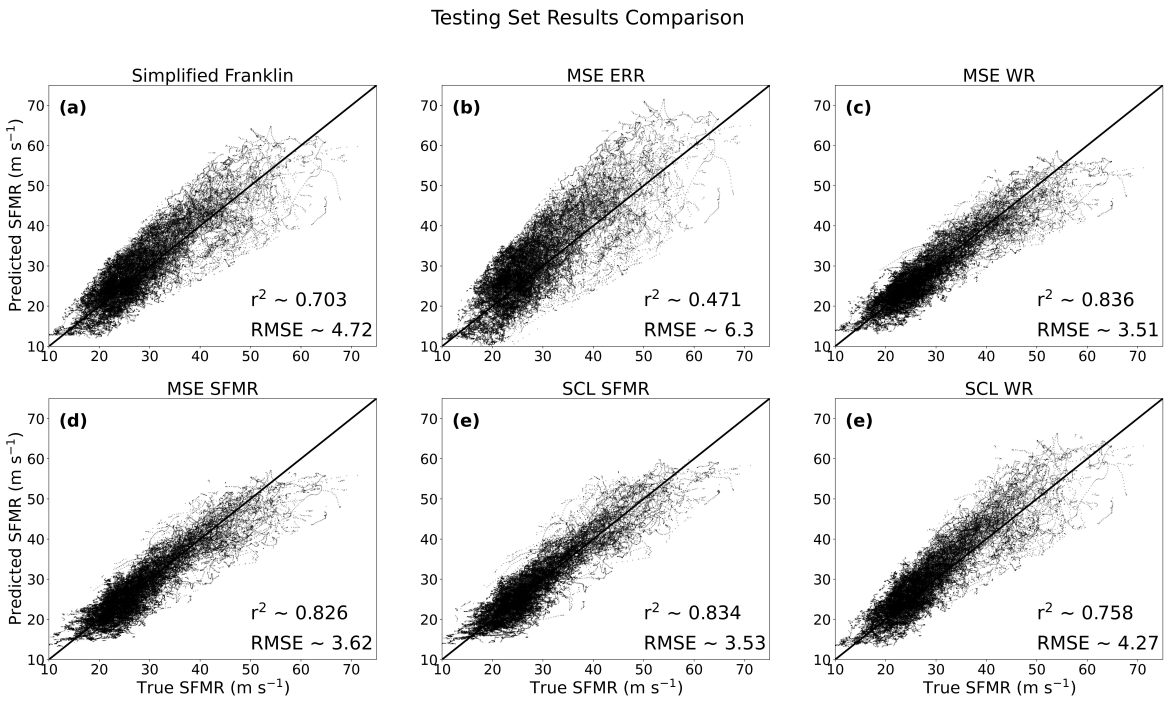

Figure 4.9: Predicted versus observed SFMR wind speeds with linear correlation (r^2) and root mean squared error (RMSE) values from the testing set given for the (a) SF, (b) MSE ERR, (c) MSE WR, (d) MSE SFMR, (e) SCL SFMR, and (f) SCL WR prediction techniques.

force in the testing set (Figure 4.10a). At major hurricane force, the SCL SFMR model exhibits the lowest RMSE which demonstrates the effect of weighting the loss function by high SFMR values. However, when taking variance of predicted WRs in tropical storm, hurricane, and major hurricane force wind speed bins in the testing set, this metric is maximized in all bins by the SCL SFMR model, which indicates the model may be learning noise and biases from the SFMR instrument (Figure 4.10b). Conversely, the MSE WR model exhibits the lowest variance in all bins among the three. However, the model's hesitance to predict high winds would make predictions of surface V_{max} in strong TCs too weak.

To capitalize on the low RMSE of the SCL SFMR method and the low variance of the MSE WR model, the methods are effectively combined into a new method referred to as SCL WR. The SCL WR method outputs a predicted WR but is trained using SCL custom loss. The SCL formulation (Eq. 1) for this model solves for MSE with true versus predicted WR values and multiplies the error by SCL which is still scaled by the SFMR value. Promising initial tests (not shown) of this

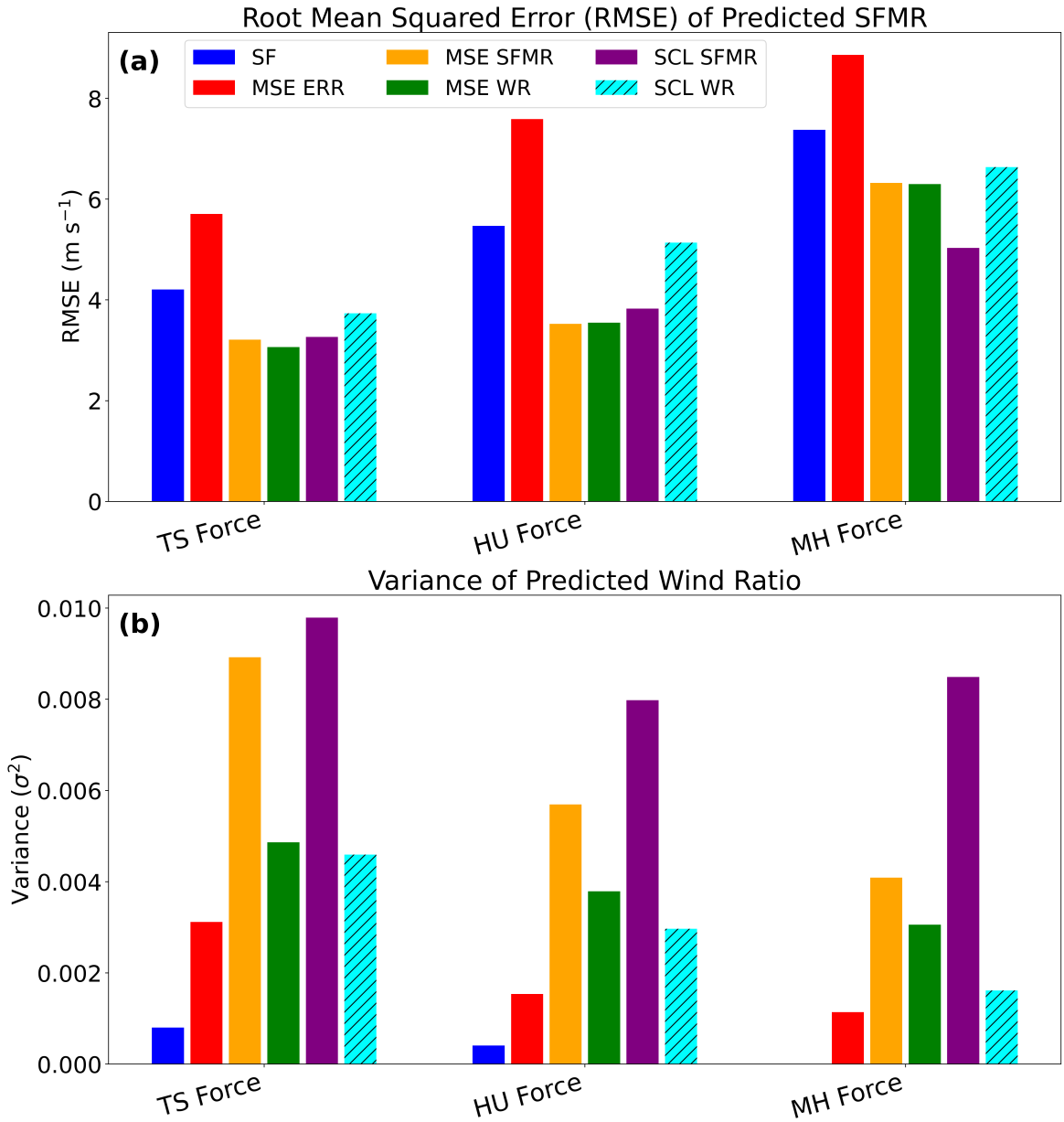

Figure 4.10: (a) Root mean squared error (RMSE) of predicted SFMR wind speeds versus observed for each technique (legend) and (b) variance (σ^2) of the predicted WRs for each technique at SFMR wind speeds of tropical storm (TS), Cat. 1-2 hurricane (HU), and major hurricane (MH) force in the testing set.

new NN training method prompted a more committed tuning effort to maximize performance. Hyperparameter tuning is performed with the KerasTuner package in Python (O'Malley et al. 2019). The number of hidden layers, number of nodes in each hidden layer, ridge regression coefficient, learning rate, and dropout rate were all allowed to vary creating a multidimensional search space of the changing hyperparameter settings. KerasTuner returned an optimal model configuration with one hidden layer containing 80 nodes, a learning rate of $\sim$ 2.6 x 10^{-5}, a ridge regression coefficient of 1 x 10^{-3}, and a dropout rate of 0.3. The model is allowed to run for 500 epochs with the small learning rate. Training is deemed complete by epoch 260 via an early stopping condition which monitors when the loss value in the validation set calculated after each epoch begins to consistently increase. The tuned SCL WR model has lesser accuracy scored by the RMSE of SFMR winds than the three most competitive models of the five originally tested (Figure 4.10a), but its variance in predicted WR is considerably lower and decreases at higher wind speeds (Figure 4.10b). The methods are compared in a 2-dimensional phase space defined by an x-axis of RMSE of all SFMR predictions in the testing set and a y-axis of variance for all predicted WRs in the testing set (Figure 4.11). A desirable location on the plot is the bottom left without being located too close to one of the axes which would indicate either a model that is too sensitive to noise and biases of the SFMR observations or predictions which are too invariant to capture the asymmetric nature of the wind field. The positioning of the SCL WR model (cyan dot; Figure 4.11) relative to the other models represents a successful tradeoff between SFMR accuracy and variance of WRs which was intended by combining the best methods for each of these metrics.

The performance metrics of the SCL RF model on the testing set are less than those of the previously-discussed MSE WR, MSE SFMR, and SCL SFMR methods with respect to its surface wind predictions in the testing set (Figure 4.9e). Regardless, the SCL WR model successfully combats the low bias at high winds most models struggle with while maintaining considerable scatter about the 1 to 1 line at high winds where SFMR winds are uncertain. The SCL WR model is also more accurate than the SF method. The method does have a notable high bias, particularly at lower wind speeds, but it is less pronounced than the SF technique (Figure 4.9a). This high bias

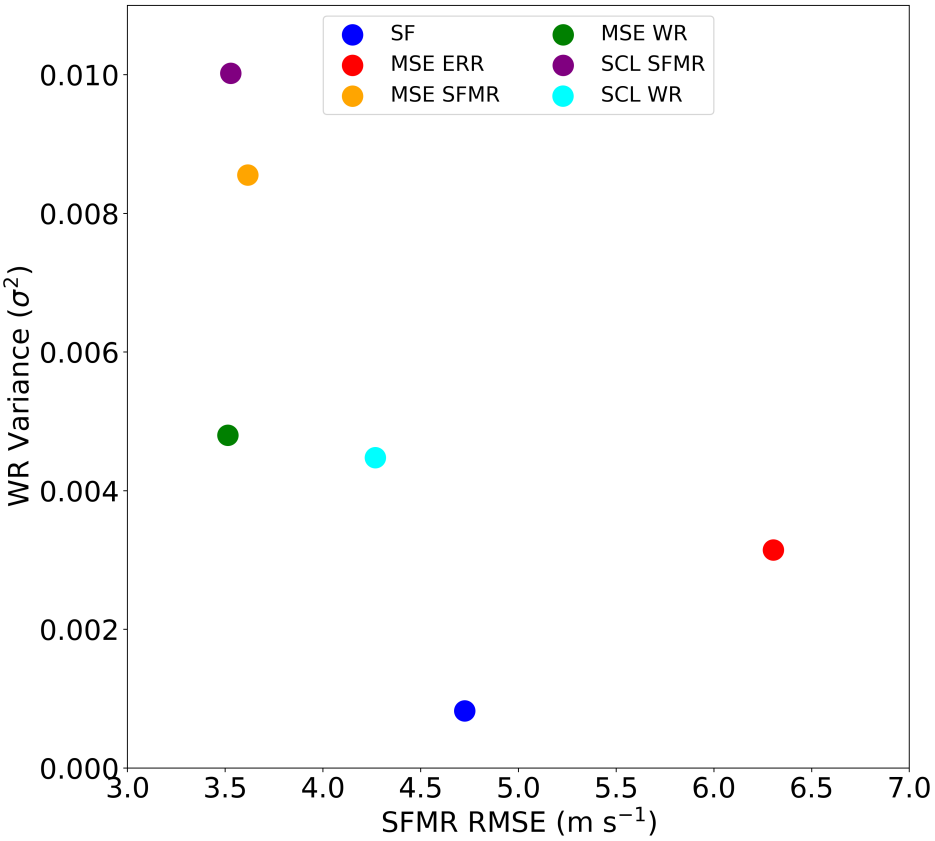

Figure 4.11: Performance of each prediction technique (legend) with respect to the variance (σ^2) of predicted wind ratios (WRs) and root mean squared error (RMSE) of all predicted SFMR winds compared to observed values in the testing set.

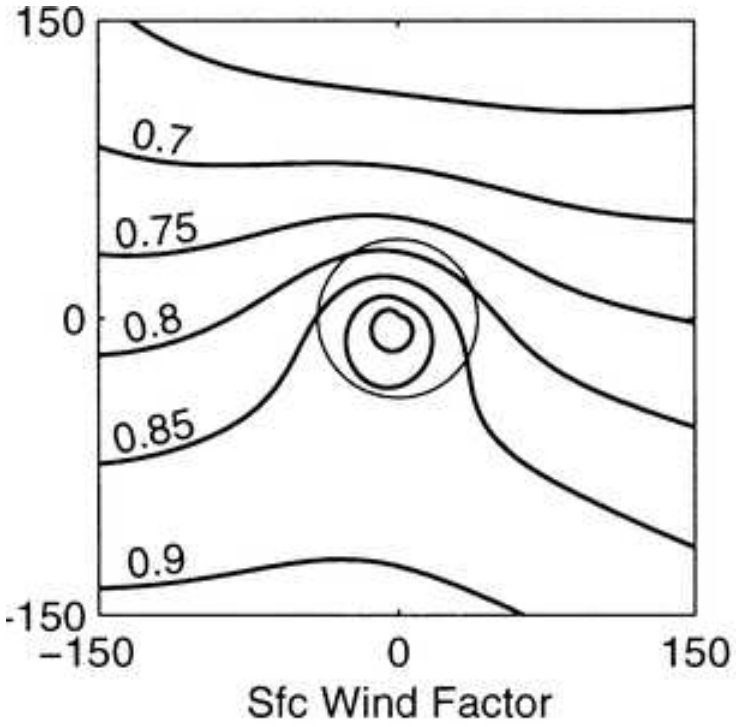

Figure 4.12: Surface wind reduction factor(using earth-relative winds), or WR, taken from Figure 5 in Kepert (2001).

may be a necessary compromise in creating a model for surface wind reduction that can be helpful for real-time V_{max} estimation based on SFMR observations which do not always contain V_{max}. The high bias decreases with magnitude of SFMR wind (not shown), which is a favorable trend when considering the decrease in SFMR-based intensity underestimation with increasing storm intensity characterized by Klotz and Nolan (2019) and the low bias in retrieved SFMR winds below 45 m s^{-1} (Sapp et al. 2019). To demonstrate the importance of this tradeoff, model performance is compared qualitatively to the theoretical WRs obtained with the simplified linear model of Kepert (2001). A spatial map of the WRs is given in Figure 4.12, which is borrowed from the original published study. The analysis is created for a simulated storm with maximum winds of 40 m s^{-1}, RMW of 40 km, and forward speed of 5 m s^{-1}. The direction of storm motion is to the west (left) and the highest WRs are found to the left of the TC motion vector.

To compare the models with the WRs predicted by theory, a similar case is selected from the TC-RADAR dataset and the flight-level wind field is reduced via the SF, SCL WR, MSE WR,

and SCL SFMR methods. Reconnaissance aircraft sampled Hurricane Zeta (2020) with TDR at category-1 intensity with a surface V_{max} of 80 kt (Blake et al. 2021), which is approximately 41.2 m s^{-1}. The flight-level RMW determined via the TDR data is 44 km and the forward motion is $\sim$ 7.5 m s^{-1}. These metrics are similar to the idealized TC used to approximate WRs with the linear model in Kepert (2001). RF fields are obtained for each reduction method by dividing the predicted surface wind field by the winds observed at flight level (Figure 4.13). All NN methods capture the left-to-right asymmetry in WRs present in the training data and predicted by theory. The SCL SFMR method is far too noisy in the inner core, with many contours packed closely together. The MSE WR method produces a more smooth WR field, but does not compare as well qualitatively with Figure 4.12 as the SCL WR model which exhibits smoother contours, especially to the left of motion in this case. The WRs predicted by the SCL WR model are notably higher than those in Figure 4.12, but the simple linear model underestimates the magnitude of winds in the PBL due to neglect of vertical advection and other nonlinear terms (Kepert and Wang 2001).

The surface wind fields produced for the Hurricane Zeta case by each method are provided in Figure 4.14. The SF method produces the strongest estimate of V_{max} which is within 2 m s^{-1} of the intensity assessed by the NHC, but there are key issues with the predicted surface wind field. The wind maximum is located directly below the maximum at flight-level which is not likely due to the slope of the eyewall with height. The static nature of the WRs also maintains the asymmetry of the wind observed at flight level to the surface. The MSE WR and SCL SFMR methods show more symmetric surface wind fields compared to flight level which should be correct due to the asymmetry in WRs opposing that of the flight-level winds. The surface wind maxima are located inward of the flight-level RMW. Despite the improved representation of general expected characteristics of the surface wind field, the maxima predicted by these two methods are much lower than that of the SF method. The V_{max} value of the SCL WR surface wind field is within $\sim$ 3 m s^{-1} of the operational estimate at this time. Although it is slightly weaker than the SF method maximum, the method captures the increased symmetry of the surface winds and inward

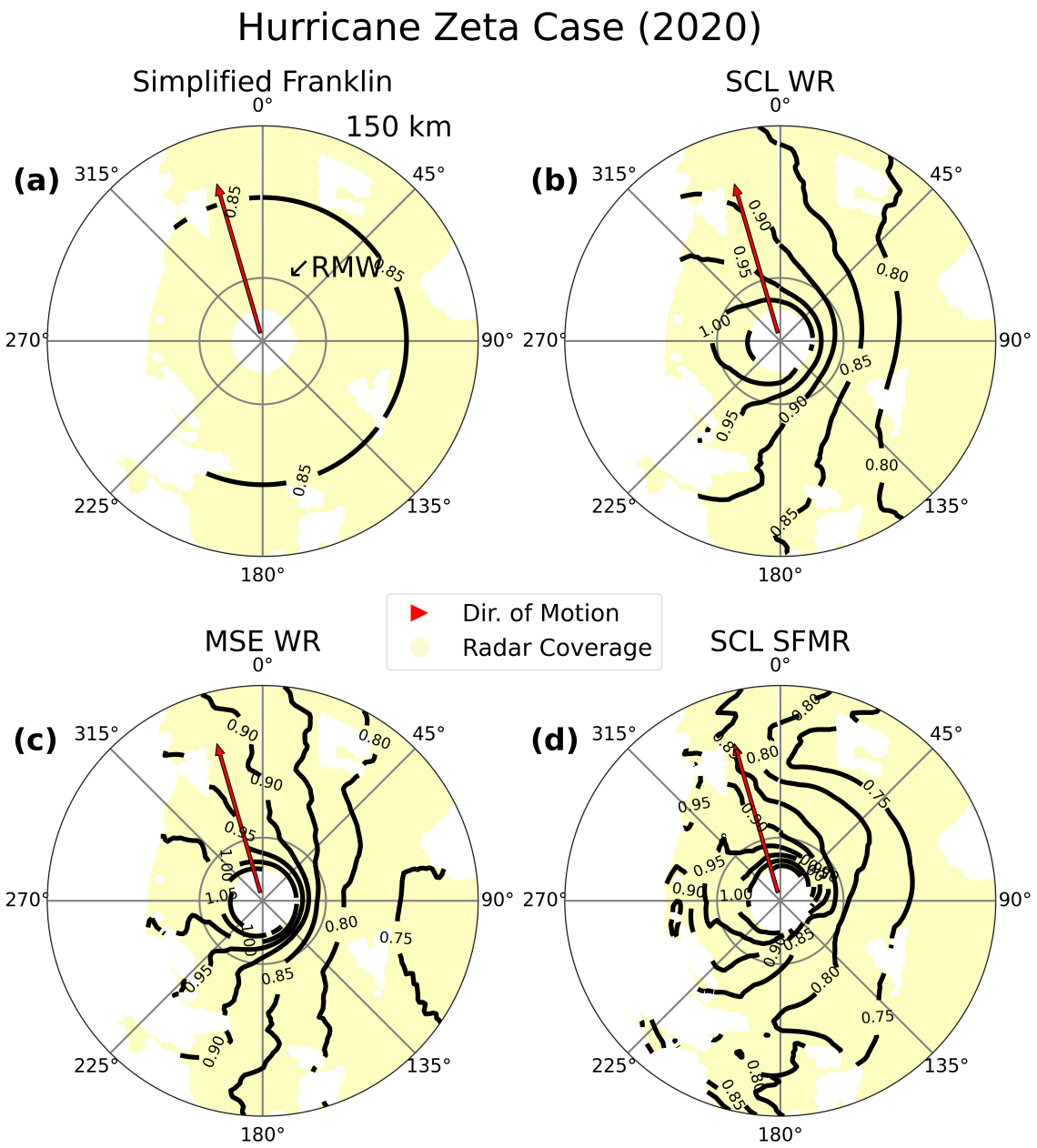

Figure 4.13: Spatial map or reduction factors between the predicted surface wind field and the smoothed wavenumber 0 + 1 flight-level wind field in TC-RADAR for the Hurricane Zeta (2020) case. Reduction fields are given for the (a) SF, (b) SCL WR, (c) MSE WR, and (d) SCL SFMR prediction techniques. Contours are only present where there is radar coverage which enables reduction. The storm motion direction is given (red arrow).

displacement of the strongest winds from the flight-level RMW which is a better representation of reality.

4.3.3 Model Performance Evaluation

The SCL WR model is found to be the most suitable technique for surface wind reduction and is compared in detail to the SF method, which is similar to operational procedures for surface wind reduction. Performance of the model on the FLIGHT+ dataset is evaluated with the training, validation, and testing sets in Figure 4.15. The SCL WR model outperformed the SF technique in both linear correlation and RMSE in the training, validation, and testing sets. The change in performance between methods for each set is compared through changes in the scatter plots of predicted versus true SFMR values. Observations are grouped in 225 bins with 5 m s^{-1} spacing between 10 and 85 m s^{-1} of true and predicted SFMR winds for each method. The bin counts for each method are subtracted (SCL WR - SF) and normalized across all sets based on the maximum increase and decrease of counts observed in each set (Figure 4.15c,f,i). In general, the SCL WR model tends to cluster more observations near the 1 to 1 line for predictions and observations with higher predictions more common at higher winds thanks to the SCL loss function multiplier.

To perform a more definitive evaluation of these methods which moves beyond the SFMR data, predicted surface wind values are co-located with dropwindsonde observations from past reconnaissance flights. Flight-level wind fields at 3000 m altitude in storms of hurricane or greater strength and 1500 m in storms of tropical storm strength are fed into the SCL WR model with their relevant predictors. The TC-RADAR analyses used to produce the flight-level wind fields are merged analyses, meaning they incorporate data from several radial flight legs through the storm. The collection of data over multi-hour periods increases coverage of the wind field analysis, but causes some temporal smoothing of the maximum winds at flight level. When a predicted surface wind value can be co-located with a dropwindsonde surface wind estimate from TC-DROPS in the r* and θ* coordinate space, the values are compared to obtain error statistics. The greater spatial coverage of merged analyses makes co-location of predictions and dropwindsondes more

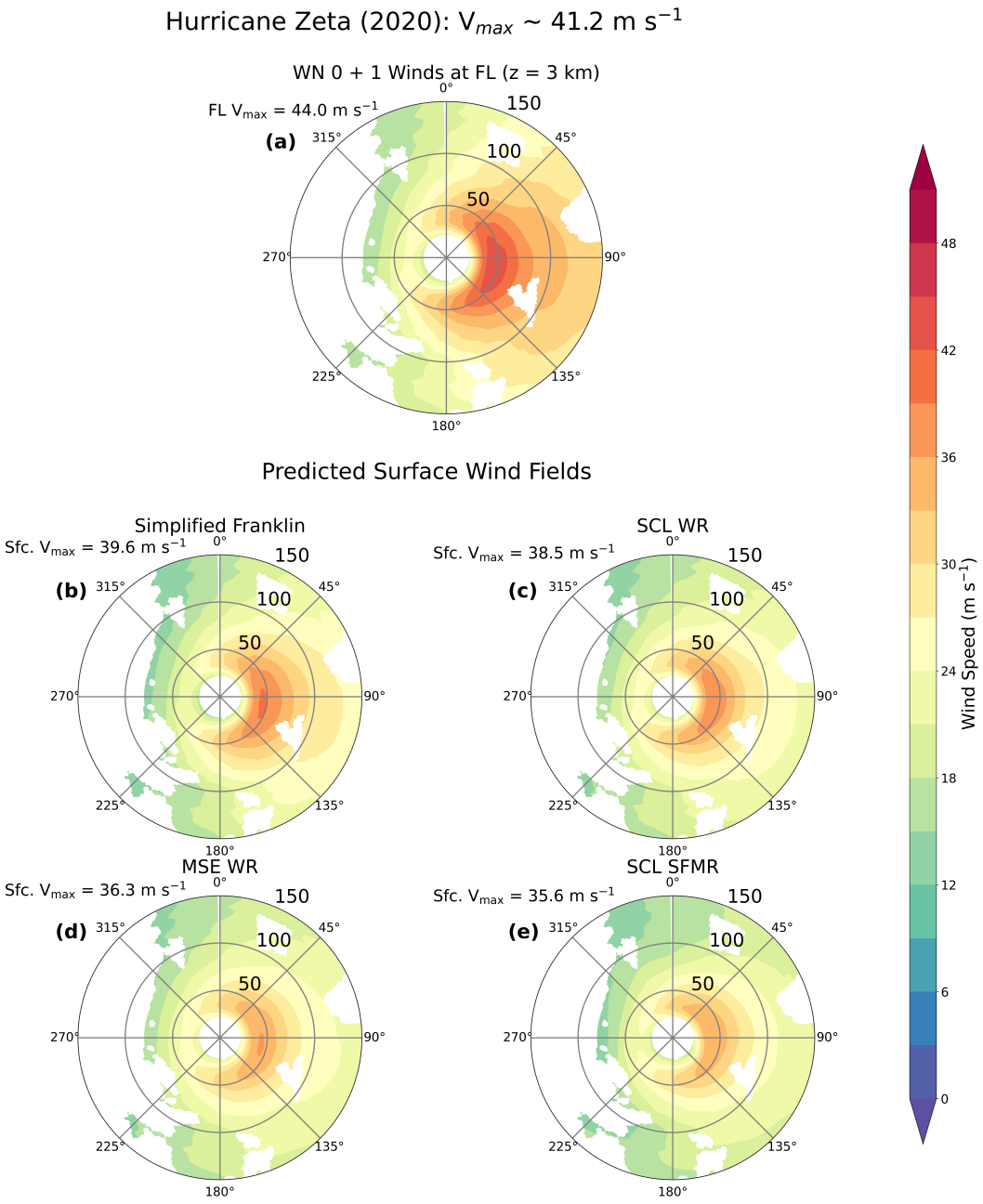

Figure 4.14: (a) Flight-level (FL) wind field at an altitude of 3 km from the Hurricane Zeta case in TC-RADAR collected near 12 UTC 28 August 2020 at category-1 intensity with the maximum observed wind at FL given. Predicted surface wind fields are given for the (b) SF, (c) SCL WR, (d) MSE WR, (e) SCL SFMR techniques with the maximum surface wind speed in the predicted field.

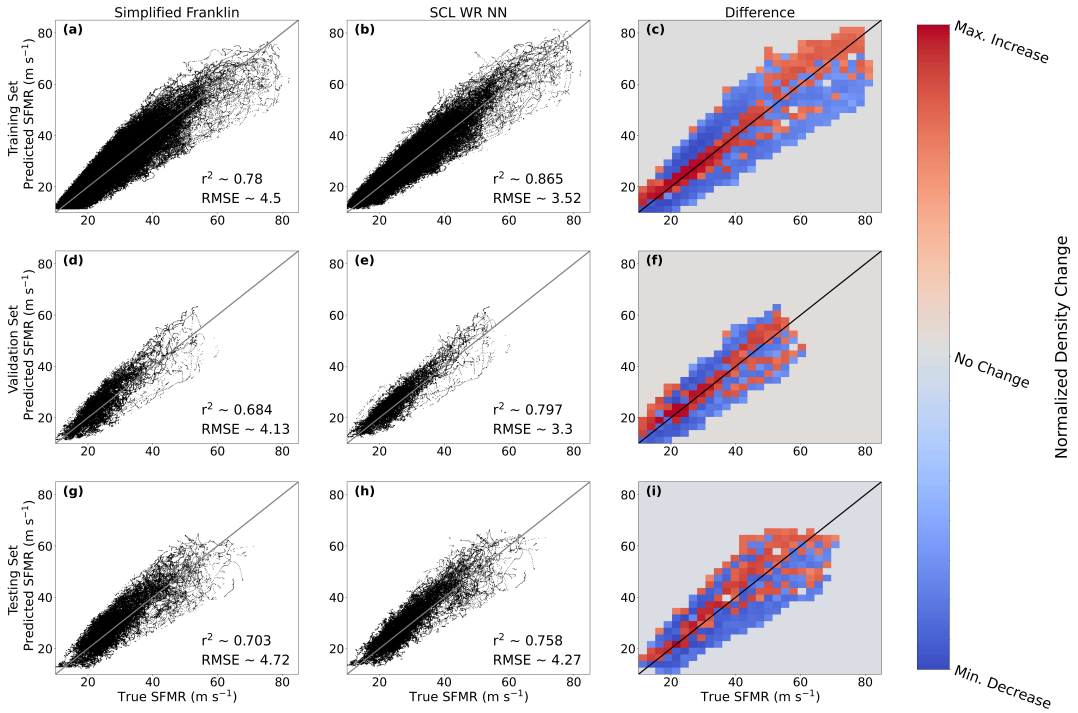

Figure 4.15: Predicted versus observed SFMR values with linear correlation (r^2) and root mean squared error (RMSE) values for the (a) SF and (b) SCL WR prediction techniques with normalized density change (from SF to SCL WR) heat map (c) for the training set, (d,e,f) validation set, and (g,h,i) testing set.

likely, but the temporal smoothing of winds makes the prediction of high winds more challenging. This also contributes to the underpredictions of V_{max} in the Hurricane Zeta case (Figure 4.14). The spatial coverage of the comparisons in storms with operational intensities classified as tropical storms, hurricanes (category 1 or 2), and major hurricanes (category 3+) is shown out to r* of 4 in Figure 4.16. Storms of major hurricane and hurricane intensity are sampled far more frequently than tropical storms in the TC-DROPS dataset as these storms are typically longer duration. The largest errors tend to be observed in major hurricanes where the SF method consistently underestimates winds near and inward of the flight-level RMW to the left of motion. The SCL WR method greatly reduces these errors with its predicted increase in symmetry of the surface winds. The large spread of errors in prediction of dropwindsonde surface winds is indicative of the chaotic nature of point observations in the PBL where frictional drag on the winds create a more messy field than the flight-level winds observed in the free-troposphere. No method trained on surface data should

be able to capture all of the variance within the TC-DROPS dataset without considerable risk of overfitting.

The prediction errors are binned by observed surface wind speed in bins of 15-30, 30-45, 45-60, and 60+ m s^{-1} (Figure 4.17). The 0 - 15 m s^{-1} bin is excluded since the model is not intended to reduce flight level winds below 15 m s^{-1}, and surface winds below 15 m s^{-1} are likely not to be of interest to the NHC, which forecasts wind radii beginning at tropical storm force (Sampson and Knaff 2015). Both methods overestimate winds below 45 m s^{-1}, but this could help mitigate the challenge of SFMR observations underestimating V_{max} in weaker storms (Klotz and Nolan 2019). In the 45 to 60 m s^{-1} range, the box and whisker plots indicate a reduction in the spread of errors compared to the SF method, with a mean error near 0 m s^{-1} for the SCL WR method. Observations of 60+ m s^{-1} surface winds are quite rare and can only be co-located with predictions from TC-RADAR flight-level winds 42 times. The SCL WR model still underestimates these winds but with a large reduction in spread and a lesser mean error which indicates the method is more capable of accurately predicting high winds in observed TCs. In all bins, the SCL WR model exhibits a lower RMSE than the SF method with the greatest improvements realized at the highest winds (Figure 4.17c).

4.3.4 Demonstration of Real-time Capability

These results show promise that the SCL WR method may be able to provide useful estimates of V_{max} with a surface wind field predicted from observed flight-level winds. A test case from Hurricane Idalia (2023) is used to demonstrate the operational capability of this reduction method. An aircraft collected TDR observations of Hurricane Idalia around 00 UTC 30 August 2023 at Category-2 intensity as it rapidly intensified in the Gulf of Mexico leading up to its landfall (Cangialosi and Alaka 2024). As this rapid intensification took place on approach to land, real-time intensity estimation of this system was of vital importance, making for a great test case of this technique. Doppler radar data from the TDR are QCed with the method developed by Gamache et al. (2008) and made available in real-time. The TDR data is synthesized into a wind field using

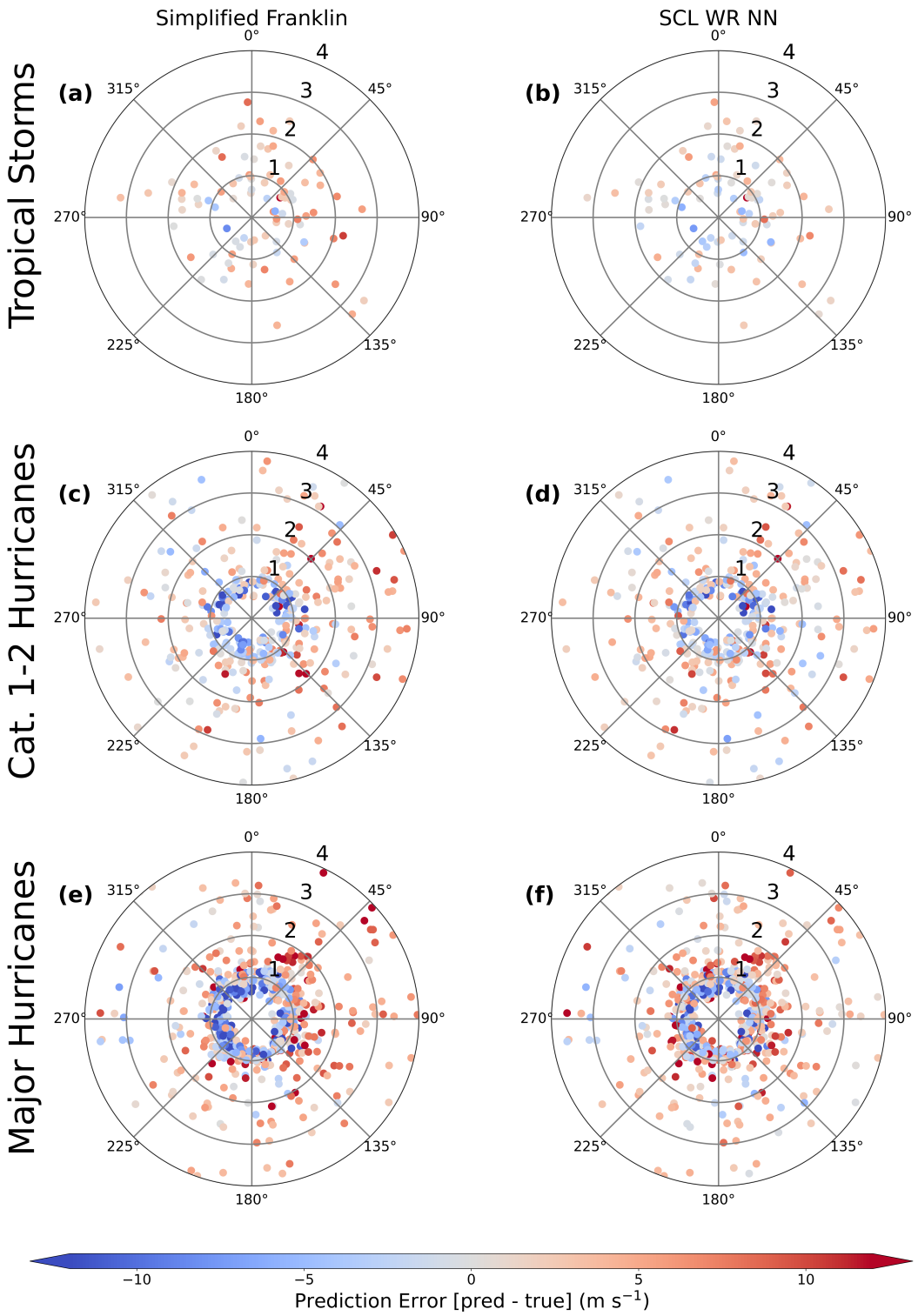

Figure 4.16: Errors (predicted - true; colorbar) of predicted surface winds with co-located surface wind dropsonde observations given in normalized polar coordinate space for the SF method in (a) tropical storms (n= 90), (c) Cat. 1-2 hurricanes (n = 363), and (e) major hurricanes (n = 592). Errors are also given for the SCL WR NN method (b,d,f).

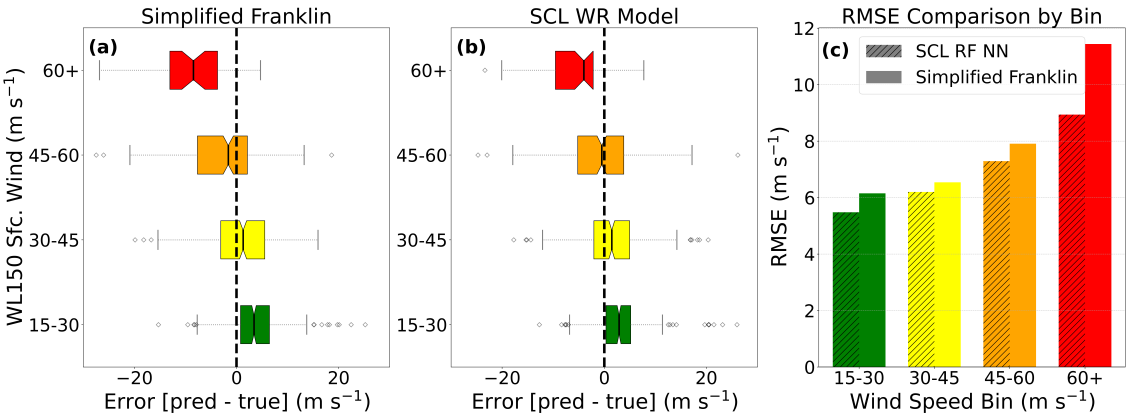

Figure 4.17: Box and whisker plots of errors (predicted - true) in surface wind predictions compared to dropsonde observations of surface winds in bins of 15 - 30 m s^{-1} (green; n = 413), 30 - 45 m s^{-1} (yellow; n = 382), 45 - 60 m s^{-1} (orange; n = 235), and 60+ m s^{-1} (red; n = 42) for the (a) SF and (b) SCL WR techniques. (c) Root mean squared error values are compared for both methods given as bars that correspond to each bin.

the Spline Analysis at Mesoscale Utilizing Radar and Aircraft Instrumentation (SAMURAI) software (Bell et al. 2012; Foerster and Bell 2017), which has been optimized to run at speeds suitable for real-time analysis (Dennis et al. 2023).

The flight-level wind field at an altitude of 3000 m is smoothed to WN 0 + 1 with a flight-level RMW analyzed to enable conversion to the normalized polar coordinates of r* and θ*. The necessary predictors for the NN, which would also be available in real-time, are paired to the flight-level wind data to allow the SCL WR model to predict a surface wind value at every grid point where radar-derived winds are available. The predicted surface wind and WR fields are shown with the flight-level winds in Figure 4.18. The asymmetric WR pattern acts to counteract the asymmetry at flight-level and produce a weaker, but more symmetric wind field at the surface. The analysis is from one radial pass through Idalia which takes on the order of an hour to complete. The shorter time period of the analysis helps to reduce temporal smoothing of the wind, but results in lesser radar coverage which is only continuous at all azimuths to approximately 50 km. The flight-level RMW is given as a dashed line, and the reduction factors have moved the surface wind maxima within the RMW, as is expected with an eyewall that slopes outward with height. The SCL SFMR model yields a surface wind maxima which is within 2 m s^{-1} of the operational estimate

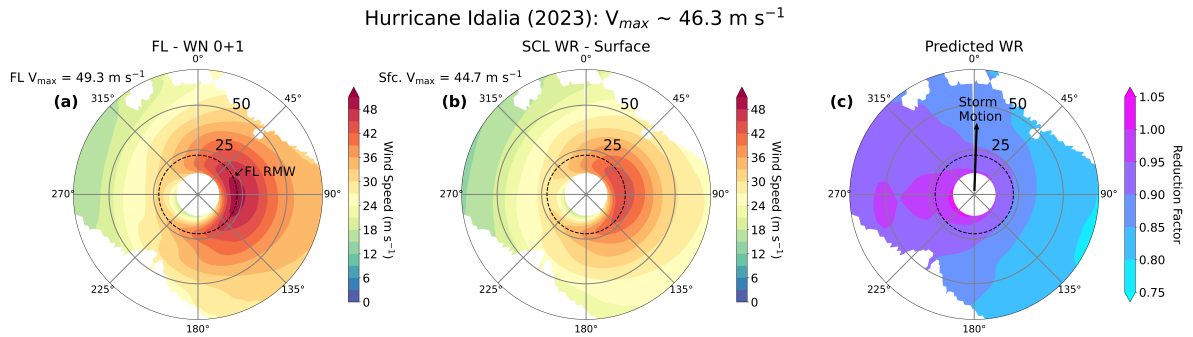

Figure 4.18: A pseudo-real-time product example of the SCL WR model reducing the observed flight-level wind field in Hurricane Idalia near 00 UTC 30 August 2023 at category-2 intensity. The (a) flight-level wind field at 3-km altitude, (b) predicted surface wind field and its maximum value, and (c) predicted WRs are shown with the flight-level radius of maximum wind (RMW) given as a dashed circle and storm motion direction (2°) provided as an arrow.

around this time, which is quite accurate considering the technique estimates this quantity from a smoothed radar-derived wind field.

4.4 Discussion

The WRs recommended by Franklin et al. (2003) are still used in operations today but are limited by static values which are incapable of characterizing the asymmetric nature of the TC wind field. This shortcoming is exacerbated when the method is extended beyond its original intention to reduce a full flight-level wind field down to the surface. Regardless, the SF method formulated here serves as a useful comparison to operational procedures when creating a new reduction method that accounts for motion-induced asymmetries due to frictional drag in the PBL (Shapiro 1983; Kepert 2001). The r*, θ*, and storm motion magnitude predictors give the NNs trained in this study necessary context to account for these broader-scale motion-relative asymmetries as well as large variability expected in the TC inner core near the RMW. Analysis of the motion-relative asymmetries of wind ratios in the Flight+ dataset in different intensity groups (Figures 4.6, 4.7, and 4.8) provides evidence that WRs are modulated by TC intensity. Powell et al. (2009) found this to be the case as well with one of their recommended wind reduction methodologies depending on inertial stability, which is a product of size and strength of the TC wind field. Stronger and intensifying TCs also tend to have more peaked radial wind profiles at flight level (Martinez et al.

2017) which impact the wind structure in the PBL by driving stronger inflow (Williams Jr. 2015). Inclusion of the most recent prior intensity estimate for a storm and the radial location of the flight-level RMW gives the NN information relevant to the inner-core winds.

The strongest contender, SCL WR, of the different NN methodologies evaluated for training a surface wind reduction model was identified by its ability to make reasonably accurate predictions of the surface wind while not exhibiting excessive variance in predicted WRs (Figure 4.11). Although for many ML studies, reducing error is seen as a positive, the known shortcomings of the SFMR training data (Sapp et al. 2019) underscore the dangers of learning the noise and biases of an imperfect observational dataset. Improvements to the SFMR GMF are likely to continue which can improve the training data for this reduction method in the future, but additional understanding of sea surface behavior at high wind speeds will be necessary (Holthuijsen et al. 2012). Despite the noise of the SFMR, the SCL WR model is still able to create a reduction field (Figure 4.13a) that is qualitatively similar to the WRs from the linear PBL model (Figure 4.12) from Kepert (2001). The similarity provides strong evidence that NNs are a capable tool for finding true physical relationships present in noisy observational datasets. Attention was paid to the setup of the NN, physical nature of the behavior being modeled, and characteristics of the observing platforms which generate the training data to accomplish this goal. Differences between WRs predicted by linear theory and the SCL WR technique are expected. Neglect of nonlinear terms and vertical advection render the linear model insufficient to match the true nature of WRs in the TC environment (Kepert and Wang 2001). Vertical advection acts to strengthen the inflow layer in the PBL (Williams Jr. 2015) that imports angular momentum and maintains the TC inner-core wind maxima despite losses to frictional drag.

The PBL is also characterized by strong turbulence (Lorsolo et al. 2010) which can never be fully explained by a bulk wind reduction algorithm. Smaller-scale features such as mesovortices can further complicate the problem by locally enhancing wind speeds near the eyewall of intense TCs (Cha et al. 2020). No method should be able to fully eliminate the prediction errors the SCL WR method accrues when compared to point measurements of dropwindsondes in the complex

flow of the PBL within a TC. Although all techniques are imperfect, the improved prediction of high winds by the NN (Figure 4.17) is helpful in estimating V_{max} from a predicted surface wind field. The improved prediction is owed to the sensitivity of the SCL loss function to high winds (Figure 4.5). The NN trained by Eusbi et al. (2024), which was also tasked with capturing structural aspects of the TC wind field, was vastly improved by weighting their loss function using the wind speed magnitude. The SCL loss function modification presented in this study provides more control over the degree to which high winds are weighted in the loss function by changing the value of the shift parameter (Eq. 1). Their NN also benefited from physical knowledge by incorporating the Navier-Stokes equations into their loss function which is an inventive and novel strategy. However, the physics of the PBL are more complex than the free troposphere and the addition of physical insight to this predictive method will take additional future effort.

Successful demonstration of this method for real-time applications with the Hurricane Idalia (2023) case is an important mark of progress (Figure 4.18). The method offers the advantage of predicting a full surface wind field compared to the method of Powell et al. (2009), which is meant to estimate the singular value of a maximum surface wind. More work can be done to improve this method. An exhaustive sample of pseudo-real-time cases are needed to characterize biases of this technique. Future efforts to improve the NN wind reduction method should focus on the addition of new predictors which are also physically relevant to the problem. The presence and magnitude of vertical wind shear (VWS) in the TC environment is important to the kinematic organization of TCs (DeHart et al. 2014) and exerts control over the asymmetries the NN method aims to predict (Uhlhorn et al. 2014). VWS direction and magnitude from the Statistical Hurricane Intensity Prediction Scheme (DeMaria et al. 2005) would provide useful predictors for the NN which are available in real-time. Relating archived satellite data to the FLIGHT+ training set may also be helpful in systematically identifying regions of convection where WRs should be locally enhanced. However, each added predictor creates an additional dependency for the method to produce predictions so a balance must be maintained between added complexity and operational

feasibility. Continued care must be taken with the addition of new predictors to not inflate the technique's accuracy beyond what the observational uncertainties of the training data allows.

4.5 Conclusions

Tropical cyclone (TC) intensity and impacts depend on the surface wind field within the planetary boundary layer (PBL). These winds are rarely sampled directly due to the dangers of flying in the PBL where frictional effects make the flow field more chaotic and turbulent in comparison to the more predictable flow present in the free troposphere at altitudes where TC aircraft reconnaissance operates. The maximum sustained wind (V_{max}) and other characteristics of the wind field at the surface are reported and predicted by operational forecast centers. Methods to reduce flight-level wind observations to the surface help forecasters infer characteristics of the surface wind field for a more plentiful source of data. The reduction factors (RFs) obtained from vertical profile measurements of dropwindsondes in TCs by Franklin et al. (2003) are still employed in operations to estimate surface winds from flight-level data. These WRs consist of static values recommended for broad regions of the storm, separated by pressure altitude of the aircraft observations and inner versus outer core. A Simplified Franklin (SF) scheme was developed to automate the application of this method by interpolating between recommended WRs as a benchmark for comparison against results with new methods. Although the SF method is still useful, its invariant nature is not suited for capturing asymmetric WRs present in TCs induced by motion and other case-specific factors. Accurate prediction of these asymmetries is necessary to predict a realistic surface wind field from one observed at flight level.

The stepped frequency microwave radiometer (SFMR) mounted on TC reconnaissance aircraft detects emissivity from the ocean surface and atmosphere below the aircraft at six different C-band frequencies (Uhlhorn et al. 2007). The emissivities are related to surface wind speeds through a geophysical model function (GMF). The GMF is imperfect (Sapp et al. 2019) and continues to be improved, but the large volume of SFMR data enables the training of a neural network (NN) machine learning model which can discern useful relationships for surface wind reduction

amidst the noisy instrument observations. SFMR data collected from the 2016 to 2019 hurricane seasons provides surface wind observations which can be co-located with predictive flight-level features to train the NN. Mapping this data to a polar grid defined by a radius (r*) normalized by the radius of maximum wind (RMW) at flight level and storm-motion-relative azimuths (θ*) puts the observations in a common grid space to understand the asymmetric characteristics of the bulk observational data. The wind ratio (WR) obtained by dividing SFMR surface winds by their corresponding flight observations forms the physical basis for reduction factors (RFs), discussed in previous work. Analyzing the distribution of WRs with respect to radius in storm-motion-relative quadrants in different intensity groups indicates WRs around the TC should change based on storm motion, intensity, and structure.

Several different NNs were trained to predict surface wind from flight-level predictors which provide necessary context to predict storm-scale variance in RFs. The SCL WR method was the most suited for the task of the different methods evaluated due to its ability to accurately predict surface winds without too much variance in predicted WRs which would indicate a model that is sensitive to the biases and noise of SFMR data. The NN method exhibits a high bias at winds below major hurricane force, but this may be beneficial to operational estimation of V_{max} from the predicted surface wind field. The high bias acts against a low bias of the SFMR GMF below 45 m s^{-1} and the systematic undersampling of V_{max} by the SFMR due to the inability to directly sample the maximum winds with aircraft during every flight, especially in weaker TCs (Klotz and Nolan 2019). The method benefits from a custom shifted cubic loss (SCL) function which exponentially increases the loss penalty assessed on prediction errors for rare, but important high wind observations in the dataset. The SCL custom loss function method may be useful for other machine learning applications where accurate prediction of rare extreme values is of importance. The SCL WR model compares well qualitatively to theoretical WRs calculated with a linear PBL model (Kepert 2001), indicating NNs are capable of learning physical relationships within noisy observational datasets.

Radar-derived flight-level wind fields from past reconnaissance flights are smoothed to wavenumber 0 + 1 and reduced to the surface by the SCL WR and SF methods. The predicted surface winds are compared to in-situ dropwindsonde measurements of surface winds from the same flights when co-location is possible. Mapping dropwindsonde prediction errors in the r* and θ* coordinate space indicates that much of the improvement is due to the ability of the SCL WR model to accurately predict the higher WRs expected left of storm motion. Errors are also reduced within the flight-level RMW where WRs must increase to predict the surface wind maxima located here below weaker winds aloft due to the outward slope of the eyewall with height. The SCL WR method improves upon the accuracy of the SF method in all intensity-based bins of dropwindsonde observations ranging from 15 m s^{-1} to 60+ m s^{-1}. Although in-situ observations of winds in the highest bin are rare, the greatest improvements in root mean squared error (RMSE) are realized at the highest winds which are important to intensity estimation in strong TCs.

When other analysis tools are used in conjunction with the SCL WR model, a surface wind field can be generated in real-time for a TC to assist forecasters in the task of estimating and predicting metrics related to the surface winds. A pseudo-real-time demonstration with data available from an aircraft reconnaissance flight into Hurricane Idalia (2021), while it was rapidly intensifying leading up to its landfall, yields promising results. The predicted surface wind field is weaker, but more symmetric than the one observed at flight level with a maxima located inward of the flight-level RMW. These characteristics are consistent with expectations based on theory and observations. The maximum value of the predicted surface wind field is within 2 m s^{-1} of the operational intensity estimate at the time of the flight. Results from this test case are encouraging, but a more exhaustive test with more pseudo-real-time cases is required to gauge the utility of this method for real-time intensity estimation and forecaster support. The method can be improved in the future through the addition of more predictors relevant to TC wind field asymmetry such as vertical wind shear (VWS), but predictors should be added with caution to maintain a balance between model accuracy and operational feasibility as more components become necessary for prediction.

Chapter 5

Conclusions

The internal structure of tropical cyclones (TCs) is important to intensity change behavior and the hazards posed by these storms. While considerable progress has been made investigating the impacts of radial and azimuthal aspects of TC intensity, vertical structure has not been explored as extensively (Chen et al. 2023). A combined approach leveraging observations, numerical modeling and machine learning (ML) techniques advances our understanding of TC vertical structure. Observations are used to provide evidence of relationships between TC vertical structure and intensity change which inform the analysis techniques and setup of numerical modeling experiments. ML is a powerful tool capable of picking out important physical relationships in large observational datasets which can further our understanding of vertical structure. This dissertation aims to define the role vertical structure plays throughout the TC intensification process as well as its importance to determining the winds these storms possess near the surface in the frictional planetary boundary layer (PBL).

In chapter 2, a large dataset of kinematic analyses (TC-RADAR) allows for the characterization of the height of the TC vortex (HOV) in storms observed by tail Doppler radar (TDR). HOV is determined by a thershold-based technique which tracks the decay of the azimuthally-averaged tangential winds of a TC with height along its radius of maximum winds (RMW). A fixed threshold HOV (HOV24), determined by the last height at which 24 m s^{-1} tangential winds are observed, has a strong relationship with the current intensity of a TC. The HOV24-intensity relationship offers additional confirmation in a novel observational database of the vertical growth of the vortex as TCs grow more intense. A dynamic HOV (DHOV) metric uses a threshold value of 40% of the maximum tangential winds found in the lower levels at 2-km altitude, which has reduced dependence on current TC intensity. Distributions of DHOV observations grouped by intensity change exhibit statistically significant differences between groups, offering the first published statistically-significant observed evidence of taller vortices being more likely to intensify. Observed TCs which

underwent rapid intensification (RI) in the 24-hour period following observation always possess deep vertical vortex structure. Storms intensifying at rates not meeting a pressure-based RI threshold are preferentially taller than steady-state storms.

A taller vortex should be more capable of efficiently lowering the minimum sea level pressure (P_{min}) during intensification (DesRosiers et al. 2022) as compared to a shorter one. However, DHOV was also found to have a strong relationship with environmental vertical wind shear (VWS), in which larger DHOV is favored in lower VWS environments. VWS is known to relate to TC intensity change and acts to tilt the vortex downshear and cause the low- and mid-level centers of a TC to become misaligned, inhibiting intensification (DeMaria 1996). A more thorough investigation of the DHOV dataset from TC-RADAR reveals that vortex alignment is likely the most important contributing factor to the observed signal for the relationship between DHOV and intensity change found in chapter 2. The absence of smaller DHOV values when observations are limited to cases where vortex tilt is small suggests that once TCs reach tropical storm strength, there are no “short" vortices, only tilted ones. DHOV values are not a product of vortex tilt alone. In aligned storms, DHOV increases as the storm grows more intense, prompting continued investigation to disentangle the contributions of both vortex alignment and vertical vortex growth to changes in TC vertical structure.

In chapter 3, the evolution of DHOV in TCs is tracked in numerical model simulations to provide a physical explanation for the observed relationship between DHOV and intensity change found in chapter 2. The analysis provides more clarity on the role of vertical structure throughout the intensification process with greater temporal resolution than observations can provide. An ensemble of simulated TCs exposed to VWS, originally generated by (Tao and Zhang 2014), experience initial vortex tilt, followed by alignment and RI with varied timing. Centering the TC evolution on vortex alignment reveals three distinct regimes of the intensification process in the presence of VWS separated by a large jump in DHOV. The early, pre-alignment, phase is characterized by weak tilted vortices which intensify slowly as the tilt between the low- and mid-level centers is decreased. DHOV values are small during this period due to weak tangential winds in

the upper levels in the azimuthal average taken about storm center, which is used to calculate the metric. Prior to the complete reduction of vortex tilt, when the centers are adequately aligned, dynamic HOV increases rapidly during the active alignment phase. The delay between the DHOV increase and the onset of RI which occurs at the end of the active alignment phase offers evidence that the jump in DHOV may be an important necessary condition and precursor signal for RI.

At the conclusion of the active alignment phase, the development of a warm core temperature perturbation in the upper levels of the TC and onset of RI signals the start of the post-alignment vertical growth phase. During the vertical growth phase, the upper-level warm core strengthens and modulates the decay of the tangential wind field with height. DHOV continues to grow as the upper-level warm core and tangential winds intensify in concert throughout the continuing RI process. The clearly identifiable intensification regimes which emerge when centering analysis on the jump in DHOV suggest a distinction between DHOV increases gained through alignment versus the continued growth of DHOV linked to kinematic and thermodynamic intensification of the TC in the upper levels of the atmosphere. Distinctive behavior of DHOV in each phase shows the metric is useful for evaluating TC vertical structure throughout the TC lifecycle. DHOV provides continuous diagnostic information while effectively bridging the gaps between several different stages of TC development which are studied in the literature due to their significance to TC intensity change.

The importance of post-alignment vertical growth and increasing DHOV during this phase of TC intensification is explored in an additional pair of numerical model experiments. A control simulation (CTRL) allows a simulated TC to intensify in a conducive environment with no VWS while another develops in a parallel simulation in the presence of an upper-level jet of VWS (ULJET). The simulated TC in CTRL reaches extreme intensities while developing a component of the warm core in the upper levels, which extends to the interface between the upper-tropospehre and lower-stratosphere (UTLS). This UTLS warm core feature is similar to that of previous observed (Duran and Molinari 2018) and simulated TCs (Ohno 2015; Chen and Zhang 2013b) of extreme intensity. The model TC in ULJET undergoes RI which is initially similar to the CTRL simulation,

but the process is halted and its peak intensity and DHOV are capped by the presence of the upper-level jet of VWS. The differences between CTRL and ULJET suggest that the UTLS component of the TC warm core may be a critical element for the continuation of RI and the ability of TCs to reach extreme intensities.

The findings relating DHOV to intensity change offer continued avenues for research on vertical structure of the tangential wind field and its importance to TC intensification and RI. Further investigation of the processes by which the vortex aligns and begins to establish in the upper levels during the active alignment phase can improve our understanding of the mechanisms which set the stage for RI. Future case studies of storms observed during the active alignment phase would help to identify these processes. The jump in DHOV is an important signal for subsequent RI events in TCs, which could be evaluated in real-time in storms that are observed by airborne radar. With low DHOV indicating vortex tilt which prevents RI and the metric's continued growth during RI in more intense TCs, availability of real-time DHOV estimates could aid forecasters in intensity prediction. The sensitivity of TC intensity to upper-level development, VWS in the upper troposphere, and model parameterizations which can impact upper-level processes may also have important implications to the potential peak intensities these storms can reach in the aligned vertical growth phase.

TC intensity is classified by the maximum surface wind speed (V_{max}) within the PBL, which is governed by more complicated physics than the free troposphere where most reconnaissance aircraft observations are gathered. Frictional impacts within the PBL act to reduce the wind speeds at the surface and wind ratios (WRs) are an important tool for operational forecasters to estimate winds at the surface from those observed by aircraft in the free troposphere. The TC wind fields at flight level and the surface are asymmetric (Uhlhorn et al. 2014) and the differential impacts of frictional surface drag (Shapiro 1983) lead to asymmetries in WRs due in part to TC motion (Kepert 2001), that are not adequately accounted for in the current WRs used operationally.

In chapter 4, a dataset of flight-level observations co-located with surface winds retrieved by the stepped frequency microwave radiometer (SFMR) is used to explore the asymmetries that exist

in WRs and train a ML method to predict surface wind from flight-level observations. Analysis of the dataset in storms of varying intensity in a coordinate space of r* and θ*, which is relative to TC motion and scaled by the location of the flight level RMW, shows the importance of location and current TC intensity to accurate reduction of flight-level wind observations to the surface. High winds are rarely observed and often localized to small areas within the inner core, but these peak winds are of vital importance to operational TC intensity estimation. A custom shifted cubic loss (SCL) function is designed and employed to ensure the model prioritizes the correct classification of these limited observations in the training dataset.

Among many candidate neural network (NN) models tested, the SCL WR model, which is trained to predict WRs with the SCL function, is found to be the most capable for predicting surface winds from flight-level variables. The NN uses a suite of predictors which are available in real-time during TC reconnaissance flights to produce a surface wind field. Predictions are validated against in-situ measurements of surface winds from dropwindsondes, which are expendable instruments that record atmospheric variables from the aircraft to the surface. Validation statistics reveal the NN predicts surface winds with greater accuracy than a procedure similar to the one employed operationally at the National Hurricane Center (NHC). The improvements are mainly due to the model's ability to capture asymmetries in the WR field as well as increased WRs within the flight-level RMW, where the outward slope of the TC eyewall with height necessitates the increase. The greatest improvements are realized at high wind speeds important to the estimation of V_{max} in strong TCs. A pseudo-real-time test of the NN on a flight into Hurricane Idalia (2023) indicates the method can produce a realistic wind field with a V_{max} similar to that assessed operationally.

Beyond the immediate benefit of a more accurate wind reduction that can be run operationally at the NHC, the results have broader implications. The SFMR observations the model is trained on are known to be quite noisy and can situationally struggle to produce reliable wind speed estimates (Sapp et al. 2019). Despite the shortfalls of the SFMR training data, the NN method is able to discern and utilize the physical relationships present in the dataset and create a WR field which is consistent with theory. Further testing is needed to quantify the accuracy of the method with other

pseudo-real-time cases, and the results of these experiments allow for improved understanding of where and when the existing operational wind reduction method is inadequate. This effort can improve our understanding of vertical TC wind field structure between the lower levels of the free troposphere and the PBL. The model can also be retrained with a more expansive sample of historical SFMR data via reprocessing with the current surface wind retrieval algorithm. Other instruments which measure surface winds, such as buoys and newer emerging technologies, can be incorporated as additional training and validation data for the NN.

The preceding chapters of this dissertation represent a body of work which jointly moves forward our understanding of the vertical structure of the TC wind field. Analysis of a collection of airborne radar data in TCs both re-confirms the intensity-HOV relationship and provides novel proof that the decay of the vortex tangential wind field with height, via DHOV, is important to TC intensity change behavior. Analysis of an ensemble of numerical model simulations disentangles the contributions of VWS-induced vortex tilt and aligned upper-level development to changes in DHOV throughout TC intensification. The DHOV metric introduced here is a useful diagnostic metric for vertical structure throughout the TC lifecycle. Additional numerical model simulations illuminate the role of upper-level development of the TC wind field and warm core in enabling extreme intensities. The nature of the change of TC wind magnitude with height is different, but remains important to TC intensity near the surface in the frictional PBL. Development of a NN wind reduction method provides an improvement over current operational procedures that can aid NHC forecasters in real-time intensity estimation. Furthermore, the NN learns and replicates important physical relationships which govern reduction factors despite the noisy nature of its observational training data. The advances described here open new avenues for research which can continue to improve our understanding of TC vertical structure and how it relates to intensity change and estimation.

Bibliography

Aircraft Operations Center, 2016: Tropical cyclone operations: Challenges in 2015; New products and services planned for 2016 and 2017. NOAA Office of Marine and Aviation Operations, cited: 2020-09-29, [Available online at https://www.ofcm.gov/meetings/TCORF/ihc16/2016presentations.html].

Alland, J. J., B. H. Tang, K. L. Corbosiero, and G. H. Bryan, 2021: Combined effects of midlevel dry air and vertical wind shear on tropical cyclone development. Part i: Downdraft ventilation. *Journal of the Atmospheric Sciences*, **78**, 763–782, doi: 10.1175/JAS-D-20-0054.1.

Bell, M. M., M. T. Montgomery, and K. A. Emanuel, 2012: Air–sea enthalpy and momentum exchange at major hurricane wind speeds observed during CBLAST. *Jounral of the Atmospheric Sciences*, **69**, 3197–3222, doi: doi.org/10.1175/JAS-D-11-0276.1.

Beven, J. L., R. Berg, and A. Hagen, 2019: National Hurricane Center tropical cyclone report: Hurricane Michael (AL142018). NHC Tech. Rep.

Blake, E., R. Berg, and A. Hagen, 2021: National Hurricane Center tropical cyclone report: Hurricane Zeta (AL282020). NHC Tech. Rep.

Boukabara, S.-A., V. Krasnopolsky, J. Q. Steward, E. S. Maddy, N. Shahroudi, and R. N. Hoffman, 2019: Leveraging modern artificial intelligence for remote sensing and NWP: Benefits and challenges. *Bulletin of the American Meteorological Society*, **100 (12)**, ES473–ES491, doi: 10.1175/BAMS-D-18-0324.1.

Bryan, G. H., and M. J. Fritsch, 2002: A benchmark simulation for moist nonhydrostatic numerical models. *Monthly Weather Review*, **130**, 2917–2928, doi: 10.1175/1520-0493(2002)130<2917:ABSFMN>2.0.CO;2.

Bryan, G. H., and R. Rotunno, 2009: The maximum intensity of tropical cyclones in axisymmetric numerical model simulations. *Monthly Weather Review*, **137**, 1770–1789, doi: 10.1175/2008MWR2709.1.

Cangialosi, J. P., and L. Alaka, 2024: National Hurricane Center tropical cyclone report: Hurricane Idalia (AL102023). NHC Tech. Rep.

Cangialosi, J. P., E. Blake, M. DeMaria, A. Penny, A. Latto, E. Rappaport, and V. Tallapragada, 2020: Recent progress in tropical cyclone intensity forecasting at the National Hurricane Center. *Weather and Forecasting*, **35 (5)**, 1913–1922, doi: 10.1175/WAF-D-20-0059.1.

Carrasco, C. A., C. W. Landsea, and Y.-L. Lin, 2014: The influence of tropical cyclone size on its intensification. *Weather and Forecasting*, **29**, 582–590, doi: 10.1175/WAF-D-13-00092.1.

Casas, E. G., D. Tao, and M. M. Bell, 2023: An intensity and size phase space for tropical cyclone structure and evolution. *Jounral of Geophysical Research: Atmospheres*, **128**, e2022JD037 089, doi: 10.1029/2022JD037089.

Cha, T.-Y., M. M. Bell, W.-C. Lee, and A. J. DesRosiers, 2020: Polygonal eyewall asymmetries during the rapid intensification of Hurricane Michael (2018). *Geophysical Research Letters*, **47**, e2020GL087 919, doi: 10.1029/2020GL087919.

Chen, H., and S. G. Gopalakrishnan, 2015: A study on the asymmetric rapid intensification of Hurricane Earl (2010) using the HWRF system. *Journal of the Atmospheric Sciences*, **72**, 531–550, doi: 10.1175/JAS-D-14-0097.1.

Chen, H., and D.-L. Zhang, 2013a: On the rapid intensification of Hurricane Wilma (2005). part ii: Convective bursts and the upper-level warm core. *Journal of the Atmospheric Sciences*, **70 (1)**, 146–162, doi: 10.1175/JAS-D-12-062.1.

Chen, H., and D.-L. Zhang, 2013b: On the rapid intensification of Hurricane Wilma (2005). Part II: Convective bursts and the upper-level warm core. *Journal of Atmospheric Science*, **70**, 146–162, doi: 10.1175/JAS-D-12-062.1.

Chen, X., and Coauthors, 2023: Research advances on internal processes affecting tropical cyclone intensity change from 2018–2022. *Tropical Cyclone Research and Review*, **12**, 10–29, doi: 10.1016/j.tcrr.2023.05.001.

Choudhury, D., and S. Das, 2017: The sensitivity to the microphysical schemes on the skill of forecasting the track and intensity of tropical cyclones using WRF-ARW model. *Journal of Earth System Science*, **126**, 1–10, doi: 10.1007/s12040-017-0830-2.

DeHart, J. C., R. A. Houze Jr., and R. F. Rogers, 2014: Quadrant distribution of tropical cyclone inner-core kinematics in relation to environmental shear. *Journal of the Atmospheric Sciences*, **71**, 2713–2732, doi: 10.1175/JAS-D-13-0298.1.

DeMaria, M., 1996: The effect of vertical shear on tropical cyclone intensity change. *Journal of the Atmospheric Sciences*, **53**, 2076–2088, doi: 10.1175/1520-0469(1996)053<2076:TEOVSO>2.0.CO;2.

DeMaria, M., M. Mainelli, L. K. Shay, and J. Knaff, John A.and Kaplan, 2005: Further improvements to the Statistical Hurricane Intensity Prediction Scheme (SHIPS). *Weather and Forecasting*, **20**, 531–543, doi: 10.1175/WAF862.1.

DeMaria, M., C. R. Sampson, J. A. Knaff, and K. D. Musgrave, 2014: Is tropical cyclone intensity guidance improving? *Bulletin of the American Meteorological Society*, **95**, 387–398, doi: 10.1175/BAMS-D-12-00240.1.

Dennis, J. M., A. H. Baker, B. Dobbins, M. M. Bell, J. Sun, Y. Kim, and T.-Y. Cha, 2023: Enabling efficient execution of a variational data assimilation application. *The International Journal of High Performance Computing Applications*, **37**, 101–114, doi: 10.1177/10943420221119.

DesRosiers, A. J., and M. M. Bell, 2024: Airborne radar quality control with machine learning. *Artificial Intelligence for the Earth Systems*, **3 (1)**, e230 064, doi: 10.1175/AIES-D-23-0064.1.

DesRosiers, A. J., M. M. Bell, and T.-Y. Cha, 2022: Vertical vortex development in Hurricane Michael (2018) during rapid intensification. *Monthly Weather Review*, **150**, 99–114, doi: 10.1175/MWR-D-21-0098.1.

DesRosiers, A. J., M. M. Bell, P. J. Klotzbach, M. S. Fischer, and P. D. Reasor, 2023: Observed relationships between tropical cyclone vortex height, intensity, and intensification rate. *Geophysical Research Letters*, **50**, e2022GL101 877, doi: 10.1029/2022GL101877.

Didlake Jr., A. C., and M. R. Kumjian, 2018: Examining storm asymmetries in Hurricane Irma (2017) using polarimetric radar observations. *Geophysical Research Letters*, **45**, 13 513–13 522, doi: 10.1029/2018GL080739.

Dunion, J. P., 2011: Rewriting the climatology of the tropical north Atlantic and Caribbean sea atmosphere. *Journal of Climate*, **24**, 893–908, doi: 10.1175/2010JCLI3496.1.

Dunion, J. P., and C. S. Marron, 2008: A reexamination of the jordan mean tropical sounding based on awareness of the Saharan air layer: Results from 2002. *Journal of Climate*, **21**, 5242–5253, doi: 10.1175/2008JCLI1868.1.

Duran, P., and J. Molinari, 2018: Dramatic inner-core tropopause variability during the rapid intensification of Hurricane Patricia (2015). *Monthly Weather Review*, **146 (1)**, 119–134, doi: 10.1175/MWR-D-17-0218.1.

Duran, P., and J. Molinari, 2019: Tropopause evolution in a rapidly intensifying tropical cyclone: A static stability budget analysis in an idealized axisymmetric framework. *Monthly Weather Review*, **76 (1)**, 209–229, doi: 10.1175/JAS-D-18-0097.1.

Ebert-Uphoff, I., R. Lagerquist, K. Hillburn, Y. Lee, K. Haynes, J. Stock, C. Kumler, and J. Q. Stewart, 2021: CIRA guide to custom loss functions for neural networks in environmental sciences – Version 1. *arXiv preprint arXiv:2106.09757*.

Eusbi, R., G. A. Vecchi, C.-Y. Lai, and M. Tong, 2024: Realistic tropical cyclone wind and pressure fields can be reconstructed from sparse data using deep learning. *Nature Communications Earth and Environment*, **5**, 8, doi: 10.1038/s43247-023-01144-2.

Finocchio, P. M., S. J. Majumdar, D. S. Nolan, and M. Iskandarani, 2016: Idealized tropical cyclone responses to the height and depth of environmental vertical wind shear. *Monthly Weather Review*, **144**, 2155–2175, doi: 10.1175/MWR-D-15-0320.1.

Finocchio, P. M., and R. Rios-Berrios, 2021: The intensity- and size-dependent response of tropical cyclones to increasing vertical wind shear. *Journal of the Atmospheric Sciences*, **78**, 3673–3690, doi: 10.1175/JAS-D-21-0126.1.

Fischer, M. S., P. D. Reasor, R. F. Rogers, and J. F. Gamache, 2022: An analysis of tropical cyclone vortex and convective characteristics in relation to storm intensity using a novel airborne doppler radar database. *Monthly Weather Review*, **150**, 2255–2278, doi: 10.1175/MWR-D-21-0223.1.

Fischer, M. S., R. F. Rogers, P. D. Reasor, and J. P. Dunion, 2024: An observational analysis of the relationship between tropical cyclone vortex tilt, precipitation structure, and intensity change. *Monthly Weather Review*, **152**, 203–225, doi: 10.1175/MWR-D-23-0089.1.

Fitzpatrick, P. J., 1995: Understanding and forecasting tropical cyclone intensity change. Ph.D. thesis, Colorado State University.

Foerster, A. M., and M. M. Bell, 2017: Thermodynamic retrieval in rapidly rotating vortices from multiple-Doppler radar data. *Jounral of Atmospheric and Oceanic Technology*, **34 (11)**, 2353–2374, doi: 10.1175/JTECH-D-17-0073.1.

Frank, W. M., and E. A. Ritchie, 2001: Effects of vertical wind shear on the intensity and structure of numerically simulated hurricanes. *Monthly Weather Review*, **129**, 2249–2269, doi: 10.1175/1520-0493(2001)129<2249:EOVWSO>2.0.CO;2.

Franklin, J. L., M. L. Black, and K. Valde, 2003: Gps dropwindsonde wind profiles in hurricanes and their operational implications. *Weather and Forecasting*, **18 (1)**, 32–44, doi: 10.1175/1520-0434(2003)018<0032:GDWPIH>2.0.CO;2.

Fu, H., M. Riemer, and Q. Li, 2019: Effect of unidirectional vertical wind shear on tropical cyclone intensity change—lower-layer shear versus upper-layer shear. *Jounral of Geophysical Research: Atmospheres*, **124**, 6265–6282, doi: 10.1029/2019JD030586.

Gamache, J. F., P. Dodge, and N. Griffin, 2008: Automatic quality control and analysis of airborne Doppler data: Realtime applications, and automatically post-processed analyses for research. *Preprints, 28th Conf. on Hurricanes and Tropical Meteorology, Orlando, FL, Amer. Meteor. Soc., P2B*, Vol. 12.

Haurwitz, B., 1935: The height of tropical cyclones and the "eye" of the storm. *Monthly Weather Review*, **63**, 45–49.

Hazelton, A. T., L. Harris, and S.-J. Lin, 2018: Evaluation of tropical cyclone structure forecasts in a high-resolution version of the Multiscale GFDL fvGFS Model. *Weather and Forecasting*, **33**, 419–442, doi: 10.1175/WAF-D-17-0140.1.

Hazelton, A. T., and R. E. Hart, 2013: Hurricane eyewall slope as determined from airborne radar reflectivity data: Composites and case studies. *Weather and Forecasting*, **28**, 368–386, doi: 10.1175/WAF-D-12-00037.1.

Hendricks, E. A., M. S. Peng, B. Fu, and T. Li, 2010: Quantifying environmental control on tropical cyclone intensity change. *Monthly Weather Review*, **138**, 3243–3271, doi: 10.1175/2010MWR3185.1.

Hirschberg, P. A., and J. M. Fritsch, 1993: On understanding height tendency. *Monthly Weather Review*, **121**, 2646–2661, doi: 10.1175/1520-0493(1993)121<2646:OUHT>2.0.CO;2.

Holbach, H. M., 2022: SFMR retrieval algorithm update, URL https://www.weather.gov/media/nws/IHC2022/SFMR_Updates_IHC.pdf, tropical Cyclone Operations and Research Forum (TCORF), 9 March 2022, Lakeland, FL.

Holbach, H. M., and Coauthors, 2023: Recent advancements in aircraft and in situ observations of tropical cyclones. *Tropical Cyclone Research and Review*, **12 (2)**, 81–99, doi: 10.1016/j.tcrr.2023.06.001.

Holthuijsen, L. H., M. D. Powell, and J. D. Pietrzak, 2012: Wind and waves in extreme hurricanes. *Journal of Geophysical Research: Oceans*, **117 (C9)**, doi: 10.1029/2012JC007983.

Hong, S.-Y., J. Dudhia, and S.-H. Chen, 2004: A revised approach to ice microphysical processes for the bulk parameterization of clouds and precipitation. *Monthly Weather Review*, **132**, 103–120, doi: 10.1175/1520-0493(2004)132<0103:ARATIM>2.0.CO;2.

Hong, S.-Y., Y. Noh, and J. Dudhia, 2006: A new vertical diffusion package with an explicit treatment of entrainment processes. *Monthly Weather Review*, **134**, 2318–2341, doi: 10.1175/MWR3199.1.

Jones, S. C., 1995: The evolution of vortices in vertical shear. I: Initially barotropic vortices. *Quarterly Journal of the Royal Meteorological Society*, **121**, 821–851, doi: 10.1002/qj.49712152406.

Kaplan, J., and M. DeMaria, 2003: Large-scale characteristics of rapidly intensifying tropical cyclones in the North Atlantic basin. *Weather and Forecasting*, **18**, 1093–1108, doi: 10.1175/1520-0434(2003)018<1093:LCORIT>2.0.CO;2.

Kaplan, J., M. DeMaria, and J. A. Knaff, 2010: A revised tropical cyclone rapid intensification index for the Atlantic and Eastern North Pacific basins. *Weather and Forecasting*, **25**, 220–241, doi: 10.1175/2009WAF2222280.1.

Kepert, J., 2001: The dynamics of boundary layer jets within the tropical cyclone core. Part I: Linear theory. *Journal of the Atmospheric Sciences*, **58 (17)**, 2469—-2484, doi: 10.1175/1520-0469(2001)058<2469:TDOBLJ>2.0.CO;2.

Kepert, J., 2023: A parametric model of tropical cyclone surface winds for sea and land. *Weather and Forecasting*, **38 (9)**, 1739–1757, doi: 10.1175/WAF-D-23-0028.1.

Kepert, J., and Y. Wang, 2001: The dynamics of boundary layer jets within the tropical cyclone core. Part II: Nonlinear enhancement. *Journal of the Atmospheric Sciences*, **58 (17)**, 2485—-2501, doi: 10.1175/1520-0469(2001)058<2485:TDOBLJ>2.0.CO;2.

Klotz, B. W., and D. S. Nolan, 2019: SFMR surface wind undersampling over the tropical cyclone life cycle. *Monthly Weather Review*, **147**, 247–268, doi: 10.1175/MWR-D-18-0296.1.

Klotz, B. W., and E. W. Uhlhorn, 2014: Improved stepped frequency microwave radiometer tropical cyclone surface winds in heavy precipitation. *Journal of Atmospheric and Oceanic Technology*, **31 (11)**, 2392–2408, doi: 10.1175/JTECH-D-14-00028.1.

Klotzbach, P. J., M. M. Bell, S. G. Bowen, E. J. Gibney, K. R. Knapp, and C. J. Schreck III, 2020: Surface pressure a more skillful predictor of normalized hurricane damage than maximum sustained wind. *Bulletin of the American Meteorological Society*, **101 (6)**, E830–E846, doi: 10.1175/BAMS-D-19-0062.1.

Klotzbach, P. J., D. R. Chavas, M. M. Bell, S. G. Bowen, E. J. Gibney, and C. J. Schreck III, 2022a: Characterizing continental us hurricane risk: Which intensity metric is best? *Journal of Geophysical Research: Atmospheres*, **127 (18)**, e2022JD037 030, doi: 10.1029/2022JD037030.

Klotzbach, P. J., K. M. Wood, C. J. Schreck III, S. G. Bowen, C. M. Patricola, and M. M. Bell, 2022b: Characterizing continental us hurricane risk: Which intensity metric is best? *Geophysical Research Letters*, **49 (6)**, e2021GL095 774, doi: 10.1029/2021GL095774.

Knaff, J. A., and C. J. Slocum, 2024: An automated method to analyze tropical cyclone surface winds from real-time aircraft reconnaissance observations. *Weather and Forecasting*, **39 (2)**, 339–349, doi: 10.1175/WAF-D-23-0077.1.

Knaff, J. A., and Coauthors, 2021: Estimating tropical cyclone surface winds: Current status, emerging technologies, historical evolution, and a look to the future. *Tropical Cyclone Research and Review*, **10 (3)**, 125–150, doi: 10.1016/j.tcrr.2021.09.002.

Landsea, C. W., and J. L. Franklin, 2013a: Atlantic hurricane database uncertainty and presentation of a new database format. *Monthly Weather Review*, **141**, 3576–3592, doi: 10.1175/MWR-D-12-00254.1.

Landsea, C. W., and J. L. Franklin, 2013b: Atlantic hurricane database uncertainty and presentation of a new database format. *Monthly Weather Review*, **141 (10)**, 3576–3592, doi: 10.1175/MWR-D-12-00254.1.

LeCun, Y., Y. Bengio, and G. Hinton, 2015: Deep learning. *Nature*, **521**, 436–444.

Lorsolo, S., and A. Aksoy, 2012: Wavenumber analysis of azimuthally distributed data: Assessing maximum allowable gap size. *Monthly Weather Review*, **140**, 1945–1956, doi: 10.1175/MWR-D-11-00219.1.

Lorsolo, S., J. Gamache, and A. Aksoy, 2013: Evaluation of the hurricane research division doppler radar analysis software using synthetic data. *Journal of Atmospheric and Oceanic Technology*, **30 (6)**, 1055–1071, doi: 10.1175/JTECH-D-12-00161.1.

Lorsolo, S., J. A. Zhang, F. Marks Jr., and J. Gamache, 2010: Estimation and mapping of hurricane turbulent energy using airborne doppler measurements. *Monthly Weather Review*, **138 (9)**, 3656–3670, doi: 10.1175/2010MWR3183.1.

Martinez, J., M. M. Bell, R. Rogers, and J. D. Doyle, 2019: Axisymmetric potential vorticity evolution of Hurricane Patricia (2015). *Journal of Atmospheric Science*, **76**, 2043–2063, doi: 10.1175/JAS-D-18-0373.1.

Martinez, J., M. M. Bell, J. L. Vigh, and R. F. Rogers, 2017: Examining tropical cyclone structure and intensification with the flight+ dataset from 1999 to 2012. *Monthly Weather Review*, **145 (11)**, 4401–4421, doi: 10.1175/MWR-D-17-0011.1.

Martinez, J., C. A. Davis, and M. M. Bell, 2022: Eyewall asymmetries and their contributions to the intensification of an idealized tropical cyclone translating in uniform flow. *Journal of the Atmospheric Sciences*, **79**, 2471–2491, doi: 10.1175/JAS-D-21-0302.1.

Mouche, A. A., B. Chapron, B. Zhang, and R. Husson, 2017: Combined co- and cross-polarized sar measurements under extreme wind conditions. *IEEE Transactions on Geoscience and Remote Sensing*, **55 (12)**, 6746–6755, doi: 10.1109/TGRS.2017.2732508.

Nachar, N., 2008: The mann-whitney u: A test for assessing whether two independent samples come from the same distribution. *Tutorials in quantitative Methods for Psychology*, **4**, 13–20, doi: 10.20982/tqmp.04.1.p013.

Nam, C. C., M. M. Bell, and D. Tao, 2023: Bifurcation points for tropical cyclone genesis and intensification in sheared and dry environments. *Journal of the Atmospheric Sciences*, **80**, 2239–2259, doi: 10.1175/JAS-D-22-0100.1.

Nguyen, L. T., J. Molinari, and D. Thomas, 2014: Evaluation of tropical cyclone center identification methods in numerical models. *Monthly Weather Review*, **142**, 4326–4339, doi: 0.1175/MWR-D-14-00044.1.

Nolan, D. S., 2011: Evaluating environmental favorableness for tropical cyclone development with the method of point-downscaling. *Journal of Advances in Modeling Earth Systems*, **3**, M08 001, doi: 10.1029/2011MS000063.

Nolan, D. S., Y. Moon, and D. P. Stern, 2007: Tropical cyclone intensification from asymmetric convection: Energetics and efficiency. *Journal of Atmospheric Science*, **64**, 3377–3405, doi: 10.1175/JAS3988.1.

Ohno, M., Tomoki andSatoh, 2015: On the warm core of a tropical cyclone formed near the tropopause. *Journal of the Atmospheric Sciences*, **72 (2)**, 551–571, doi: 10.1175/JAS-D-14-0078.1.

O'Malley, T., E. Bursztein, J. Long, F. Chollet, H. Jin, and L. Invernizzi, 2019: Kerastuner. GitHub, URL https://github.com/keras-team/keras-tuner.

Onderlinde, M. J., and D. S. Nolan, 2017: The tropical cyclone response to changing wind shear using the method of time-varying point-downscaling. *Journal of Advances in Modeling Earth Systems*, **9**, 908–931, doi: 10.1002/2016MS000796.

Ooyama, K. V., 1969: Numerical simulation of the life cycle of tropical cyclones. *Journal of the Atmospheric Sciences*, **26**, 3–40, doi: 10.1175/1520-0469(1969)026<0003:NSOTLC>2.0.CO;2.

Pasch, R. J., B. J. Reinhart, and R. Berg, 2021: National Hurricane Center tropical cyclone report: Hurricane Eta (AL292020). NHC Tech. Rep.

Peng, K., and J. Fang, 2021: Effect of the initial vortex vertical structure on early development of an axisymmetric tropical cyclone. *Journal of Geophysical Research*, **126 (4)**, doi: 10.1029/2020JD033697.

Powell, M. D., E. W. Uhlhorn, and J. D. Kepert, 2009: Estimating maximum surface winds from hurricane reconnaissance measurements. *Weather and Forecasting*, **24 (3)**, 868–883, doi: 10.1175/2008WAF2007087.1.

Powell, M. D., and Coauthors, 2010: Reconstruction of hurricane katrina's wind fields for storm surge and wave hindcasting. *Ocean Engineering*, **37 (1)**, 26–36, doi: 10.1016/oceaneng.2009.08.14.

Rios-Berrios, R., C. A. Davis, and R. D. Torn, 2018: A hypothesis for the intensification of tropical cyclones under moderate vertical wind shear. *Journal of the Atmospheric Sciences*, **75**, 4149–4173, doi: 10.1175/JAS-D-18-0070.1.

Rios-Berrios, R., and R. D. Torn, 2017: Climatological analysis of tropical cyclone intensity changes under moderate vertical wind shear. *Monthly Weather Review*, **145 (5)**, 1717–1738, doi: 10.1175/MWR-D-16-0350.1.

Rogers, R. F., P. Reasor, and S. Lorsolo, 2013: Airborne Doppler observations of the inner-core structural differences between intensifying and steady-state tropical cyclones. *Monthly Weather Review*, **141**, 2970–2991, doi: 10.1175/MWR-D-12-00357.1.

Rogers, R. F., and Coauthors, 2017: Rewriting the tropical record books: The extraordinary intensification of Hurricane Patricia (2015). *Bulletin of the American Meteorological Society*, **98**, 2091–2112, doi: 10.1175/BAMS-D-16-0039.1.

Rousseau-Rizzi, R., and K. Emanuel, 2019: An evaluation of hurricane superintensity in axisymmetric numerical models. *Journal of the Atmospheric Sciences*, **76**, 1697–1708, doi: 10.1175/JAS-D-18-0238.1.

Ruppert Jr, J. H., A. A. Wing, X. Tang, and E. L. Duran, 2020: The critical role of cloud–infrared radiation feedback in tropical cyclone development. *Proceedings of the National Academy of Sciences*, **117**, 27 884–27 892, doi: 10.1073/pnas.2013584117.

Sampson, C. R., and J. A. Knaff, 2015: A consensus forecast for tropical cyclone gale wind radii. *Weather and Forecasting*, **30 (5)**, 1397–1403, doi: 10.1175/WAF-D-15-0009.1.

Sapp, J. W., S. O. Alsweiss, Z. Jelenak, P. S. Chang, and J. Carswell, 2019: Stepped frequency microwave radiometer wind-speed retrieval improvements. *Remote Sensing*, **11 (3)**, 214, doi: 10.3390/rs11030214.

Schubert, W. H., and J. J. Hack, 1982: Inertial stability and tropical cyclone development. *Journal of Atmospheric Science*, **39 (8)**, 1687–1697, doi: 10.1175/1520-0469(1982)039<1687:ISATCD>2.0.CO;2.

Shapiro, L. J., 1983: The asymmetric boundary layer flow under a translating hurricane. *Journal of the Atmospheric Sciences*, **40 (8)**, 1984—-1998, doi: 10.1175/1520-0469(1983)040<1984:TABLFU>2.0.CO;2.

Skamarock, W. C., and Coauthors, 2008: A description of the advanced research wrf version 3. *NCAR technical note*, **475**, 113.

Smith, R. K., and M. T. Montgomery, 2016: Understanding hurricanes. *Weather*, **71 (9)**, 219–223, doi: 10.1002/wea.2776.

Srivastava, N., G. Hinton, A. Krizhevsky, I. Sutskever, and R. Salakhutdinov, 2014: Dropout: A simple way to prevent neural networks from overfitting. *The Journal of Machine Learning Research*, **15**, 1929–1958.

Stern, D. P., J. R. Brisbois, and D. S. Nolan, 2014: An expanded dataset of hurricane eyewall sizes and slopes. *Journal of Atmospheric Science*, **71**, 2747–2762, doi: 10.1175/JAS-D-13-0302.1.

Stern, D. P., and D. S. Nolan, 2009: Reexamining the vertical structure of tangential winds in tropical cyclones: Observations and theory. *Journal of Atmospheric Science*, **66**, 3579–3600, doi: 10.1175/2009JAS2916.1.

Stern, D. P., and D. S. Nolan, 2011: On the vertical decay rate of the maximum tangential winds in tropical cyclones. *Journal of Atmospheric Science*, **68**, 2073–2094, doi: 10.1175/2011JAS3682.1.

Stern, D. P., J. L. Vigh, D. S. Nolan, and F. Zhang, 2015: Revisiting the relationship between eyewall contraction and intensification. *Jounral of the Atmospheric Sciences*, **72**, 1283–1306, doi: 10.1175/JAS-D-14-0261.1.

Stewart, S. R., 2017: National Hurricane Center tropical cyclone report: Hurricane Matthew (AL142016). NHC Tech. Rep.

Tao, D., and F. Zhang, 2014: Effect of environmental shear, sea-surface temperature, and ambient moisture on the formation and predictability of tropical cyclones: An ensemble-mean perspective. *Journal of Advances in Modeling Earth Systems*, **6**, 384–404, doi: 10.1002/2014MS000314.

Thompson, G., R. M. Rasmussen, and K. Manning, 2004: Explicit forecasts of winter precipitation using an improved bulk microphysics scheme. Part i: Description and sensitivity

analysis. *Monthly Weather Review*, **132**, 519–542, doi: 10.1175/1520-0493(2004)132<0519:EFOWPU>2.0.CO;2.

Trabing, B. C., and M. M. Bell, 2020: Understanding error distributions of hurricane intensity forecasts during rapid intensity changes. *Weather and Forecasting*, **35 (6)**, 2219–2234, doi: 10.1175/WAF-D-19-0253.1.

Trabing, B. C., and M. M. Bell, 2021: The sensitivity of eyewall replacement cycles to shortwave radiation. *Journal of Geophysical Research: Atmospheres*, **126**, e2020JD034 016, doi: 10.1029/2020JD034016.

Trabing, B. C., M. M. Bell, and B. R. Brown, 2019: Impacts of radiation and upper-tropospheric temperatures on tropical cyclone structure and intensity. *Journal of the Atmospheric Sciences*, **76**, 135–153, doi: 10.1175/JAS-D-18-0165.1.

Uhlhorn, E. W., P. G. Black, J. L. Franklin, M. Goodberlet, J. Carswell, and A. S. Goldstein, 2007: Hurricane surface wind measurements from an operational stepped frequency microwave radiometer. *Monthly Weather Review*, **135 (9)**, 3070–3085, doi: 10.1175/MWR3454.1.

Uhlhorn, E. W., B. W. Klotz, T. Vukicevic, P. D. Reasor, and R. F. Rogers, 2014: Observed hurricane wind speed asymmetries and relationships to motion and environmental shear. *Monthly Weather Review*, **142 (3)**, 1290–1311, doi: 10.1175/MWR-D-13-00249.1.

Vigh, J. L., and Coauthors, 2020: Flight+: The extended flight level dataset for tropical cyclones. Tropical Cyclone Data Project, National Center for Atmospheric Research, Research Applications Laboratory, Boulder, Colorado, URL https://verif.rap.ucar.edu/tcdata/flight/, doi: 10.5065/D6WS8R93.

Wang, Z., M. T. Montgomery, and C. Fritz, 2012: A first look at the structure of the wave pouch during the 2009 PREDICT-GRIP dry runs over the Atlantic. *Monthly Weather Review*, **140 (4)**, 1144–1163, doi: 10.1175/MWR-D-10-05063.1.

Williams Jr., G. J., 2015: The effects of vortex structure and vortex translation on the tropical cyclone boundary layer wind field. *Journal of Advances in Modeling Earth Systems*, **7**, 188–214, doi: 10.1002/2013MS000299.

Zawislak, J., L. Nguyuen, E. Paltz, K. Young, H. Voemel, and T. Hock, 2018: Development and applications of a long-term, global tropical cyclone dropsonde dataset., 33rd Conference on Hurricanes and Tropical Metorology, Ponte Vedra, FL, Amer. Meter. Soc.